High-Performance Organic Light Emitting Diodes

by

Kody George Klimes

A Dissertation Presented in Partial Fulfillment
of the Requirements for the Degree
Doctor of Philosophy

Approved April 2019 by the
Graduate Supervisory Committee:

Jian Li, Chair
James Adams
Liping Wang

ARIZONA STATE UNIVERSITY

May 2019

ABSTRACT

Organic electronics have remained a research topic of great interest over the past few decades, with organic light emitting diodes (OLEDs) emerging as a disruptive technology for lighting and display applications. While OLED performance has improved significantly over the past decade, key issues remain unsolved such as the development of stable and efficient blue devices. In order to further the development of OLEDs and increase their commercial potential, innovative device architectures, novel emissive materials and high-energy hosts are designed and reported.

OLEDs employing step-wide graded-doped emissive layers were designed to improve charge balance and center the exciton formation zone leading to improved device performance. A red OLED with a peak efficiency of 16.9% and an estimated LT_{97} over 2,000 hours at 1,000 cd/m^2 was achieved. Employing a similar structure, a sky-blue OLED was demonstrated with a peak efficiency of 17.4% and estimated LT_{70} over 1,300 hours at 1,000 cd/m^2. Furthermore, the sky-blue OLEDs color was improved to CIE coordinates of (0.15, 0.25) while maintaining an efficiency of 16.9% and estimated LT_{70} over 600 hours by incorporating a fluorescent sensitizer. These devices represent literature records at the time of publication for efficient and stable platinum phosphorescent OLEDs.

A newly developed class of emitters, metal-assisted delayed-fluorescence (MADF), are demonstrated to achieve higher-energy emission from a relatively low triplet energy. A green MADF device reaches a peak efficiency of 22% with an estimated LT_{95} over 350 hours at 1,000 cd/m^2. Additionally, a blue charge confined OLED of PtON1a-tBu demonstrated a peak efficiency above 20%, CIE coordinated of (0.16, 0.27), and emission onset at 425 nm.

High triplet energy hosts are required for the realization of stable and efficient deep blue emission. A rigid "M"-type carbazole/fluorene hybrid called mDCzPF and a carbazole/9-silafluorene hybrid called mDCzPSiF are demonstrated to have high triplet energies E_T=2.88 eV and 3.03 eV respectively. Both hosts are demonstrated to have reasonable stability and can serve as a template for future material design. The techniques presented here demonstrate alternative approaches for improving the performance of OLED devices and help to bring this technology closer to widespread commercialization.

ACKNOWLEDGMENTS

My thanks are due firstly to my advisor, mentor and friend, Dr. Jian Li. Without him, none of this work would have been possible. He graciously welcomed me into his group as an undergraduate researcher and has shown me his unwavering support for my work ever since. He has guided my professional development, imparted his expertise in the OLED field and aided in my transition to industry. I cannot thank him enough for giving me the opportunity to be a part of his research team. Additional thanks are owed to Tyler Fleetham for being a role model to me as a young student and teaching me the fundamentals of research, Guijie Li for guiding the chemical synthesis team during my early years in the group, Zhi-Qiang Zhu for guiding the chemical synthesis team during my later years in the group and being a friend/teacher to me in the field of organic chemistry, Linyu Cao for her aid in synthesis and photophysical measurements and Barry O'Brien for improving my interpersonal communication skills and for providing access to measurement equipment. Thanks are also given to all collaborating researchers who are not individually named here.

Most of all, I would like to thank my family. It is often said that 'nothing is achieved alone' and that bears repeating. I would not be where I am today without the love and support of my parents, brothers and extended family. I dedicate this work to them.

TABLE OF CONTENTS

Page

LIST OF TABLES vi

LIST OF FIGURES vii

LIST OF EQUATIONS xvi

CHAPTER

1: INTRODUCTION 1

1.1: Organic Electronics 1

1.2: OLED Operating Principals 4

1.3: Evolution of the OLED 16

1.4: Performance and Characterization of OLEDs: 22

1.5: Overview of Mechanisms that Impact OLED Lifetime and Efficiency 32

1.6: Research Drive: 36

2: IMPROVING OLED PERFORMANCE THROUGH EMISSIVE LAYER DESIGN 40

2.1: Improvements in the Stability and Efficiency of OLEDs Through Adept Emissive Layer Design 42

2.2: Improving the Emission Color Quality Using Florescent Blue Emitters 49

2.3: PtN3N Layered Structure 57

2.4: Conclusion 67

3: METAL-ASSISTED DELAYED FLUORESCENCE 68

CHAPTER Page

3.1: PdN3N: Green MADF 71

3.2: PdN1N-dm: Blue MADF 79

3.3: PdON1a: Blue MADF with Improved Fluorescent Component 87

3.4: Conclusion 98

4: DEVELOPMENT OF NEW HOST MATERIALS 99

4.1: "M"-Type Hosts 101

4.2: Conclusion 110

5: OPTICAL EXTRACTION 111

5.1: Setfos Simulations 116

5.2: PtN8PPy Device Study 123

5.3: Pd3O3 Device Study 126

5.4: Conclusion 130

6: CONCLUSIONS 131

6.1: Blue OLEDs 131

6.2: High Energy Host Materials 132

6.3: Enhanced Low-Cost Optical Extraction 133

6.4: Commercial Impacts of Research 133

REFERENCES 136

APPENDIX 149

A CUSTOM BUILT OLED EQUIPMENT FOR AAML LAB 149

LIST OF TABLES

Table Page

1. Summary of PtNON and PtNON with TBPe Devices, EQE, Brightness, Lifetime, and CIE Coordinates are Shown. 56
2. Summary of PtN3N Device Performance Metrics. 63
3. Photophysical and Electrochemical Properties of the Platinum(II) Complexes (a) Measured in a CH_2Cl_2 Solution at Room Temperature. (b) Measured in a 2-Me-THF Solution at 77K. (c) Measured in a PMMA Film at Room Temperature. (d) $k_r = \Phi/\tau$. (e) $k_{nr} = (1-\Phi)/\tau$. Where the k_r and k_{nr} are the Radiative and Non-Radiative Rate Constants, Respectively. (f) The HOMO and LUMO Levels Were Calculated by Using $Cp_2Fe^{0/+}$ Values of 4.8 eV Below the Vacuum Level. (g)Calculated from the λ_{max} of the 77K Emission Spectra Measured in 2-Me-THF Solution. 89
4. Photophysical and Electrochemical Properties of Host Materials. 104
5. Summary of PtN3N-ptb Device Performance. 107
6. Summary of Device Performance of Ptn8ppy EQE with Various Theoretical Extractor Efficiency. 126

LIST OF FIGURES

Figure Page

1. Schematic of Opv, Showing Key Active Layers, Light Absorption, Charge Separation and Charge Collection....2
2. Standard Otft Schematic Showing the Source, Drain, and Gate That Are Required in All Transistor Devices. 3
3. Step by Step Process Demonstrating How Dna Can Be Utilized for Mass Storage. ...3
4. A) Standard Diode P-n Junction in Line with a Circuit B) Circuit Schematic Representation of Diode Denoting Current Flow Direction and Current Stopping Direction C) Current-voltage Curve Showing Diodes Ability to Inhibit Current Flow When under Reverse Bias and Allow Current Flow under Forward Bias. 5
5. N-doped and P Doped Inorganic Semiconductors Showing Their Conduction and Valence Bands with Free Charge Carriers. 6
6. Diagram Showing an Example of Electrons Hopping in the Lumo and Stopping on the Discrete Isolated States Denoted by (B). 7
7. A Depiction of Homo and Lumo Level Occupation in the 4 Different States That a Molecule Can Be in a) Ground State B) Hole Polaron (Referred to as a Hole) C) Electron Polaron (Electron) and D) Exciton.....8
8. Illustration of Exciton Types Showing Spin Direction and Phase. A) Singlet Exciton with Opposite Spin B) Triplet Excitons with Three Possible Spin Conditions.....9
9. Diagram Showing Fret and Dexter Energy Transfer from One Molecule to Another. 10

Figure Page

10. Energy Band Diagram Showing Singlet and Triplet Decay Paths That Lead to Fluorescence and Phosphorescence and Intersystem Crossing (ISC). 12
11. Schematic Showing Emission Pathways of Thermal Assisted Delayed Fluorescence (Left) and Metal-Assisted Delayed Fluorescence (Right). 13
12. Jablonski Diagram Showing Singlet and Triplet Excited States with Their Vibronic Bands, Average Transition Timescales, and the Ground State. 14
13. The Visible Electromagnetic Spectrum in Terms of Wavelength and Energy. 16
14. Kodak First OLED by Tang and Vanslyke, a Two-Layer Device Using a Diamine for Hole Transport and Alq_3 for Emission. 17
15. HOMO-LUMO Diagram of All 9 Layers of an OLED Device Showing Charge Injection, Transport, and Recombination. 18
16. HOMO LUMO Diagram of OLED Transport, Blocking and Emissive Layers Showing Electrons and Holes Moving in the Layers. 19
17. Thermal Vapor Deposition Showing the Key Components. 20
18. Schematic Showing Spin Coating Steps 1) Coat 2) Spin (Low Speed) 3) Spin (High Speed) 4) Dry. 22
19. A) Diagram of OLED IVL Testing B) Schematic of Spectrometer Operation. 23
20. Schematic Cross-Section of an Integrating Sphere Showing Entrance Port and Detector Port. 25
21. Cross-Section View of an OLED Showing the Major Optical Loss Mechanisms 26
22. Weighting vs Wavelength of the CIE Imaginary Primary Colors $X(\lambda), Y(\lambda)$ and $Z(\lambda)$. 30
23. Commission Internationale De l'Eclairange 1931 X-Y Chromaticity Plot. 31

Figure Page

24. Diagram of Electron Buildup in the OLED Emissive Layer, Caused by Unbalanced Charge Injection and Strong Electron Blockers. 41

25. Absorption and Emission Spectra of PtNON in 2-Methyl Tetrahydrofuran at 77 K, in a Solution of Dichloromethane at Room Temperature and in a Doped PMMA Thin Film at Room Temperature. 42

26. Schematic Showing the Stable OLED Structure Used For Devices 1-6 and 11-14. Layer Thickness is as Follows, ITO (40nm), Hat-CN (10nm), NPD (40nm), Tris-PCZ (10nm Or 0nm In Device 5 And 6), Mcbt (8nm), Bpytp (40nm), Lif (1nm), Aluminum (100nm). B) Schematic to Visualize the Varying Doping Structure used for Device 1-6, Device 1,5 (25nm), Device 2, 3, 4 and 6 (30nm). 44

27. A) EL Intensity vs Wavelength with Inset Graph Showing an Enhanced View of the Blue Region Below 450nm B) Normalized Intensity vs Time with Figure Inset Showing EQE vs Luminescence Curve. 45

28. Stable OLED Structure Showing HOMO and LUMO Levels. 46

29. A) EQE vs Luminance Plot of Devices 1-4, B) EL Spectra with Subplot Showing Emission in the 380- 480nm Wavelength Range, C) Normalized Relative Intensity vs Operational Lifetime at Constant Current of 20mA/cm^2, D) EL Spectra With Subplot Showing Emission Range Between 380-480nm Comparing Key Devices With and Without an Electron Blocking Layer. 47

Figure Page

30. Energy Level Diagram Interpretation of Tbpe and Ptnon Interaction. PtNON is a Phosphorescent Emitter with a High Triplet Energy Above Tbpe's Singlet Energy. FRET Can Allow Triplets Harvested on Ptnon to be Transferred to Tbpe and Emit From the Singlet State. PtNON's High IQE, this Process Can Result in Fluorescent Emitters Emitting with an IQE Above the Theoretical Limit of 25%. 50

31. A) Schematic Showing Charged Confined OLED Structure Used in Device 7-10, Layer Thickness are ITO (40nm), Hat-CN (10nm), NPD (40nm), TAPC (10nm) DPPS (10nm), Bmpypb (40nm), Lif (1nm), Aluminum (100nm). B) EML Structure of Device 7-10, 7: 10% Ptnon in Mcpy26 (25nm), 8: 10%Ptnon:1%Tbpe:in Mcpy26 (25nm), 9: 10% Ptnon:2% Tbpe: in Mcpy26 (25nm), 10: 10%Ptnon: in Mcpy26 (4nm), 2% Tbpe: in Mcpy26 (2nm), 10%Ptnon: in Mcpy26 (4nm), 2% Tbpe: in Mcpy26 (2nm), 10%Ptnon: in Mcpy26 (4nm). 51

32. A) EQE vs Luminance, B) EL Spectra Measured at 1mA/cm^2 of Devices in Charge Confined Structure. 52

33. A) Schematic Showing the Doping Scheme for Devices 11-14, B) EQE Vs Luminance for Devices 11-14, C) EL Spectra of Devices 11-14 With Respective CIE Coordinates, D) Normalized Relative Intensity vs Operational Lifetime at a Constant Driving Current of 20 mA/cm^2. 53

34. Absorption and Emission Spectra of Ptn3n and its Analog Ptn3n-Ptb.....59

35. PL Spectra At 77K in a Solution of 2me-THF. 60

36. A) EL Spectra with the Inset Showing Nonexclusive Emission from 400-450nm, B) EQE vs Luminance, C) Device Operational Time at 20mA/cm^2 D) Schematic of Single and Split EML Used in Device 2 and 4. 61

Figure Page

37. Variable Current Density Lifetime A) Device 2 Employing a Single EML, B) Device 4 Employing a Split EML....64
38. Escalation Factor of Single and Split EML. 66
39. Summary of Singlet and Triplet Transitions Associated With A) Fluorescence, B) Phosphorescence, C) Thermal Activated Delayed Fluorescence And D) Metal Assisted Delayed Fluorescence. 69
40. Absorption of Pdn3n and N3N Ligand with Enhanced MLCT Absorption Peak, PL of Pdn3n at 300K and 77K.....72
41. A) Excitation Spectra Measured at 485nm and 530nm Corresponding to the Thermally Activated Peak and the Primary Phosphorescent Peak, B) Transient Lifetime of Pdn3n Measured at 485nm and 530nm.....73
42. Variable Temperature PL Measurements Offset in the Y Direction for Clarity. 74
43. A) Cyclic Voltammetry of Pdn3n Vs Fc/Fc^+ B) Transient Lifetime Vs Temperature of Pdn3n. 75
44. EQE Versus Luminance with The Corresponding EL Spectra at 1 mA/cm2 Inset for Devices of Pdn3n in the Structure: ITO/ HATCN/ NPD/ TAPC/ 6% Pdn3n:26mcpy/ DPPS/ Bmpypb/ Lif/ Al.....76
45. A) Current Density vs Voltage, B) EL Spectra, C) EQE vs Luminance and D) Device Operational Lifetime. 78
46. Illustrates the Design of Blue Shifted MADF Emitter by Replacing the Pyridine with a Pyrazolyl to Raze the LUMO. 79
47. Room Temperature Absorption Spectra of Pdn1n, Pdn1n-Dm, and Pdn6n in Dichloromethane.....80

Figure Page

48. Photoluminescence Spectra of Ptn1n, Pdn1n, Pdn1n-Dm, and Pdn6n at Room Temperature in Dichloromethane (Solid Lines) and at 77 K in 2-Methyltetrahydrofuran (Dash-Dotted Lines). the Redox Potentials for Each Complex Were Also Given. 81

49. Cyclic Voltammograms For Pdn1n, Pdn1n-Dm, And Pdn6n....83

50. A) EL Spectra Collected at 1 mA/cm2, B) EQE vs. Luminance for Device 1-2 with Structure: ITO/HATCN/NPD/TAPC/10% Pdn1n-Dm: X % Ptn3n-Ptb: 26mcpy/DPPS/Bmpypb/Lif/Al, Wherein X is 0% for Device 1 and 1% For Device 2....84

51. A) EL Spectra, (B) Current Density vs Voltage, (C) EQE vs Luminance, and (D) Plots of Relative Luminance Vs. Operation Time for Device 3-6....86

52. (A) UV-Vis Absorption Spectra of Pton1a-Tbu, Pton1a-DM-Tbu and Pton1-Tbu in CH2Cl2 Solution at Room Temperature. The Chemical Structures (Inset) and Emission Spectra of Pton1a-Tbu (B), Pton1a-DM-Tbu (C) and Pton1-Tbu (D) in Degassed CH2Cl2 (Solid Lines). 90

53. Emission Spectra of Pton1a-Tbu in 2-Me-THF Solution at the Variable Temperatures Ranging From 77K To 298K....93

54. A) Energy Level Diagram of Materials Used in the Devices. B) Molecular Structures of the Materials Employed in the Devices. C) the Electroluminescent Spectra of Pton1a-Tbu and Pton1a-DM-Tbu at Room Temperature. D) the Plots of External Quantum Efficiency....95

Figure Page

55. The External Quantum Efficiency Versus Luminance for Devices in the Structure: ITO/HATCN/NPD/TAPC/10% Pton1a-Tbu:1% Tbpe:Mcpy/DPPS/Bmpypb/Lif/Al. The Emission Spectrum of the Device (Purple) is Shown in the Inset as Well as the Spectrum for the Pton1a-Tbu Reference Device (Blue). 97

56. Molecular Structures of the Newly Developed "M"-Type Host Materials and the Structure of "V"-Type Host. 102

57. (A) Optimized Structures, HOMO and LUMO Distributions of Pdczpf and Mdczpf Calculated by DFT (Titan/B3LYP/6–31G*). Hydrogen Atoms Were Omitted for Clarity. (B) the Fluorescent Spectra of Pdczpf, Mdczpf and Mdczpsif in CH2Cl2 Solution at Room Temperature. 103

58. (A) Energy Level Diagram and Chemical Structures of the Materials for the Ptn3n-Ptb-Doped Oleds (Devices 1-4) Using CBP, Pdczpf, Mdczpf or Mdczpsif as Hosts. (B) EL Spectra, (C) Current Density–Voltage (J–V) Characteristics, (D) External Quantum Efficiency (EQE) Versus Luminance Plots (E) Luminance Intensity-Time Curves of Devices 1-4. HIL, Hole Injection Layer; HTL, Hole Transporting Layer; EML, Emissive Layer; HBL, Hole Blocking Layer; ETL, Electron Transporting Layer. 106

Figure Page

59. (A) Energy Level Diagram and Chemical Structures of the Materials for the Ptnon-Doped Oleds (Devices 5, 6) Using 26mcpy Or **Mdczpf** as Hosts. (B) EL Spectra, (C) Current Density–Voltage (J–V) Characteristics, (D) Power Efficiency-Luminance (P–L) Characteristics, and (E) External Quantum Efficiency (EQE) Versus Luminance Plots of Devices 5 and 6. EBL, Electron/Exciton Blocking Layer. 109

60. Schematic Showing General Layer Structure and Emission Direction for A) Bottom Emitting OLED, B) Inverted Bottom Emitting OLED, C) Top Emitting OLED.112

61. Planer vs Corrugated Substrate Schematic. 113

62. Schematic of Microlense Array on Substrate. 114

63. Schematic Showing Isotropic vs Horizontal Dipole Orientation and its Impact on Emitted Light. 115

64. A1-A4 FDTD Simulation of Emission for 0 Pair, 1 Pair, 2 Pair and 3 Pair Respectively at Variable NPD Thickness. B1-B4 Setfos Simulation of Emission For 0 Pair, 1 Pair, 2 Pair and 3 Pair Respectively at Variable NPD Thickness. C1-C4 EQE vs NPD Thickness. 118

65. A) Schematic of the Standard Bottom Emitting OLED Structure that we Employed, B) Breakdown of Probabilities of Lighting in Each of the Different Modes in a OLED Structure as the ETL Changes in Thickness, (Red-Air Mode, Dark Blue-Substrate Mode, Yellow-Absorption Loss, Pink- Organic Waveguide Mode, Light Blue: Plasmon Quenching. 119

66. A) Loss Modes vs HTL Thickness, B) Loss Modes vs Transparent Anode Thickness. 120

Figure Page

67. Variable ITO and HTL Thickness A) Air Mode Extraction, B) Substrate Mode and C) Combined Air and Substrate Mode.....122

68. A) CIE Plot Showing the ECE Defined Red and Yellow (Amber) Regions, B) Narrow Band Emitter Electroluminescent Emission with Chemical Structure, and C) Schematic Showing How Air Mode and Substrate Mode are Measured. 124

69. A) EQE vs Luminance of Standard and Optimized OLED, Measuring Air Mode and Airmode + Substrate Mode, B) EL Spectra of Standard and Optimized Device. ...125

70. A) Schematic of Angular Dependent PL Spectroscopy Measurement, B) Experimental vs Simulated Intensity vs Detection Angle. 127

71. Setfos Simulation of Emitter Dipole Orientation and its Impact on Optical Extraction. 128

72. A) Pd3O3's Chemical Structure, B) EQE Vs Luminance, C) EL Emission Spectrum, and D) Device Operation Time at Variable Brightness.....129

LIST OF EQUATIONS

Equation Page

1 9

2 28

3 29

4 30

5 30

1: Introduction

1.1: Organic Electronics

Electronic properties in organic compounds have been of interest to researchers since the early 1900s.[1] In the past few decades, these organic electronics have seen a sharp rise in use across a variety of applications. The most common among these are organic photovoltaics (OPVs), organic thin film transistors (OTFTs), organic memory storage solutions and organic light emitting diodes (OLEDs).

Photovoltaic (PV) devices have been gaining widespread traction in markets across the world as their efficiency continues to rise and their cost becomes more competitive. Photovoltaic devices, colloquially called solar panels, absorb visible and infrared light and convert that light to a usable electric current. These have long been viewed as a viable source of renewable energy and are being widely implemented across the world.[2,3] For example, California has recently passed a new law that will require every new home built in 2020 or later to incorporate rooftop PV panels. Conventional PV devices are commonly made from inorganic semiconductors like silicon and therefore suffer from problems such as fragile panel components, heavy mounting hardware, and bulky design. Alternatively, organic photovoltaic (OPV) systems can be made thin, flexible and transparent. Figure 1 shows a typical cross-section of an OPV. Their thin profiles (.5mm or less) coupled with their use of

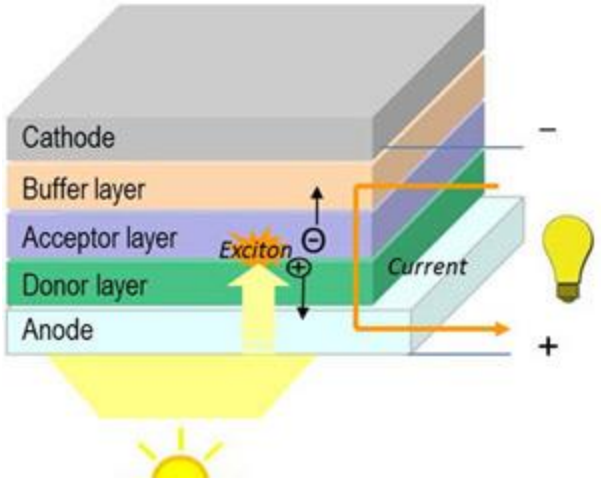

Figure 1: Schematic of OPV, showing key active layers, light absorption, charge separation and charge collection.

amorphous organic materials give rise to their transparent and flexible properties.[4], [5] While OPVs are currently unable to meet or exceed the performance of standard PV devices they have the potential to be a low-cost supplemental technology. One notable example is using transparent OPVs as energy producing window tint for commercial or residential applications.[6]

Transistors are a fundamental and core part of all modern electronics. A transistor can serve one of two functions, it can act as an amplifier switching a small input current into a larger output current, or it can behave like a switch. Transistors accomplish this with four simple non-moving components. A source (positive), a drain (negative), a dielectric material stack between the source and drain, and a gate. The source and drain provide contact to the circuit. When a bias is applied at the gate, the transistor is switched on. The bias applied to the gate causes the dielectric stack to switch from insulating to conducting. This allows the transistor switch to open and closed under the applied bias. TFTs (Figure 2) operate in a similar fashion, however, they are preferred in display applications for liquid crystal displays

(LCD) and active matrix organic light emitting diode (AMOLED) screens because of their ability to be grown as a thin film to reduce total screen thickness. Organic TFTs use organic materials and conductive polymers allowing the OTFT to be produced at a lower temperature and for lower cost.[7,8]

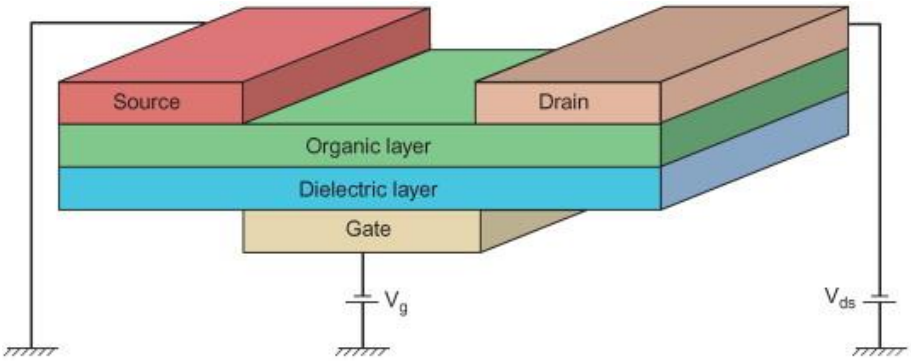

Figure 2: Standard OTFT schematic showing the source, drain, and gate that are required in all transistor devices.

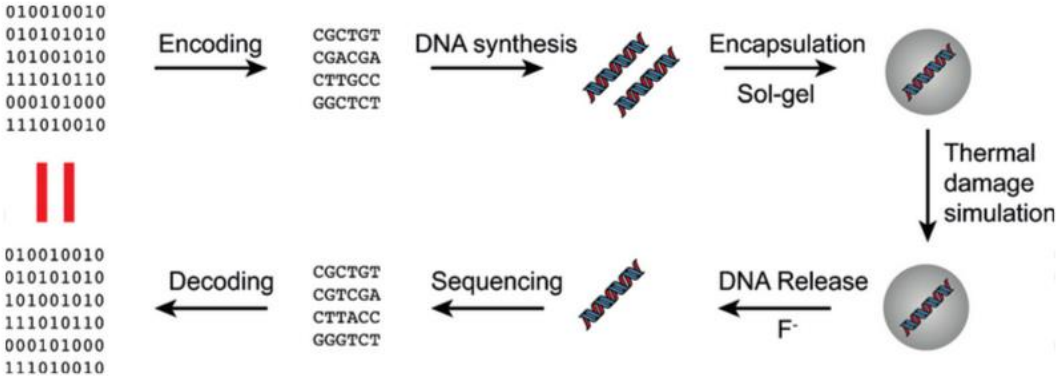

Figure 3: Step by step process demonstrating how DNA can be utilized for mass storage.

Organic memory storage solutions can satisfy such a serious need that mega-corporations like Microsoft are actively supporting research into this field.[9] Current

magnetic storage technology has limited data density and non-ideal storage stability on the order of a few decades. The International Data Corporation has projected that the "digital universe" (all digital data worldwide) will exceed 44 zettabytes (44 trillion gigabytes) by the year 2020. This explosion of data and the need for reliable long-term storage has led researchers away from magnetic storage solutions and toward the emerging field of organic memory storage. DNA has an extremely high raw data density on the order of 10^9 GB/mm^3 with a half-life of over 500 years[10]. Research is currently focused on accurately and quickly reading and writing data into DNA via the process shown in Figure 3. As research continues to progress this technique is likely to have a large impact on informatics and can change the way we store data.

Among the applications of organic electronics, OLEDs are the one technology that is closest to achieving widespread commercial acceptance and use. Many lighting and display manufacturers currently offer a small range of OLED products. Despite this, there is a continued push to achieve the highest possible device performance and make OLEDs a part of everyday life.

1.2: OLED Operating Principals

Organic light emitting diodes are an emerging solid-state lighting technology that has applications that range from general purpose lighting to displays. These devices are comprised of a stack of organic and organometallic layers sandwiched between two ohmic contacts to form a light emitting diode. Diodes are a semiconductor device shown in Figure 4 that consists of a standard P-N junction (Figure 4a) that allows current to flow in only one direction when a voltage bias is applied (Figure 4c).[11,12] This same principle is what occurs in

an OLED device. When a forward bias is applied to the OLED, charge is injected into the device where it recombines to generate light emission. In solid-state lighting devices, the recombination of electrons and holes generates photons via a process called electroluminescence that will be discussed later in this work. For this process to occur charge needs to be able to migrate through the organic layers of the device.[13]

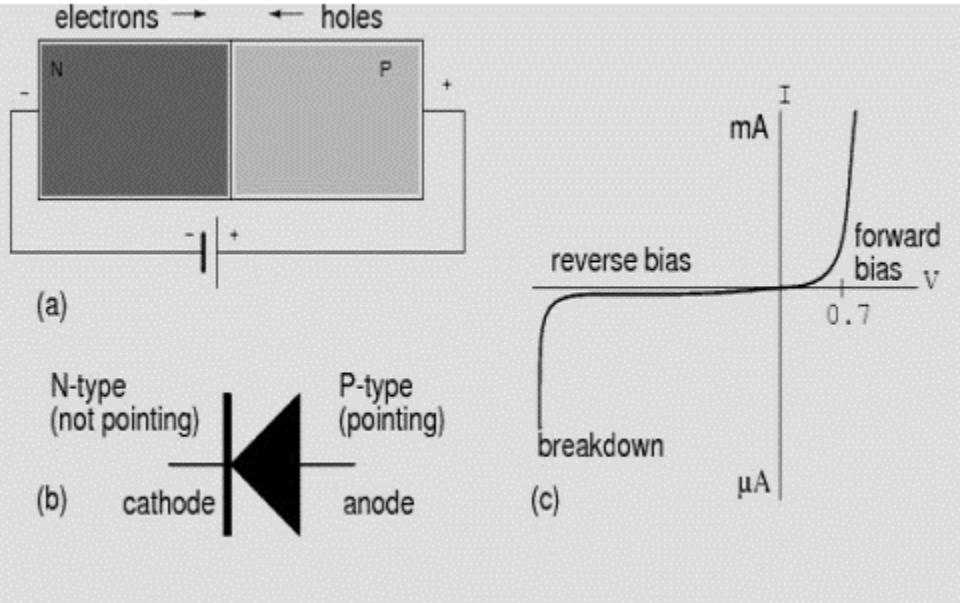

Figure 4: a) standard diode P-N junction in line with a circuit b) circuit schematic representation of diode denoting current flow direction and current stopping direction c) current-voltage curve showing diodes ability to inhibit current flow when under reverse bias and allow current flow under forward bias.

Charge migration in organic semiconductors (OSCs) differs greatly from their inorganic counterparts. Conventional semiconductors (SCs), like silicon, are often a single crystal with very few unintentional defects. This long-range order and close atomic packing allow the material to form bands of electron orbitals known as the conduction and valence band. When an electron resides in the conduction band, or a hole resides in the valence band, the charge is free to move through the material allowing electrical conductivity to occur. Semiconductors are often doped with elements from the III and V groups to provide

an excess of electrons (N-type) or an excess of holes (P-type). These excess charge carriers will reside in the conduction and valence band as shown in Figure 5.

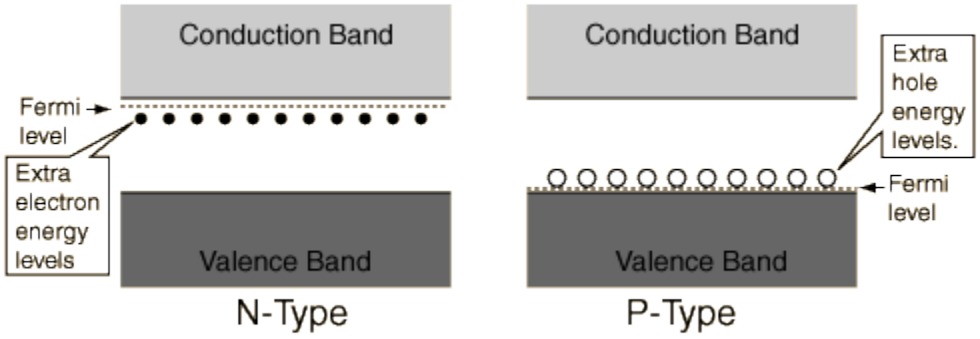

Figure 5: N-doped and P doped inorganic semiconductors showing their conduction and valence bands with free charge carriers.

Conversely, OSCs are typically amorphous materials held together primarily by weak Van der Waal interactions, dipole-dipole interactions or hydrogen bonding. This disorder along with trace chemical impurities that are typically present serve to localize charge on each molecule.[14] This results in the OSCs not having continuous conduction and valence bands. The energy "bands" of an inorganic SC only exist because of their long-range order, periodicity and the alignment of the energy levels across the crystal. In OSCs, the discrete energy levels that are analogous to the conduction and valence bands are known as the highest occupied molecular orbital (HOMO) level and the lowest unoccupied molecular orbital (LUMO) level.[15] These HOMO and LUMO levels are localized on each molecule in the disordered film and while they share similar values to their near neighbor they are unable to share charge as easily as in their inorganic counterpart. Consequently, charge migration in OSC materials is primarily governed by hopping between localized sites.[16] In this method of charge migration, electrons and holes are localized to a single molecule, however, there are many factors that affect the probability of charge hopping to an adjacent state. The

probability of hopping to a specified neighbor is dependent on the distance between the two molecules, the energy of the starting molecule, the energy of the destination molecule, and the ambient electric field.[17], [18] This hopping process also has a dependence on temperature, this is because thermal excitations can raise the local energy of a state preparing to hop making it easier for the hopping to occur to a lower energy neighbor. The dependence of hopping on temperature can be well represented by Mott's law.[19] This hopping mechanism is shown schematically in Figure 6, electrons can be seen hopping along the LUMO levels of the molecules denoted by b in the figure.

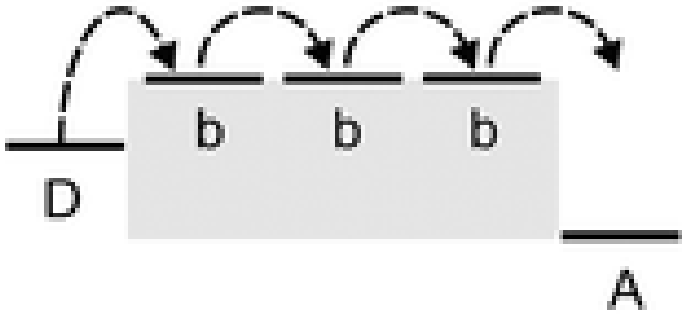

Figure 6: Diagram showing an example of electrons hopping in the LUMO and stopping on the discrete isolated states denoted by (b).

Charge mobility in solids is defined by units of charge flux over a unit area per volt second. OSC mobilities are orders of magnitude lower than conventional SCs. These low mobilities serve to limit the thickness at which OLEDs can be made. While charge mobility would seem to be a problem hindering the development of OLEDs, rigorous material design has continued to improve the quality of materials used.[20]

For the following discussion of excitons, it is important to understand a few concepts about holes and electrons. According to spin-statistics and quantum field theory, electrons are categorized as fermions, particles with half-integer spin. Alternatively, holes do

not physically exist. A hole is a positive charge that remains after an electron is removed from a state. Figure 7 provides a helpful visual representation of these two charged states. Figure 7a shows a molecule in its neutral state, with a net spin of zero, a pair of electrons in its HOMO level and an empty LUMO level. This neutral or ground state represents every molecule in the OLED prior to any external bias being applied. Figure 7b shows a HOMO level that has lost an electron leaving behind a net positive charge on the molecule. This positive charge pulls the HOMO and LUMO closer together and is referred to as a hole polaron. Figure 7c shows a molecule that has gained an electron in the LUMO level and still has a full HOMO level. This causes a net negative charge and is called an electron polaron. When an external bias is applied to the OLED, hole polarons are generated at the anode and electron polarons at the cathode.

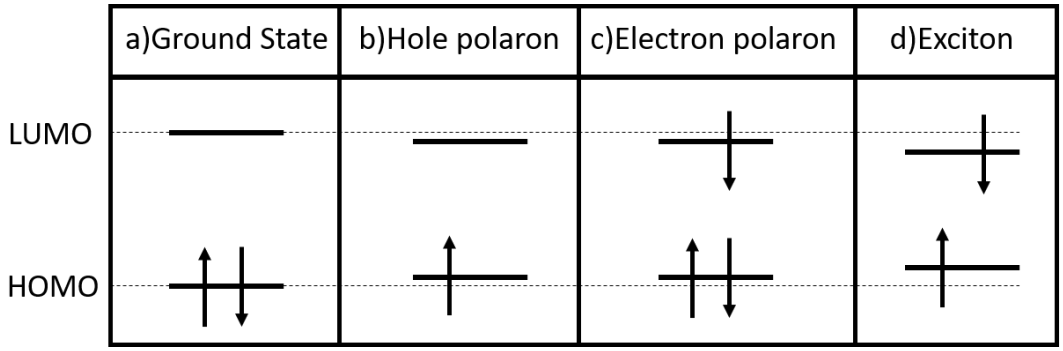

Figure 7: A depiction of HOMO and LUMO level occupation in the 4 different states that a molecule can be in a) Ground State b) Hole Polaron (referred to as a hole) c) Electron polaron (electron) and d) Exciton.

The hole polarons are coulombically attracted to the negative cathode and the electron polarons are drawn to the anode. As discussed, this charge will migrate via hopping towards the center of the OLED device. When the holes and electrons reach the emissive

region, they begin to interact with each other to form excitons Figure 7d. Excitons are coulombically bound electron and hole pairs with binding energy given by:

Equation 1

$$\Delta E(e-h) = \frac{e^2}{4\pi e_o \varepsilon R_c} = k_B T$$

Where ΔE(e-h) is the electron-hole binding energy, e is the electron charge, ε_0 and ε are the respective vacuum and host permittivity, R_C is the critical radius where the Coulomb attraction energy is roughly equal to the thermal energy, k_B is Boltzmann's constant and T is absolute temperature.

The amorphous nature of films in OLEDs leads to Frenkel exciton being formed. Frankel excitons have a smaller radius, higher binding energy and are localized to a single molecule.[21] The Pauli exclusion principle states that two or more identical fermions cannot occupy the same quantum state. This means that any pair of electrons that try to occupy the same state must have opposing spins[22].

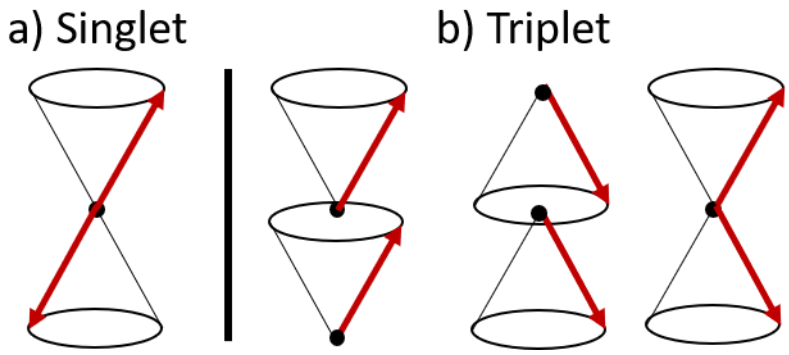

Figure 8: Illustration of exciton types showing spin direction and phase. a) singlet exciton with opposite spin b) triplet excitons with three possible spin conditions.

There are two types of excitons that can be formed, singlet and triplet excitons. When an exciton forms, spin-statistics dictate that there is a 25% chance that the electron spins will be opposing and in phase as shown in Figure 8a. This is commonly referred to as a singlet exciton, it has a net spin of 0 and a short transient lifetime (time in its excited state) on the order of nanoseconds. Alternatively, 75% of excitons that form will have spins that are in the same direction or out of phase, shown in Figure 8b. These are called triplet excitons and can have a net spin value of -1, 0, or 1. Additionally, triplets tend to have longer lifetimes on the order of microseconds. Singlet and triplet excitons will be discussed further below as they are the driving mechanism for fluorescent vs phosphorescent emission.

When an exciton forms on a molecule, despite the exciton binding energy, these charged states are mobile. Exciton diffusion can be explained by one of two main processes. Föster resonant energy transfer (FRET) also called dipole-dipole coupling and Dexter energy transfer or electron exchange. A diagram of the two processes is illustrated in Figure 9.

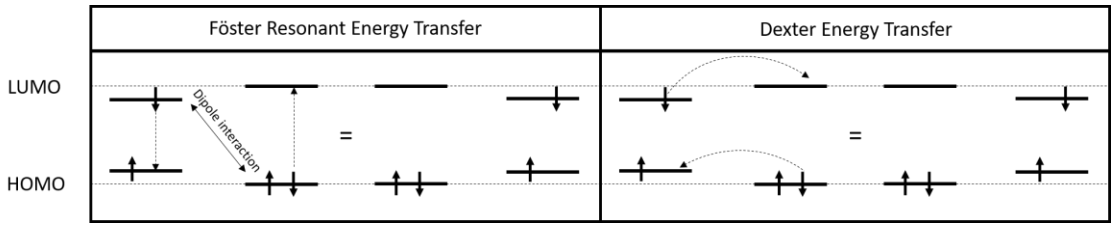

Figure 9: Diagram showing FRET and Dexter energy transfer from one molecule to another.

FRET is a non-contact process that typically occurs on a length scale of 1-10nm. Intermolecular dipole interaction can occur between an excited molecule (M1*) and a molecule at its ground state (M2). When the excited electron in the LUMO of M1* relaxes to the HOMO level its energy is transferred via dipole coupling to an electron in the M2

HOMO level. This results in an energy transfer that excites the electron in M2 to the LUMO level. Conversely, Dexter energy transfer is a direct electron exchange that can only occur when M1* and M2 are in close contact. In this process, the excited electron in M1* hops to the LUMO level of M2. Simultaneously, an electron that occupied the HOMO in M2 hops to the HOMO of M1*. It is worth noting that since this is a contact process it has a much shorter length scale compared to FRET.[23] Of these two processes, FRET is the driving process that occurs in OLEDs and is primarily responsible for exciton diffusion.

OLEDs emit light via a process known as electroluminescence (EL). Viewing this process through the lens of conservation of energy can help to simplify the explanation. Based on the law of conservation of energy, if an exciton relaxes from its excited state down to its ground state the system will have negative net energy. To correct the energy deficit, this relaxation process must be accompanied by the generation of energy equal to the exciton starting energy. In the EL process, this is most commonly satisfied by the generation of a photon.[24,25] Figure 10 illustrates the two main types of electroluminescent emission. Singlet excitons will occupy a higher energy state than their triplet counterparts. In a pure organic system, a singlet exciton decaying from its excited state will generate fluorescent emission.

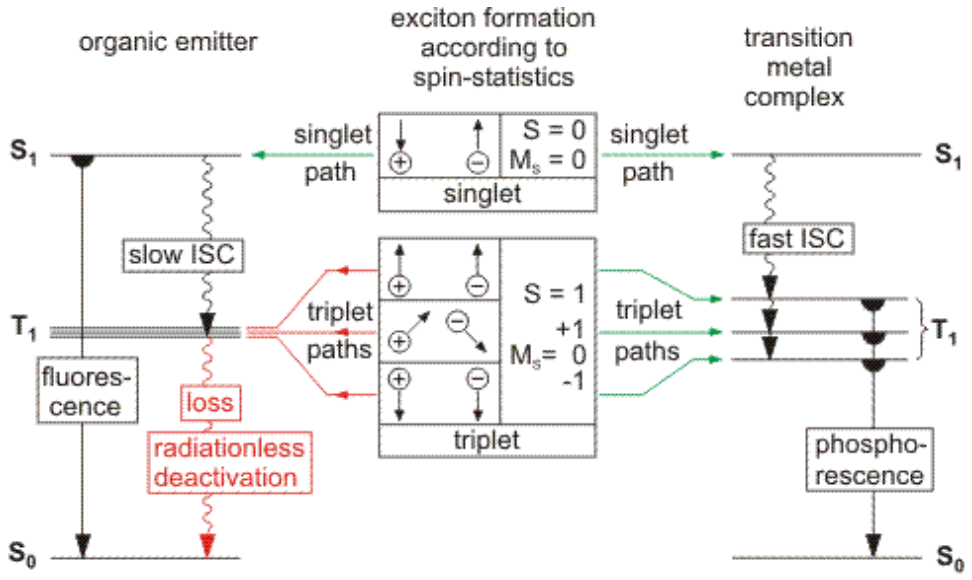

Figure 10: Energy band diagram showing singlet and triplet decay paths that lead to fluorescence and phosphorescence and intersystem crossing (ISC).

A singlet transition from the S1 state to the ground state occurs on a timescale of around 1-100ns. By comparison, the transition from the S1 to the T1 state is significantly slower, ranging from .1 to 1μs. This results in nearly 100% of the singlet excitons decaying radiatively. Unfortunately, in fluorescent systems, all the triplet excitons will decay non-radiatively, Pauli exclusion principle, resulting in a net exciton to photon conversion efficiency of only 25%.[26] Fortunately, the addition of a transition metal atom to the emissive molecule can allow triplet excitons to decay radiatively. This process is known as phosphorescence and is the basis of most modern OLEDs. Spin-orbit coupling between the excitons and the metal atom will allow radiative decay from the T1 state to the ground state. In a phosphorescent system, the S1 to S0 transitions are slower than the S1 to T1 transition resulting in intersystem crossing (ISC). This ISC is a fast and efficient process that leads to phosphorescent emitters being able to achieve an exciton to photon conversion efficiency of 100% by harvesting both singlet and triplet excitons.[27,28] While fluorescence and

phosphorescence are the two primary emission pathways in OLEDs, there has been a growing interest in two unique subsets of fluorescent emission.

Delayed fluorescence occurs when there is reverse intersystem crossing (RISC) causing triplets to be up-converted to the singlet state where they can then decay radiatively. This is classified as delayed fluorescence because a standard singlet will decay in nanoseconds whereas a RISC singlet will decay much slower between microseconds and milliseconds. This delay is a result of the exciton spending a large portion of time in the triplet state prior to being excited to the singlet state. There are two primary ways that delayed fluorescence is achieved. Thermally activated delayed fluorescence (TADF) is a process by which thermal excitations, at room temperature, provide enough energy to cause RISC. This is achieved through judicious material design that reduces the S1-T1 energy gap.[29–31]

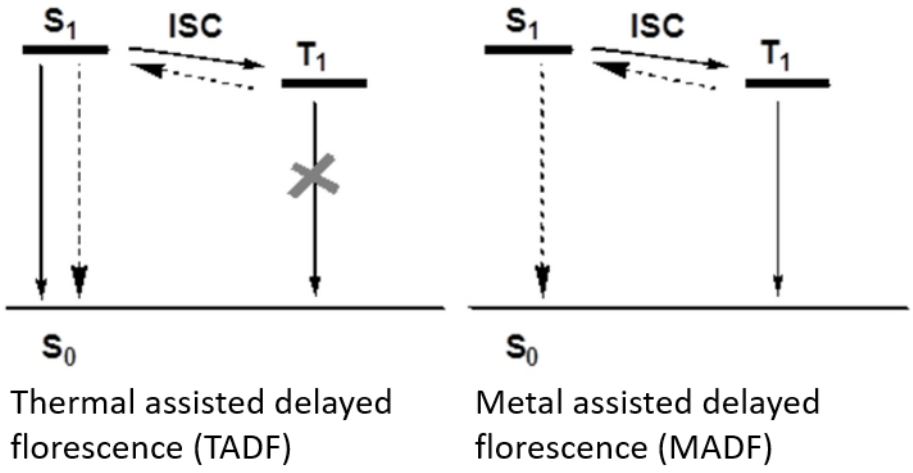

Figure 11: Schematic showing emission pathways of thermal assisted delayed fluorescence (left) and metal-assisted delayed fluorescence (right).

Alternately, in metal-assisted delayed fluorescence (MADF), the RISC is facilitated by the heavy metal atom and thermal energy. MADF emission is accompanied by standard phosphorescence allowing efficient dual emission pathways to coexist. The key differences between these two phenomena are that MADF can still occur at low temperature and has dual emission pathways.[32] These four processes encompass the main mechanisms by which OLEDs generate light.

One of the key valuable traits of OLEDs is their ability to directly emit light over the entire visible spectrum and beyond. This is one key reason why they are a highly sought-after technology for display applications, especially when compared to conventional liquid crystal displays (LCDs). The energy savings achieved by directly emitting colored light vs filtering white light (done in LCD displays), the improved contrast ratio and the improved dynamic color range all point to OLED being the future of displays. To better understand the process that governs the color emission of OLED devices, an energy diagram with more detail than those presented in Figure 10 and Figure 11 must be discussed.

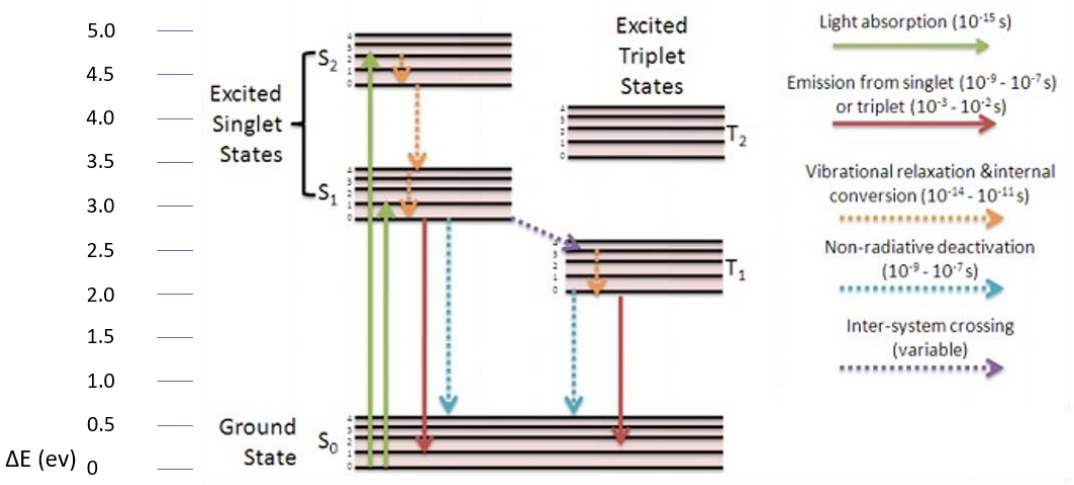

Figure 12: Jablonski diagram showing singlet and triplet excited states with their vibronic bands, average transition timescales, and the ground state.

Figure 12 shows a Jablonski diagram that contains multiple vibrionic states and shows absorption and emission of light with the corresponding time scales. The left-hand side of the figure also shows an energy scale that is used to determine the change in energy of an event.[33] The previous figures discussed are highly simplified to a single S0, S1 and T1 band, however, in complex molecules such as those used in OLEDs, there are a wide range of vibrionic states. When a material in a ground state is excited by an absorbed photon or an exciton, an electron will jump from S0 to S1 or S2 deepening on the energy of the excitation event. Once an electron is in the excited state it will undergo internal conversion, relaxation or intersystem crossing to the lowest S1 or T1 state dictated by the materials parameters previously discussed. When the excited electron decays from S1 (fluorescence) or T1 (phosphorescence) to the S0 state the change in energy between those two states will dictate the emission energy of the photon. Therefore, it is necessary to consider all the vibrionic states that exist in an organic emitter. In an idealized model such as Figure 10 and Figure 11, the existence of a single S0 and S1 state leads to emission that will be monochromic and only entail a single emission energy. However, in a real system, vibration energy, molecular distortions in the emitting molecule and thermal excitations create a wide range of vibrionic delocalized states. This leads to the emission containing multiple energies creating a broader emission profile.

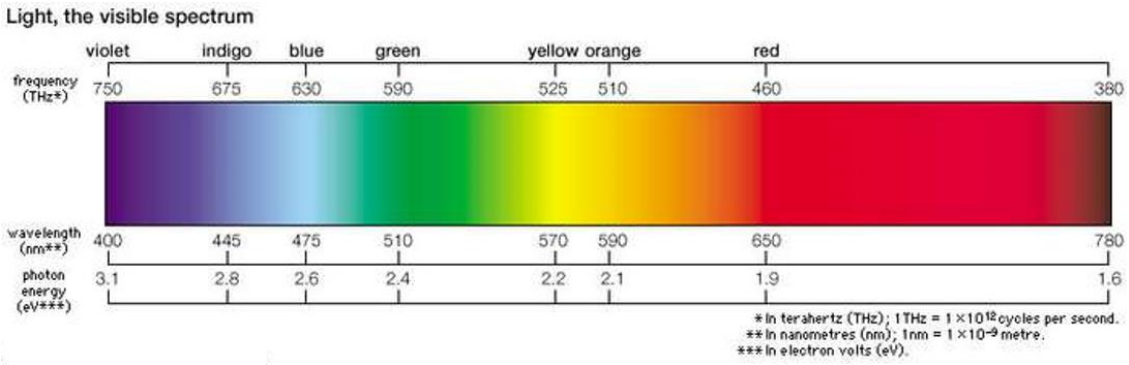

Figure 13: The visible electromagnetic spectrum in terms of wavelength and energy.

The visible electromagnetic spectrum is shown in Figure 13 to provide a visual correlation between the energy, wavelength, and color of the emission. With the fundamental operating principles of OLEDs explained, a more in-depth discussion of device physics and performance can follow.

1.3: Evolution of the OLED

Among the first reports is of electroluminescence in organic solids was published in 1965 by Helfricht and Schnelder. They observed blue emission from anthracene crystals while applying voltages ranging from 40 to over 2000 volts.[34] This demonstration of emission from organic solids sparked further research into the field, however, all the subsequent demonstrations required unpractically high voltages to achieve emission.[35],[36] The first practical demonstration of emission from organic solids and what is now referred to as the first practical OLED was published by Tang and VanSlyke in 1987.

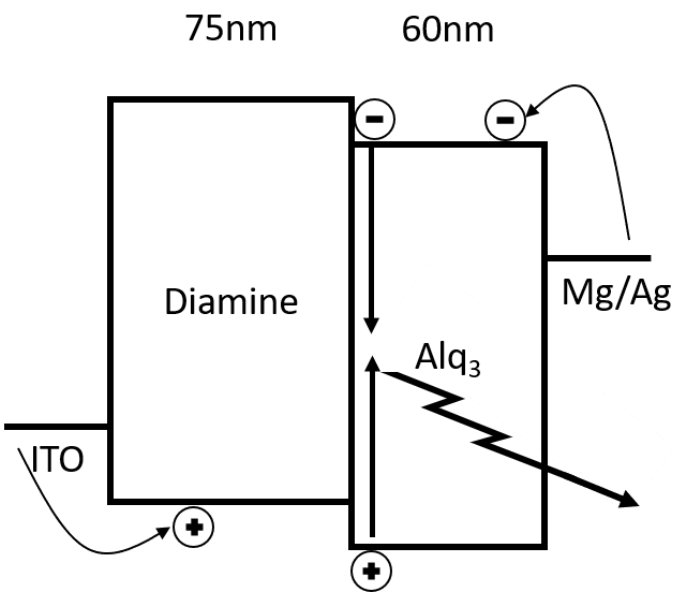

Figure 14: Kodak first OLED by Tang and VanSlyke, a two-layer device using a diamine for hole transport and Alq_3 for emission.

The structure of the first OLED is shown in Figure 14, it consisted of 4 layers total fabricated on a glass substrate. Indium-tin oxide (ITO) is a transparent metal oxide that was used for the device anode. To facilitate the transport of holes from the ITO to the emitting region, 75nm of a nameless aromatic diamine was used. The emitting layer was chosen to be 60nm of tris-(8-hydroxyquinoline) aluminum (Alq_3). Finally, the opaque cathode was selected to be a 1:10 ratio of magnesium and silver respectively. This provided an ohmic contact as well as a back reflector to direct emitted light in the forward direction. Tang and VanSlyke achieved an external efficiency of 1% and demonstrated green emission with the EL peak of 550nm.[13] This landmark publication is now recalled as the first practical OLED device. It demonstrated that electroluminescent emission from an organic solid could be achieved at low voltages and it showed that organic electronic materials could be a viable alternative for many optoelectronic applications.

In the 31 years since this first practical demonstration of OLEDs, research into organic electronics has boomed. The modern OLED structure has changed drastically when compared to the first demonstration over 30 years prior. What will be referred to as a standard OLED structure from this point forward consists of seven active layers between a transparent anode and a reflective cathode. Each of these seven layers serves a specific role that is needed to achieve high-performance OLEDs.[37–42] Figure 15 shows a diagram of the HOMO and LUMO levels of a standard OLED.

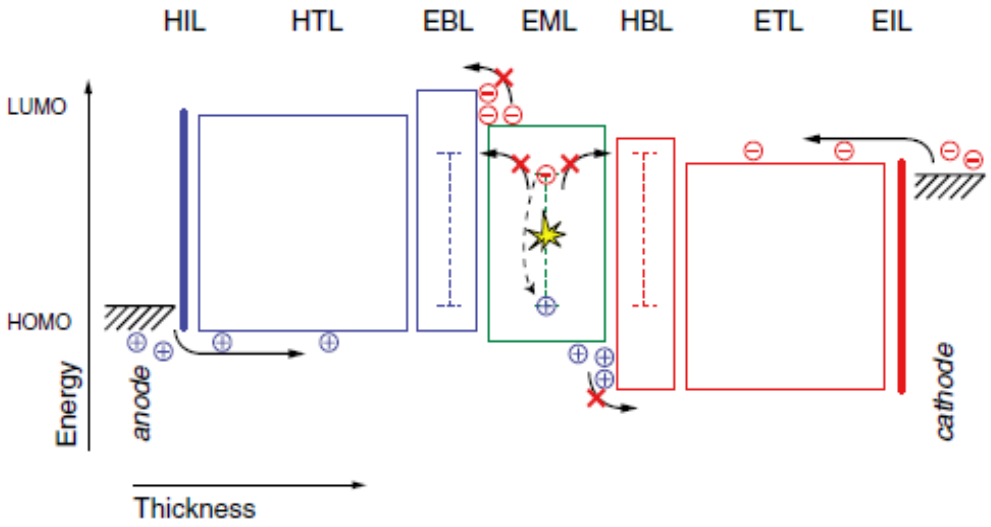

Figure 15: HOMO-LUMO diagram of all 9 layers of an OLED device showing charge injection, transport, and recombination.

Injection layers are placed adjacent to the anode and cathode layers to alter their work function, reduce the charge injection barrier, and generate more charge carrying states. The hole injection layer (HIL) must have a HOMO level similar in energy to the work function of the anode and be able to stably undergo repeated oxidation. This will allow the HIL to easily give up electrons to the anode thereby allowing holes to be injected by the anode. By comparison, the electron injection layer (EIL) is designed to have a LUMO that aligns well

with the cathode's work function and to be repeatably reduced without degrading. This allows for electrons to be injected efficiency into the system.[43,44]

The transport layers are adjacent to the injection layers and serve two functions, to rapidly carry charge through the device and to provide a thickness buffer to reduce the risk of electrical shorts. These materials must be designed to have high electron or hole mobility. The blocking layers are used to confine charge to the emissive layer of the device illustrated in Figure 16. The electron blocking layer (EBL) must be capable of transporting holes and blocking electrons from entering. This is accomplished by designing a material that has a larger HOMO LUMO energy gap. The high LUMO level will prevent electrons from entering and the HOMO level aligns well with the HTL. The same applies to the hole blocking layer (HBL), it must be capable of transporting electrons while blocking holes.

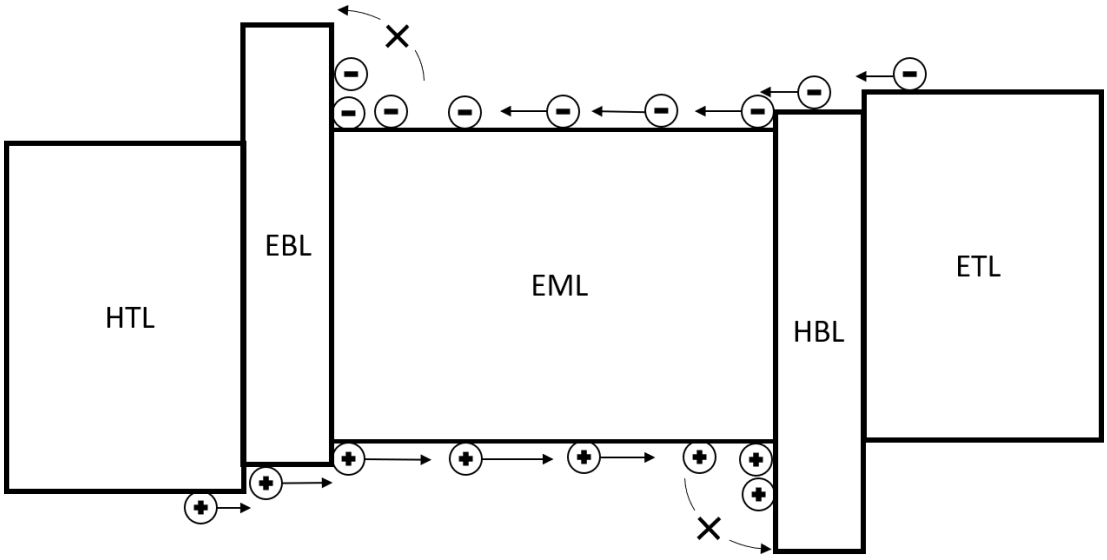

Figure 16: HOMO LUMO diagram of OLED transport, blocking and emissive layers showing electrons and holes moving in the layers.

The emissive layer of the OLED is where the exciton formation and radiative decay occurs. This layer is typically composed of a host and dopant system at a specified weight ratio. The

host serves to transport charge through the layer. The dopant or emitter traps the charge and allows excitons to form and decay radiatively generating the desired light emission. The host must have a larger energy gap than the dopant to prevent the host from emitting, this allows excitons that form on the host to transfer to the dopant before relaxing. This standard OLED structure allows for efficient charge injection and transport.[45,46] The blocking layers confine charge recombination into the emissive layer and the emissive layer is designed to have the highest exciton to photon conversion efficiency possible.

The use of amorphous organic thin films in OLEDs allows for flexibility in their fabrication process. The two most common and successful methods used to fabricate devices are thermal vapor deposition (TVD) and solution processing. Figure 17 shows the key components in the thermal vapor deposition process. Resistive heating sources are filled with organic material and placed in a vacuum chamber with the sample that is to be coated.

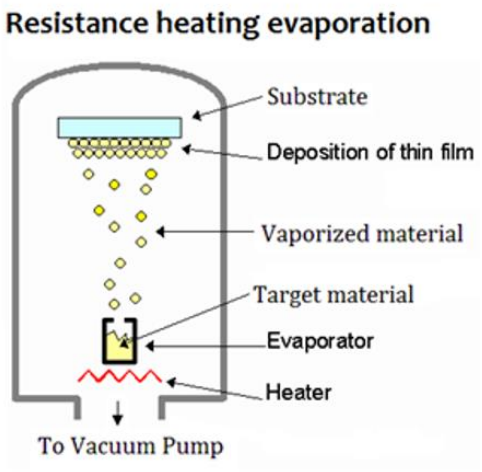

Figure 17: Thermal vapor deposition showing the key components.

Current is passed through the heating element causing the organic material to heat up. The combination of low ambient pressure and high temperature cause the material to

change from a solid or liquid phase into the vapor phase. Even a low vapor pressure is sufficient to generate a cloud of vaporized material that is expelled from the heated source. The vapor cloud condenses on all surfaces that are within line of sight of the source, this includes the sample. This process is controlled using quartz micro-balance thickness motors. These monitors measure the change in oscillation frequency of a quartz sample as mass is deposited on its surface, using density and relative geometry values the monitor can accurately measure the thickness of the material deposited at angstrom resolution. This allows the organic materials to be deposited with specific thickness as thin films for use in the OLED device. TVD is the most commonly used process in commercial applications, however, there has been a recent push to improve the quality of solution processing to reduce the cost of manufacturing.[47]

Solution processing is done by spin coating or blade coating the substrate with a solution containing a solvent and solute (the material you want to deposit). Figure 18 shows a sample being coated with the solution and spun at high speed until the sample dries leaving behind an amorphous layer of the solute. The thickness of the film can be controlled by the spin speed, acceleration and time. This process can also be repeated to build up multiple layers of material. However, care must be taken to use incompatible or alternating solvent systems to prevent the bottom layers from being washed away by the next solvent. Solution processing is more compatible with low-cost, large-scale, roll to roll process like inkjet printing. Further development of this technique can lead to drastically lower production costs of OLEDs.[48]

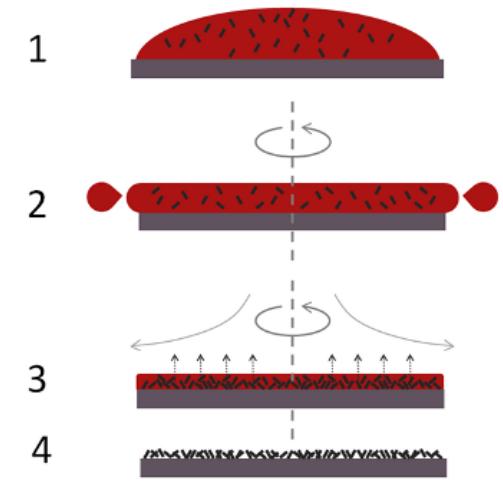

Figure 18: Schematic showing spin coating steps 1) coat 2) spin (low speed) 3) spin (high speed) 4) dry.

1.4: Performance and Characterization of OLEDs:

In this section, the language, terminology, and performance metrics that are used to characterize OLEDs will be introduced and discussed. The most common test that is performed on an OLED is referred to as an IVL test, this stands for current-voltage-luminance. During this test, the diode behavior of the device is probed while the intensity of the light emission is measured. Figure 19a shows a cross-section view of the IVL test procedure, a device is hooked up to a variable voltage source and placed

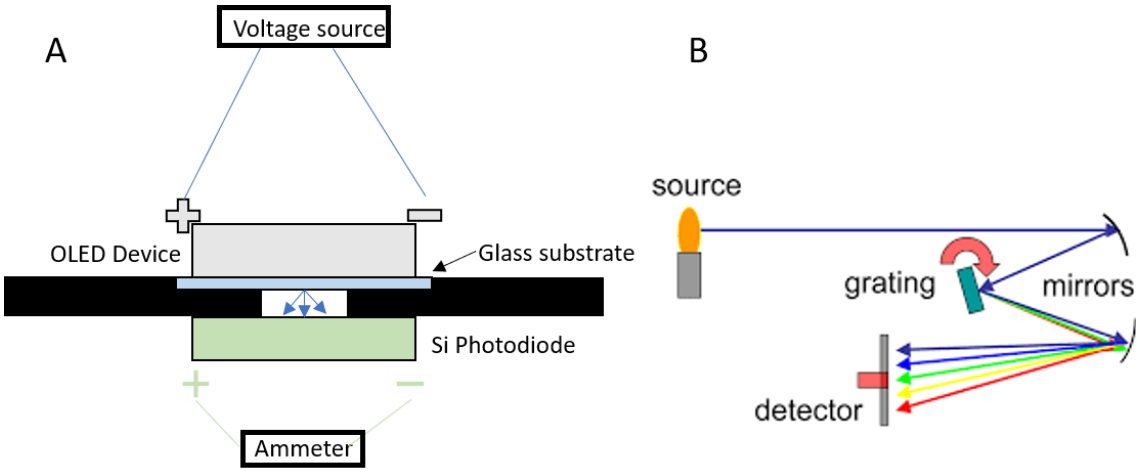

Figure 19: A) Diagram of OLED IVL testing B) schematic of spectrometer operation.

in close contact with a silicon photodiode. The voltage is swept from 0 to a predetermined value usually ranging from 5-20 volts. While the voltage is swept, the current and resistance of the OLED are measured, the emitted light is collected by a silicon photodiode, and the current generated by the photodiode is recorded using a high-resolution ammeter.

Using a spectrometer, the electroluminescent emission spectrum of the OLED is measured. Figure 19b shows a diagram of how a spectrometer measures the incoming light. Using a series of mirrors, the incident light is focused on a diffraction grating. The grating reflects the incoming light at different angles based on the wavelength. The light is then directed to a photodetector that is typically a charge-coupled device (CCD) with a linear array of pixels. This allows for the measurement of the intensity of light vs wavelength. To calculate the brightness of the light emitted from the OLED, the EL spectrum is combined with the silicon photodiodes responsivity curve to convert the photocurrent measured during the IVL test into a value of lumens.

The first device metric that can be calculated from the IVL and spectrum, is called the power efficiency (PE) and has the units lumens/Watt. The power efficiency of an OLED is a useful metric for comparing them to other lighting technologies.

External quantum efficiency (EQE) and internal quantum efficiency (IQE) must be discussed together because they are related values. EQE is a measure of the ratio of photons that escape the device into the air to the number of hole and electron pairs injected into the device. This is estimated by using the current-voltage characteristic to quantify the charge injected and by using the brightness to quantify the photons produced that escaped the device. Unfortunately, the IVL measurement shown in Figure 19a is incapable of collecting all the light emitted from the device, there are losses due to high angle emission that cannot be collected and light reflecting off the silicon photodiode. To avoid undercalculating the device performance, a loss value called the geometry factor is calculated using a calibrated device with known performance. The inverse of the geometry factor ($0<GF<1$) is multiplied by the measured brightness to account for measurement loss. The most accurate way to measure the brightness of an OLED is using an integrating sphere.

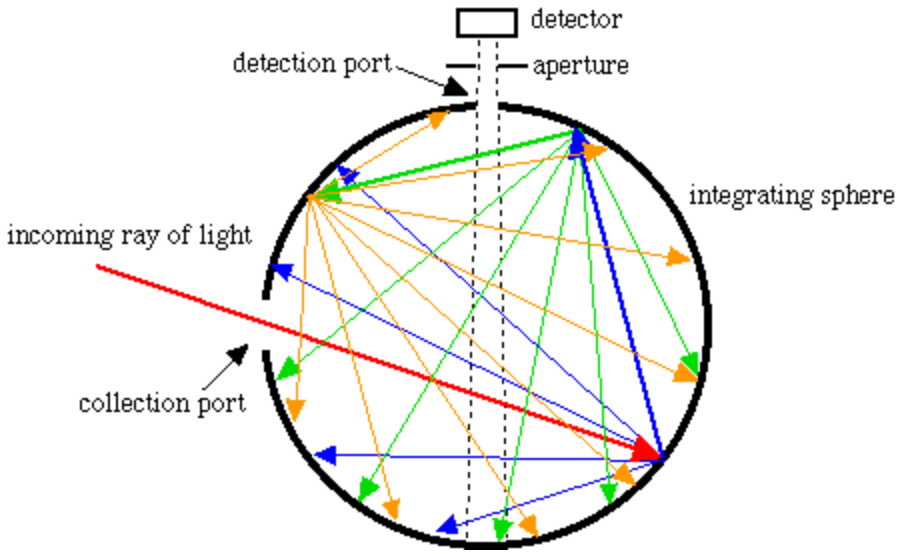

Figure 20: Schematic cross-section of an integrating sphere showing entrance port and detector port.

Figure 20 shows a schematic of an integrating sphere, these spheres are coated with a highly reflective material that can reflect nearly 100% of light across the viable spectrum. The OLED is attached to the outside of the sphere with its emission source up against the collection port of the sphere. All the light emitted in the forward direction will eventually make its way into the detector after many reflections inside the sphere. In some extreme circumstances, the entire OLED device is placed inside the sphere allowing the light emitted in all directions to be measured. Using this highly accurate technique for brightness measurement the EQE of an OLED can be calculated with high confidence.

The IQE of an OLED is a ratio of the number of photons generated in the device to the number of hole and electron pairs injected into the device. By comparison to the previously discussed EQE, the quantification of the IQE is esoteric by nature. There are several techniques that will be discussed, however, many of them must be combined to achieve an accurate estimation of IQE. Before this discussion continues it is worth noting

that this will be a surface level discussion of the techniques involved in this calculation. These techniques will be discussed in more depth later in the presentation. Figure 21 shows the various optical paths that a photon generated in an OLED can take. Otical absrobtion, plasmon quenching and total internal reflection in the organic layers, the transparent conductor (ITO) and the substrate (glass) are responsible for between 70-80% of the emitted light being lost. These optical losses make it extremely difficult to quantify the total number of photons that are electrically generated in the device.

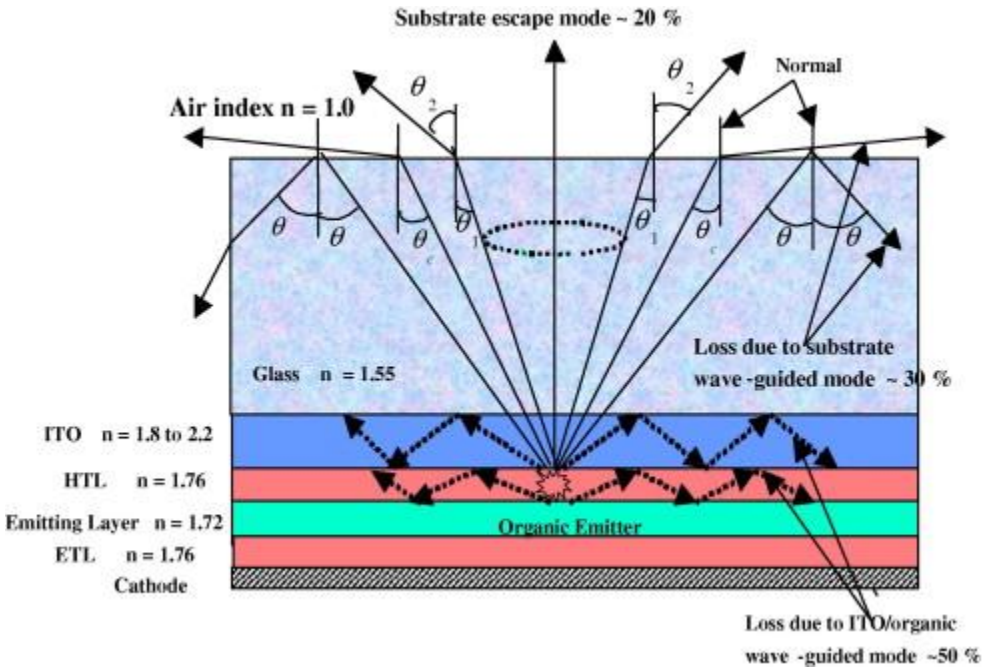

Figure 21: Cross-section view of an OLED showing the major optical loss mechanisms

The first technique that can provide insight into the IQE is called photoluminescent quantum yield (PLQY). Electroluminescence is photon emission via electrically generated excitons, conversely, photoluminescence is photon emission via optically generated excitons. When higher energy light (UV) irradiates a material that is photoluminescent, the material will absorb the light causing electrons to be excited to the LUMO band creating an exciton.

When these excitons relax to their ground state they will emit a photon, similar to the process in electroluminescence. For a PLQY measurement, a sample is placed inside an integrating sphere that is fitted with a high-resolution detector, spectrometer, and a monochromatic light source. The material is illuminated by the light source of known intensity and the resulting signal is collected and processed. From this test, you can quantify the number of photons absorbed by the material based on the original intensity of the excitation source compared with the final intensity of the source. The number of photons emitted from the material can also be measured. This is possible because many phosphorescent OLED emitters have a large stoke-shift (gap between their absorption and their emission) and the absorption and emission of the material will not be convoluted. This measured ratio of absorbed photons to emitted photons will give the PLQY of a material. The PLQY of a material correlates to the IQE, however, photoluminescence and electroluminescence are different mechanisms and they cannot be assumed to have the same efficiencies.

The next technique used to estimate the IQE is optical modeling based on the dipole emission model. This technique allows a device structure with known thickness, emitter orientation, optical constants, and IQE to be simulated with high accuracy. The dipole emission model will construct a device with the emitters and their dipoles oriented in a user-specified manner. This coupled with the knowledge of thickness, optical constants, and IQE will allow simulation of the quantity of light that reaches the air. The optical model on its own will not lead to any significant conclusions unless validated with real OLED devices.

A series of devices can be made where the thickness of one or more layers are varied. If an OLED that has a well know charge confined structure is used, then the only losses in the

device can be assumed to be optical losses. By building an optical to match the devices with varying layer thickness, the model's input IQE value can then be used to make the theoretical and experimental data match. The combination of optical modeling and device testing is currently the best method to achieve a reliable value for device IQE.

Characterizing the stability of an OLEDs emission is crucial to their commercialization. This value must be measured in a standardized way to allow accurate comparison between devices performance. The luminescent decay of an OLED is measured by driving the device at a constant current density (mA/cm^2) and monitoring the brightness decay over time using a silicon photodiode. These values are reported as a time to some percentage decay of the initial brightness. The percentage decay value ranges from 97% (lt_{97}) down to 50% (lt_{50}) and the initial brightness commonly used is $1000cd/m^2$, except during accelerated lifetime tests. For accelerated tests the device is driven at a higher starting brightness, sometimes as high as 10,000-20,000 cd/m^2, this is done to reduce the time needed to screen the device. The stretched exponential decay model published by Féry et al provides a baseline equation that allows an OLEDs lifetime to be estimated from a lower starting brightness.[49]

Equation 2

$$LT(L_1) = LT(L_0)(\frac{L_0}{L_1})^N$$

Where $LT(L_0)$ is the lifetime of the device from a starting brightness of L_0, $LT(L_1)$is the calculated lifetime of the device to a user-specified brightness L_1, and N is the escalation factor. N is dependent on the material system and degradation mechanisms of the device but is widely assumed to be N=1.7, however, this value has been shown to vary.[50]

The final OLED characterization tools to be discussed will relate to the chromaticity of the emitted light. A blackbody radiation source, such as the sun, is referenced as the ideal white light source. An idealized blackbody radiation source can be described by Plank's blackbody spectrum equation:

Equation 3

$$\rho(\omega) = \frac{h\omega^3}{\pi^2 c^3 (e^{\frac{h\omega}{k_b T}} - 1)}$$

Where ϱ is energy density per unit frequency, h is Plank's constant, c is the velocity of light, k_b is Boltzmann constant, ω is the angular frequency, and T is the temperature of the blackbody in kelvin.

The illumination from the sun, as perceived on earth, differs from the blackbody equation above because of absorption effects in our atmosphere. Despite this, the blackbody approximation can still be used to model the ideal white light source.

The color rendering index (CRI) is a metric that compares a light sources ability to render the color of an object to a perfect blackbody's ability to render the color of the same object. This index is assigned a number between 0 and 100 where 0 is no match and 100 is a perfect match to a blackbody. For general lighting applications, a CRI value above 80 is considered a quality light source.

While there are many methods for characterizing the chromaticity of light, the most common is a coordinate plot developed in 1931 by the Commission Internationale del'Eclairange (CIE). This CIE plot uses three imaginary primary colors to match any color of light shown in Figure 22. The primary colors are represented by $\overline{X}(\lambda)$, $\overline{Y}(\lambda)$ and $\overline{Z}(\lambda)$, and

are referred to as spectral tristimulus values (color matching functions). The amount of light each tristimulus contributes is given by:

Equation 4

$$X = \int S(\lambda)\bar{x}(\lambda)d\lambda$$

$$Y = \int S(\lambda)\bar{y}(\lambda)d\lambda$$

$$Z = \int S(\lambda)\bar{z}(\lambda)d\lambda$$

Here S(λ) is the spectral irradiance of the source being characterized.

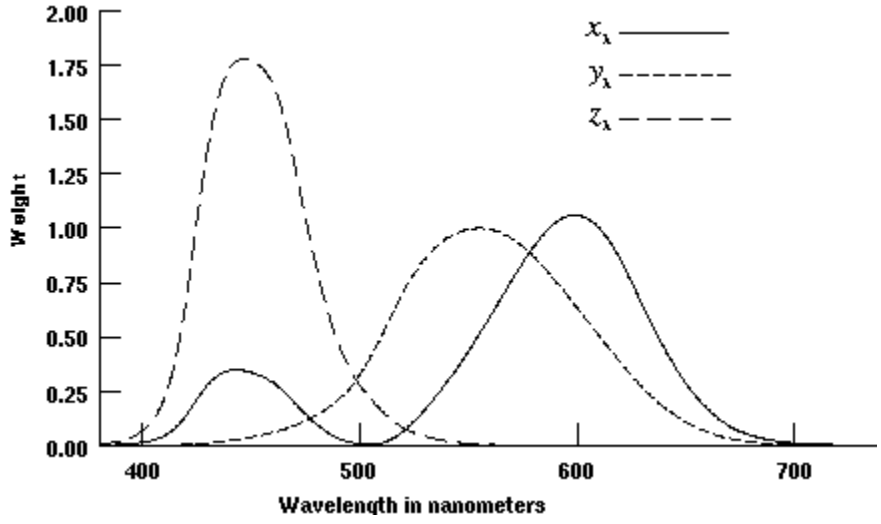

Figure 22: Weighting vs wavelength of the CIE imaginary primary colors $\bar{X}(\lambda)$, $\bar{Y}(\lambda)$ and $\bar{Z}(\lambda)$.

The final CIE chromaticity coordinates can be calculated by the set of equations:

Equation 5

$$x = \frac{X}{X + Y + Z}$$

$$y = \frac{Y}{X + Y + Z}$$

$$z = \frac{Z}{X + Y + Z}$$

$$x + y + z = 1$$

By convention, CIE coordinates are only expressed in terms of x and y, this allows for easy 2D plotting on the CIE plot shown in Figure 23. CIE and CRI provide a standardized method to quantify the color of light and the quality of white light.

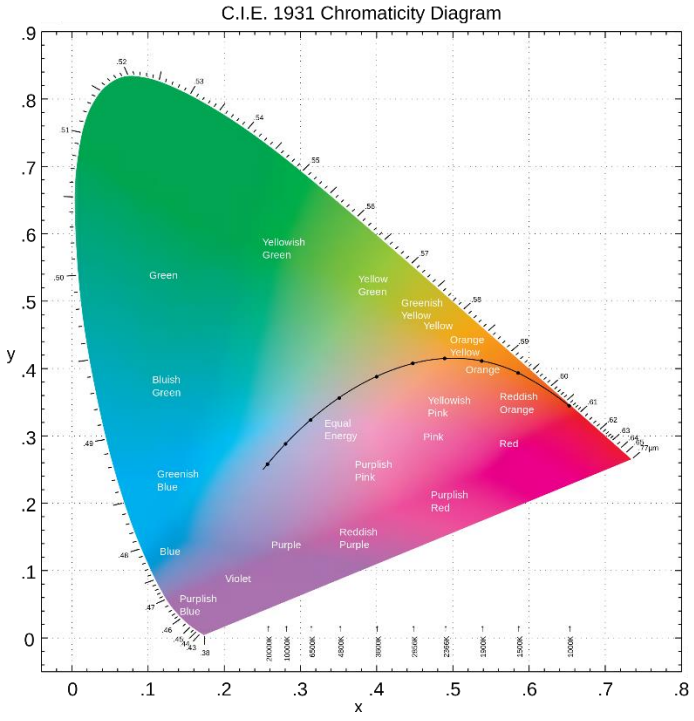

Figure 23: Commission Internationale de l'Eclairange 1931 X-Y chromaticity plot.

1.5: Overview of Mechanisms that Impact OLED Lifetime and Efficiency

OLEDs have two main characteristics that must be improved prior to their widespread acceptance as a new lighting technology. The luminescent decay of devices under operation, and the devices external quantum efficiency. In this section, a brief list of common OLED mechanisms with accompanying descriptions will be presented.

The luminescent decay mechanisms of OLEDs has been widely studied to attempt to understand how to prevent or slow this decay process. Unfortunately, there are so many factors that contribute to this decay rate that no decisive recipe for a stable OLED device has been developed. The processes listed below are well known and reported to lead to luminance decay, however, the relative contribution of each mechanism is highly dependent on process conditions, techniques, materials, and environment.

Dark spot formation and emission area shrinkage:

The emitting area of OLED devices is ideally uniform and constant brightness. Dark spots on the active area are known to form because of cathode delamination or contamination particles within the device.[51] This loss of emissive area will result in a reduction of luminance. Additionally, the edges of the dark spots are generally subjected to a higher current density resulting in higher temperature that can cause the dark spot to grow. It has also been observed that as devices age with or without operation, the edges of the active area can become non-emissive. This is most commonly caused by oxygen and moisture penetration through the organic films. It should be noted that these two processes can happen independently of emissive material degradation, meaning that a dark spot doesn't mean damaged emitters in the dark region.

OLED fabrication concerns:

It has been well researched that the oxygen and water partial pressures during the organic deposition will have a significant impact on the operational stability of a device. Unfortunately, this issue has very little impact on the I-V-L characteristics of the device making it difficult to detect.[52] The presence of oxygen and moisture is particularly harmful when introduced during the emissive layer deposition. The presence of water can lead to oxidation of organic materials followed by hydrolysis of chelation molecules.

Impurities:

Impurities in the organic materials have been known to lower the performance of organic semiconductors.[53] These impurities can reduce charge transport capabilities, create trapping sites and lead to non-radiative exciton decay. A .2% improvement in the chemical purity of an emissive complex has been shown to lead to over a three times improvement in operational stability. [54]

Ion Diffusion:

It has been well studied that indium ion can diffuse into the organic layer from the transparent anode of the device. The presence of these ions in the organic layers can lead to exciton quenching. With Indium having been shown to diffuse at least 100nm quenching of the emissive layer by indium ions is a reasonable possibility. [55]

Non-radiative recombination centers (NRRCs):

The buildup of NRRCs will typically occur in the emissive layer because of poor charge balance in the device. Polaron or exciton buildup will lead to electrochemical degradation of materials that can create trapping sites that form NRRCs. [56]

Dipole reorientation:

Materials that have permanent dipole moments such as OLED emissive materials have been shown to undergo reorientation under applied electric fields. The field strength required to do this is on the order of 1Mv/cm, unfortunately, these fields can be achieved in OLED devices. [57] If dipole reorientation occurs, the device performance can be drastically affected over time.

In addition to the list above of contributing factors consideration of factors such as operation temperature, material glass transition temperature, electrochemical degradation, and photochemical degradation must also be considered. Despite the long list of possible luminescent decay mechanisms OLEDs continue to improve in stability and are approaching the point of wide commercial adoption.

The external quantum efficiency of an OLED is also impacted by several internal and external device parameters. Charge confined device structures can be used to evaluate the efficiency of emissive complexes. These structures are designed with a focus on achieving the maximum rate of charge transport, charge blocking, and radiative recombination. By using this structure the maximum achievable device efficiency can be probed and the IQE of the device can be estimated. For all sections below the IQE will be assumed to be unity.

Material impurities:

Any chemical impurities in the materials used will lead to a reduction in device efficiency. This can result from the formation of traps and non-radiative decay pathways throughout the organic layers. Reductions of charge carrier species in transport layers can also occur. [54]

Recombination zone:

The location of the recombination zone within the OLED structure will have a large impact on the EQE of the device. Centering the exciton formation and recombination region in the emissive layer of the OLED will lead to a reduction of polaron-polaron, polaron-exciton, and exciton-exciton quenching, additionally, quenching of excited states by blocking and transport layers can be prevented. [50]

Dipole Orientation:

The orientation of the emitters dipole moment vectors in relation to the 2D direction of the substrate will alter the optical escape path of light generated in the device. The higher the dipole orientation the less total internal reflection will be experienced. This will lead to a higher EQE in a device setting.

Host selection:

The charge carrying properties of the host-guest system will play a large role in the efficiency of the OLED. The ability to carry both holes and electrons through the EML will lead to an improvement in charge balance that will result in improvements in EQE. [58]

Like what is observed in the stability mechanisms of OLED devices, the EQE is impacted by many interrelated factors. Maintaining awareness of all these factors can lead to an intuitive and educated design of device structure. Unfortunately, many of these mechanisms discussed above cannot be directly measured and must be correlated to actual measurable and observable traits from the organic thin films. The design and understanding of OLED devices have progressed a long way over the past 30 years but still has the potential the be improved further.

1.6: Research Drive:

Organic light emitting diodes are being fervently researched as a replacement for many existing technologies in both the display and lighting sectors. OLEDs have already begun displacing many display technologies ranging from liquid crystal displays (LCDs) to traditional light emitting diodes (LEDs). OLEDs are capable of being processed at lower temperatures making them compatible with a wide variety of substrate materials, ranging from flexible plastics to metal foils. These substrates allow for more rugged displays to be manufactured. In addition to durability, OLEDs offer a simplified device structure when compared to LCDs. LCDs generate images by color filtering a white backlight into the individual pixels that form the final image seen by the user. By contrast, OLEDs directly emit a combination of red, green and blue light for each pixel used to generate the images seen by the user. This leads to lower energy consumption, wider dynamic color range, and deeper color saturation in OLED displays.

OLEDs are also being studied as a potential replacement for conventional lighting technologies such as compact fluorescent lamps (CFL) and LEDs. OLEDs possess many properties that make them valuable to the lighting industry. They do not use environmentally hazardous materials such as mercury, arsenic and lead, they can operate at higher efficiencies, and they inherently produce a diffuse light emission needed for the comfort of the user.

Despite all the attractive attributes that OLEDs possess there are still many key issues that require further research and development. The emission stability of OLEDs needs to be further improved prior to them achieving a wider commercial adoption. Oxygen and moisture absorption into the thin films can cause quenching of the triplet states inside the device's active layers and a breakdown of the electrical properties of the device. These

problems are currently being addressed by used an external capping layer to encapsulate the device and protect it from ambient conditions. The encapsulation concern is further exacerbated when using flexible substrates. Most common plastic substrates are semi-permeable to moisture and oxygen, allowing them to enter the organic layers of the device through the substrate. This has led to research on developing flexible substrates that are resistant to oxygen and moisture, and to find a bottom encapsulation layer that does not reduce the light outcoupling of the device.

OLEDs, like all lighting technologies, undergo luminescent decay while being operated. This occurs from an individual layer's inability to perform its role in the device without breaking down under the applied bias. It is worth noting that material design in the industry has advanced to the point where the primary culprit of short device lifetimes is attributed to the emitting materials and their hosts. For example, blue emitters are still on the order of 20 times less stable than their green or red counterparts. The current, widely reported explanation for this is annihilation between excited states (exciton-exciton or exciton-polaron) in the emissive layer. This process will occur in all device (red, green and blue) and can lead to higher excited excitons or polarons. However, as a result of the higher triplet energy in blue emitter systems, this process can produce excited states that exceed 6.0 eV. When dissipating this higher energy, the dopant or host can potentially undergo a chemical bond dissociation. This process will lead to the degradation of the host and dopant molecules over time inducing non-radiative decay pathways that reduce brightness and efficiency.[59–61]

In addition to the issues with stability OLEDs currently exhibit low external efficiency resulting from poor light extraction in the device. While OLEDs have the

potential to achieve 100% internal quantum efficiency, most devices in a standard structure are limited to between 15-25% external quantum efficiency. Figure 21 shows the primary reason that this occurs, the different refractive indexes of the materials in the device stack lead to 3 main interfaces where larges losses to total internal reflection occur. However, some of these loss mechanisms in the device are recoverable.

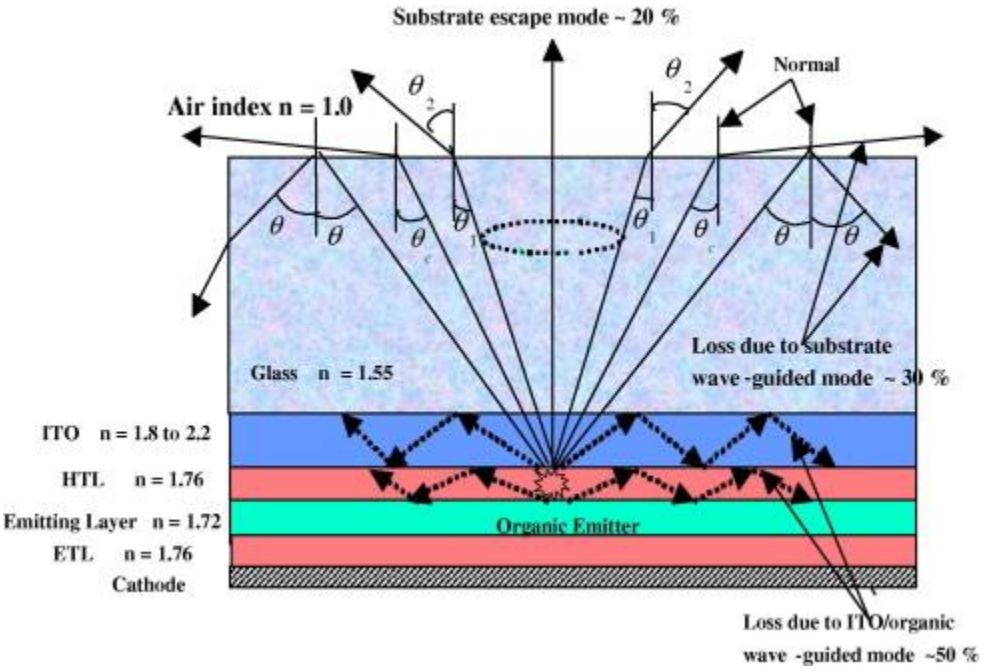

Figure 21: Cross-section view of an OLED showing the major optical loss mechanisms.

There are a variety of techniques for reducing loss mechanisms that range from using materials that have lower refractive indexes, to using micro shaped surfaces to help extract photons that have a high incident angle with the layer interface. These techniques can prove to be useful in improving the optical extraction of the devices. The goal with these techniques is to integrate them seamlessly into the production process while maintaining low cost and high device throughput. While research has demonstrated several techniques that can improve the optical extraction of the device by 1.3 to 2 times, many of these techniques

add significant time and cost the fabrication process.[62] These optical extraction techniques will be discussed further in chapter 4.

2: Improving OLED Performance Through Emissive Layer Design

High-performance blue phosphorescent emitters are currently known as the "holy grail" in the OLED community. This is because stable and efficient blue emitters are needed in almost every OLED device on the market. One large factor limiting the quality and efficiency of OLED displays is their use of low efficiency fluorescent blue emitters. While most fluorescent emitters are limited to IQE's below 25% a phosphorescent emitter can achieve an IQE that approaches unity. This would allow both stationary and mobile displays to operate at a much higher power efficacy, increasing their market value. In addition to displays, OLEDs used for general purpose lighting will experience a similar benefit with the development of higher performance blue emitters. While there are numerous approaches to improving the performance of blue OLEDs, the two techniques that will be discussed are, improving device charge balance through emissive layer design and using phosphorescent emitters to harvest nearly 100% of excitons for conversion to a fluorescent sensitizer.

The standard high-performance OLED structure uses hole and electron blocking layers to confine exciton recombination to the desired emissive region. The use of these layers is well known to improve the EQE and reduce non-exclusive emission (emission from materials other than the dopant) by confining the charge recombination zone. A potential drawback of charge blocking layers is the buildup of charge at one of the blocking layer interfaces. If the OLEDs charge transport properties aren't balanced on both sides of the device, then adding blocking layers will only serve to keep the unbalanced charge confined in the emissive zone.

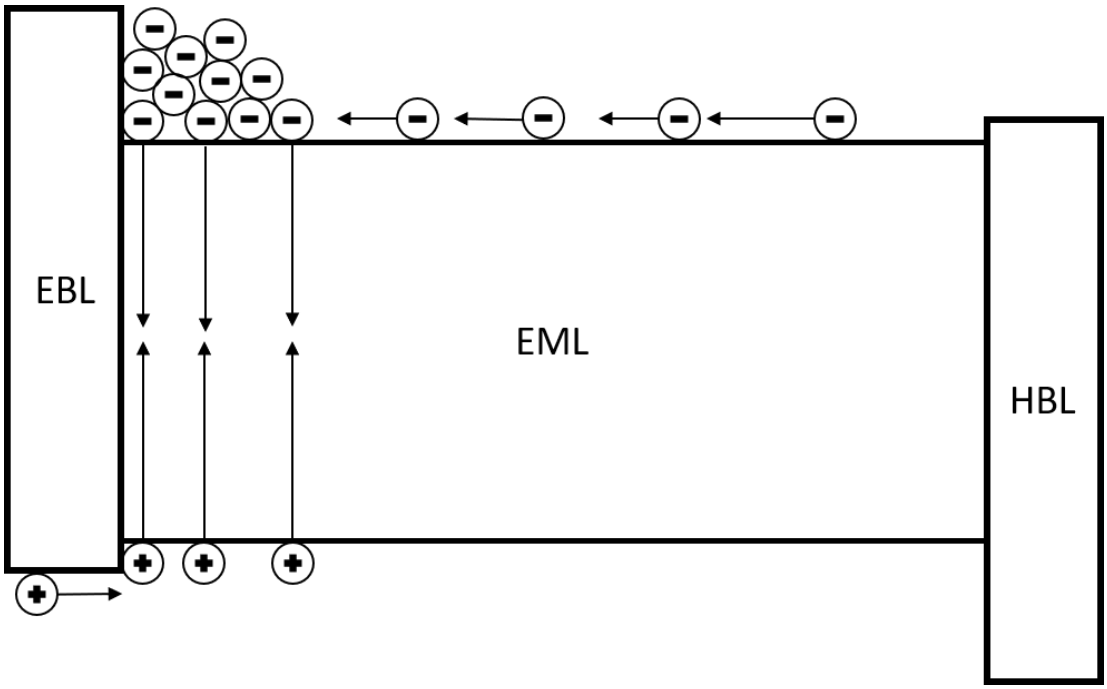

Figure 24: Diagram of electron buildup in the OLED emissive layer, caused by unbalanced charge injection and strong electron blockers.

While this commonly occurs at the EBL, as shown in Figure 24 it can occur at ether blocking layer depending on the charge transport properties of the device and the EML. Charge buildup at blocking layer interfaces has been shown to significantly reduce the device lifetime. A technique is needed to modify the charge balance of the OLED device and center the recombination in the emissive layer. Some recent reports have shown that using a graded emissive layer doping scheme can be used to improve charge balance.[63–66] To unravel the effect that emissive layer design has on charge balance, and by extension stability, a sky blue phosphorescent emitter PtNON and a red phosphorescent emitter PtN3N are studied.

2.1: Improvements in the Stability and Efficiency of OLEDs Through Adept Emissive Layer Design

The photophysical properties of platinum (II) 9-(pyridin-2-yl)-2-(9-(pyridin-2-yl)-9H-carbazol-2-yloxy)-9H-carbazole (PtNON) were investigated under variable conditions.

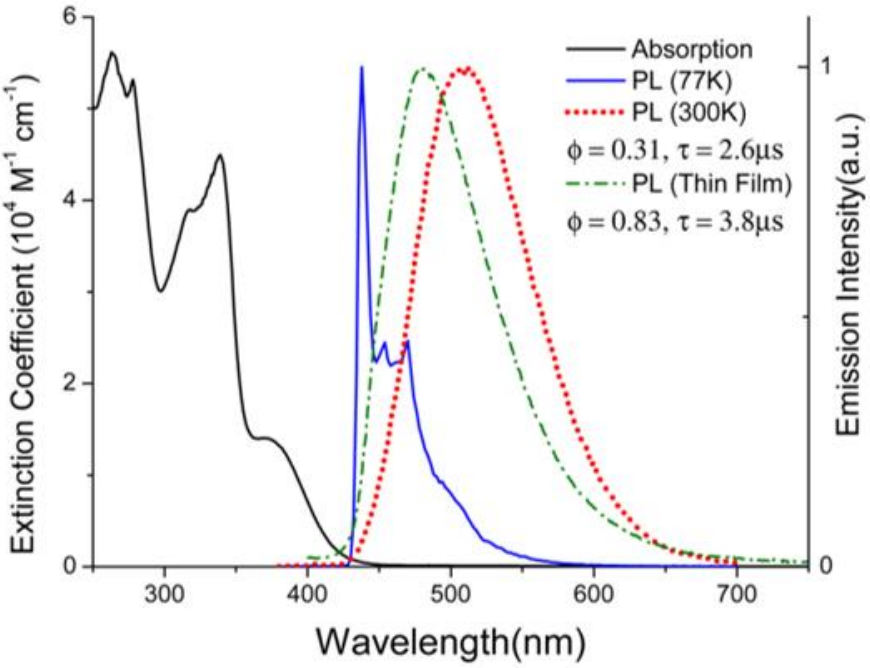

Figure 25: Absorption and emission spectra of PtNON in 2-methyl tetrahydrofuran at 77 K, in a solution of dichloromethane at room temperature and in a doped PMMA thin film at room temperature.

The PL spectrum of a solution of PtNON in 2-methyl tetrahydrofuran was tested at 77K as shown in Figure 25. The emission peak was located at 438nm with two small sidebands at 454 and 470nm indicating a triplet energy of T_1=2.83eV. A solution of PtNON in dichloromethane was then tested at room temperature yielding a much broader featureless emission centered at 508nm. The PLQY of this solution was measured to be 31% with a luminescent lifetime of 2.6μs. Fortunately, when PtNON is doped into a thin film of PMMA at 5% doping concentration the PLQY is increased to 83% and the emission peak shifted to

472nm all while maintaining a short luminescent lifetime of 3.8μs. The short luminescent lifetime and high PLQY in a thin film suggest that PtNON could be a desirable blue phosphorescent emitter for OLED applications.

Subsequently, the EL properties and operational stability of PtNON were studied. A series of devices were fabricated and tested employing a known stable structure with thicknesses and materials as follows, ITO (40nm)/ HatCN (10nm)/NPD (40nm)/Tris-PCZ (10nm) EML (Xnm)/ mCBt (8nm) BPyTP (40nm) LiF (1nm)/ AL (100nm) were ITO is Indium tin oxide, HATCN is 1,4,5,8,9,11-hexaazatriphenylene-hexacarbonitrile, NPD is N,N'-diphyenyl-N,N'-bis(1-naphthyl)-1,1'-biphenyl-4,4''-diamine, Tris-PCZ 9,9',9''-triphenyl-9H,9'H,9''H-3,3':6'3''-tercarbazole, mCBP is 3,3-di(9H-carbazol-9-yl)biphenyl, mCBT is 9,9'-(2,8-dibenzothiophenediyl)bis-9H-carbazole, and BPyTP is 2,7-di(2,2'-bipyridin-5-yl)triphenylene. The only variation between devices 1-4 is the change in the EML doping concentration and thickness (shown below in Figure 26). All four devices showed a sky-blue EL emission spectra peaking around 494nm. The small variation between the FWHM and the peak intensity of the emission profiles can be explained by the addition of high concentration doping regions near the EBL. PtNON in a single emissive layer (device 1) at 6% doping concentration exhibits a peak efficiency of 12.6%. It is worth noting that this performance is significantly lower than the EQE observed in a known charge confined structure. [67]

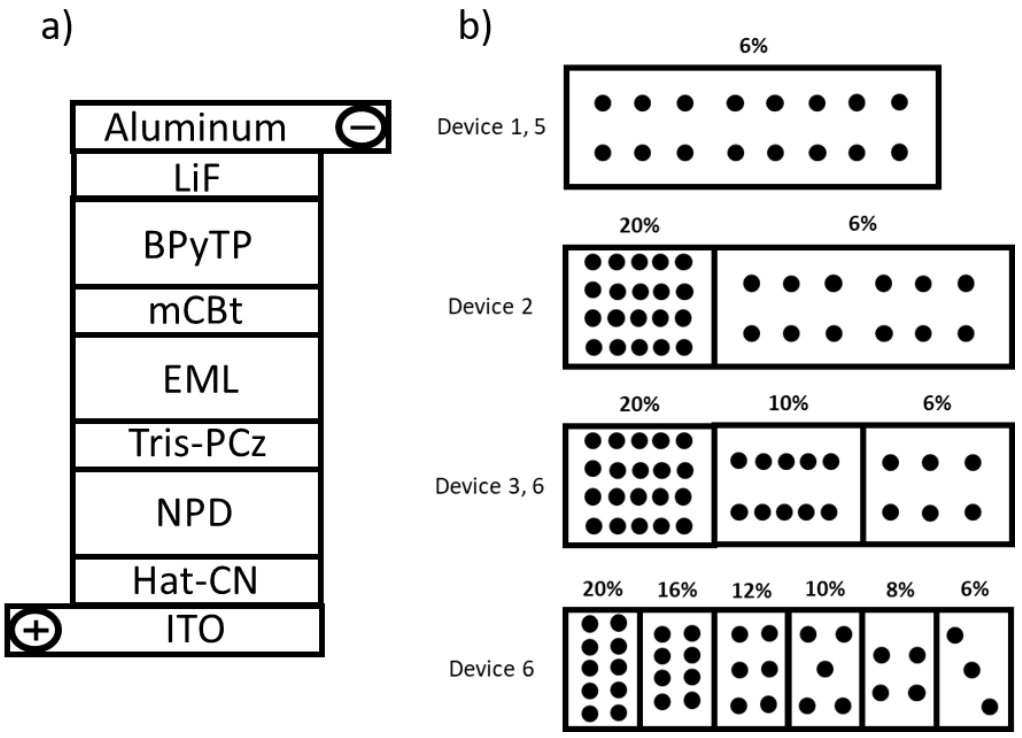

Figure 26 Schematic showing the stable OLED structure used for devices 1-6 and 11-14. Layer thickness is as follows, ITO (40nm), Hat-CN (10nm), NPD (40nm), Tris-PCZ (10nm or 0nm in device 5 and 6), mCBt (8nm), BPyTP (40nm), LiF (1nm), Aluminum (100nm). b) Schematic to visualize the varying doping structure used for device 1-6, Device 1,5 (25nm), device 2, 3, 4 and 6 (30nm).

The drop in EQE results from poor charge confinement and charge balance that commonly arises in stable OLED structures. This device will provide a baseline for device behavior prior to altering the emissive layer structure. To better understand the charge recombination properties of the baseline structure the electron blocking layer was removed (device 5). The comparative performance of these devices is shown below in Figure 27. Device 5 exhibits a blue shift in its peak EL intensity with an increased emission between 400 and 450nm. This emission is attributed to exciton recombination in the NPD layer. The removal of the EBL allows electrons and excitons to diffuse into the hole transporting layer. This is further supported by the reduction in EQE visible in Figure 27b's insert. The reduction in charge

confinement and subsequent fluorescent emission from NPD will result in lower device efficiency and brightness.

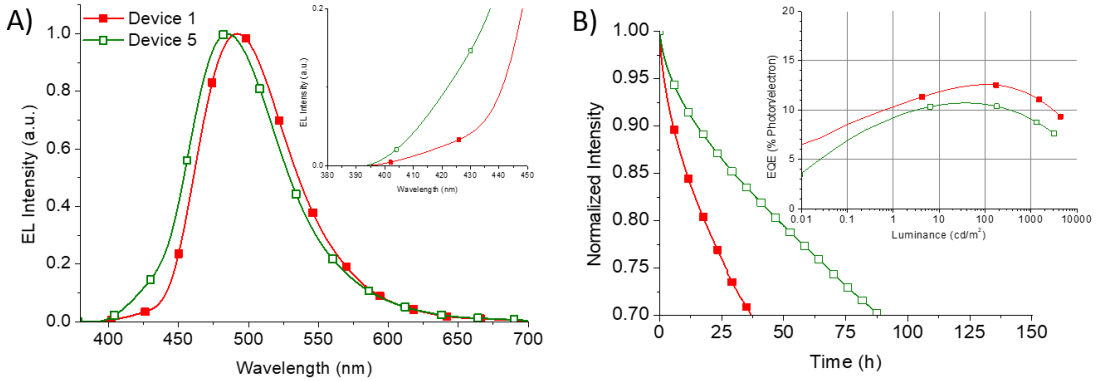

Figure 27: A) EL intensity vs wavelength with inset graph showing an enhanced view of the blue region below 450nm B) Normalized intensity vs time with figure inset showing EQE vs luminescence curve.

Finally, the removal of the EBL in device 5 served to more than double the lifetime of the device run at a constant current density of 20mA/cm^2 from 37 hours up to 88 hours. This behavior supports the idea that poor charge balance is partially responsible for PtNON's non-ideal performance, and that charge buildup is occurring at the ELB as shown in Figure 24. As a result of PtNON's bi-carbazole ligand structure and its HOMO level of 5.1 eV (see Figure 28) PtNON has the potential to improve hole injection and transport in the EML if the dopant concentration is increased. To alleviate charge buildup at the EBL interface a 10nm 20% PtNON:mCBP layer was added (device 2). This structure had a substantial impact on the device efficiency and roll-off, raising the peak EQE to 17.6% and the EQE at a high brightness of 1000 cd/m^2 to 16.8%. Figure 29 shows the normalized intensity vs operational lifetime at a constant current of 20mA/cm^2.

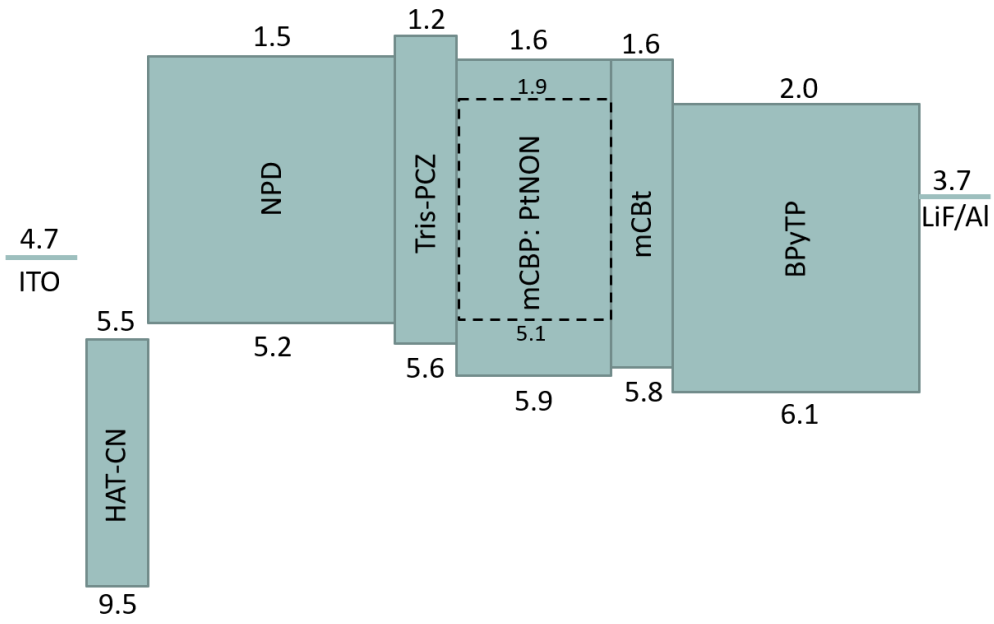

Figure 28: Stable OLED structure showing HOMO and LUMO levels.

Despite the significant improvement in both EQE and brightness, device 2 exhibits low operational stability with a lifetime to 70% of its initial luminance (LT_{70}) of only 14.3 hours. The large change in starting brightness can skew constant current lifetime comparisons, therefore the lifetime values have been calculated from a starting brightness of 1,000 cd/m^2 using the stretched exponential formula (Equation 2). Device 2 has a LT_{70} at 1,000cd/m^2 of 378 hours and Device 1 has a LT_{70} at 1,000 cd/m^2 of 466 hours. We believe this drop in the lifetime to be a result of the large change in doping concentration from 20% to 6% causing discontinuous charge transport characteristics within the emissive layer. The discontinuity can lead to an interface within the EML where charge-buildup can occur. As a result, excitons and polarons form in higher concentration at the EBL-EML interface and at the 20%-6% dopant interface leading to faster degradation and reduced lifetime.

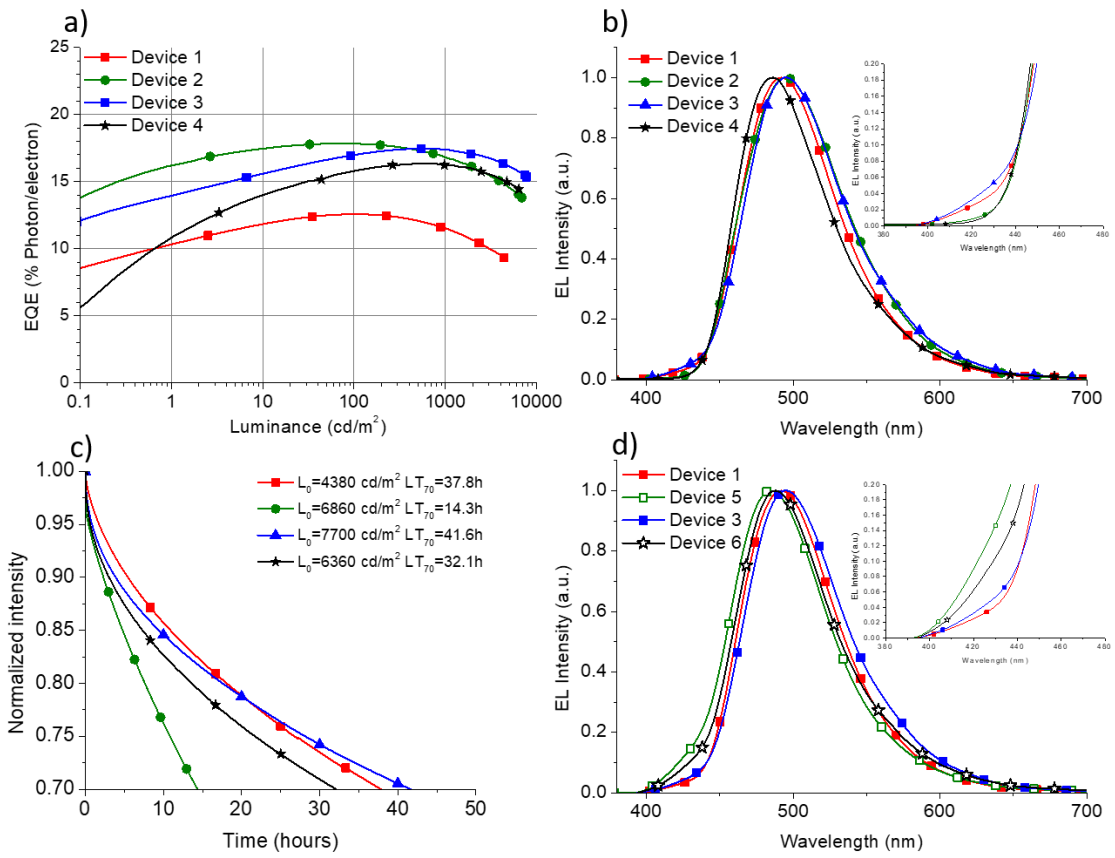

Figure 29: a) EQE vs Luminance plot of devices 1-4, b) EL spectra with subplot showing emission in the 380- 480nm wavelength range, c) Normalized relative intensity vs operational lifetime at constant current of 20mA/cm², d) EL spectra with subplot showing emission range between 380-480nm comparing key devices with and without an electron blocking layer.

Device 3 was designed to reduce the discontinuous charge transport properties in the EML to solve the issues observed in Device 2. By placing a 10% doped layer between the 20% and 6% layers we aim to alleviate charge buildup inside the EML and allow for excitons and polarons to diffuse deeper into the emissive region. This structure demonstrated an efficiency that peaks at a high brightness of 1,000 cd/m^2 of 17.4%. In addition to high efficiency, the three-layer structure shows a significant improvement in stability with LT_{70} of 41.6 hours under a constant 20mA/cm^2 drive current and LT_{70} 1,000 cd/m^2 of 1337 hours. As the dopant concentration stepping size between the layers in the EML decreases we can

observe improvement in the EQE, roll-off, and stability of the blue device. Figure 29d compares the EL spectra of the single layer and three-layer emissive device with and without a 10nm Tris-PCZ electron blocking layer. The subplot shows the presence of a deep blue emission between 400 and 450nm attributed to emission from the HTL (NPD). Like in Figure 27b this is a result of the exciton formation zone being located and the EBL-EML interface. Shifting the exciton formation region deeper into the emissive layer and away from the EBL-EML interface will result in a reduction of the deep blue emission even when an EBL is not present. By comparing the single layer and triple layer devices without electron blocking (device 5 and 6 in Figure 29d) we can see from the subplot that the amount of NPD emission drops significantly. This reduction can be correlated to improved charge confinement and a shifting of the exciton formation zone away from the EBL EML interface.

To further improve the performance, device 4 was designed to spread the exciton and polaron recombination zone across the widest possible region of the EML. This was done by using 6 steps of gradually decreasing dopant concentration from 20% to 6%. It is worth noting that there is published work that uses continuously varied EML's to achieve similar results.[63–66] However, that technique is difficult to control, reproduce and is not compatible with large-scale manufacturing. For this reason, we believe that using individual steps is a more repeatable way to achieve the benefits of variable doped EMLs. This device resulted in a drop in peak EQE to 16.3% at 1,000 cd/m^2 as well as a reduction in the operational stability of LT_{70} to 32.1 hours and LT_{70} 1,000 cd/m^2 to 745 hours. The notable drop in device performance could be caused by the multiple interfaces inside the emissive layer. Each pause in the vapor deposition can result in a higher concentration of contaminants forming at the surface of the deposited layer. Consequently having 5 of these

contamination layers vs 2 (in the previous device) inside the EML can create many more pathways for nonradiative decay causing the observed reduction in device performance.

It should be noted that the previously mentioned, known charge confined structure with PtNON had an EQE at 1,000 cd/m^2 of 17.5% and a power efficiency of 17.8 Lm/W (Lumens/Watt). The multilayer OLED structure employs the same material system as the single layer structure and only changes doping concentration and thickness. This results in a relatively small change in manifesting cost, however, there is a 2.8 times increase in device stability while nearly doubling the luminous efficiency from 15.8 Lm/W to 28.2 Lm/W at 1,000 cd/m^2. Additionally, this device outperforms its known charge confined counterpart suggesting that it is nearing the optimal charge balance. To the best of the author's knowledge, this is the most stable and efficient demonstration of a single stack, sky-blue OLED to date. Despite all these improvements, PtNON's emission color is not deep enough of a blue to be used in display settings. However, because of its high triplet energy, there is still room for improvement in the color quality of this device.

2.2: Improving the Emission Color Quality Using Florescent Blue Emitters

2,5,8,11-Tetra-tert-butylperylene (TBPe) is a widely used and well-studied blue fluorescent emitter with an emission peak at 462nm, and a singlet energy S_1= 2.59eV estimated from its peak emission at 77K. With the singlet energy of TBPe residing below the triplet energy of PtNON, there is a strong probability that foster resonant energy transfer (FRET) will occur from PtNON's T_1 state to TBPE's S_1 state. This process is outlined in an energy level diagram shown in Figure 30**.** If this process can be carried out efficiently, the PtNON will harvest triplet excitons and transfer them to TBPe for emission. This can allow the 25%

IQE cap of fluorescent emitters, like TBPe to be surpassed, improving the emission color quality and stability of the PtNON system.

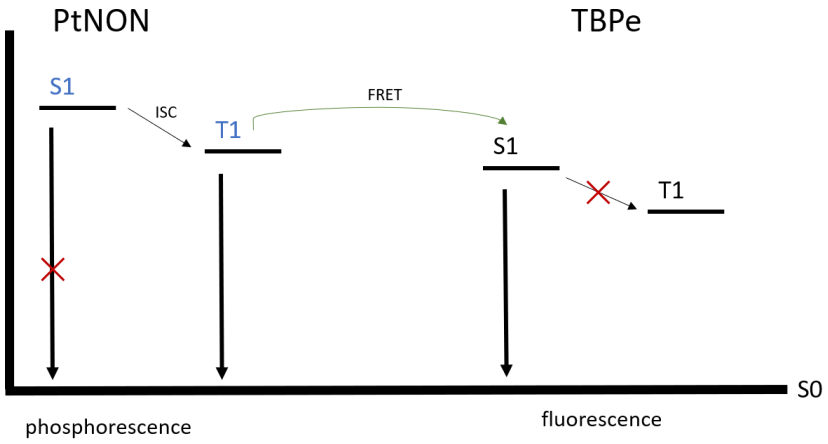

Figure 30: Energy level diagram interpretation of TBPe and PtNON interaction. PtNON is a phosphorescent emitter with a high triplet energy above TBPe's singlet energy. FRET can allow triplets harvested on PtNON to be transferred to TBPe and emit from the singlet state. Because of PtNON's high IQE, this process can result in fluorescent emitters emitting with an IQE above the theoretical limit of 25%.

The efficiency of the energy transfer process must first be investigate in a device setting. Figure 31a shows the know charge confined structure with the thicknesses of: ITO (40nm), Hat-CN (10nm), NPD (40nm), TAPC (10nm), EML (Xnm), DPPS (10nm), BmPyPB (40nm), LiF (1nm), Aluminum (100nm) where TAPC is di-[4-(N,N-di-tolylamino)-phenyl]cyclohexane, DPPS is diphenyl-bis[4-(pyridin-3-yl)phenyl]silane, and BmPyPB is 1,3-bis[3, 5 di(pyridin-3-yl)phenyl]-benzene. Figure 31b shows the EML structure of device 7-10. 7: 10% PtNON in mCPy26 (25nm), 8: 10%PtNON:1%TBPe:in mCPy26 (25nm), 9: 10% PtNON:2% TBPe in mCPy26 (25nm), 10: 10%PtNON: in mCPy26 (4nm), 2% TBPe in mCPy26 (2nm), 10%PtNON: in mCPy26 (4nm), 2% TBPe: in mCPy26 (2nm), 10%PtNON: in mCPy26 (4nm) where mCPy26 is 2,6-bis(N-carbazolyl) pyridine.

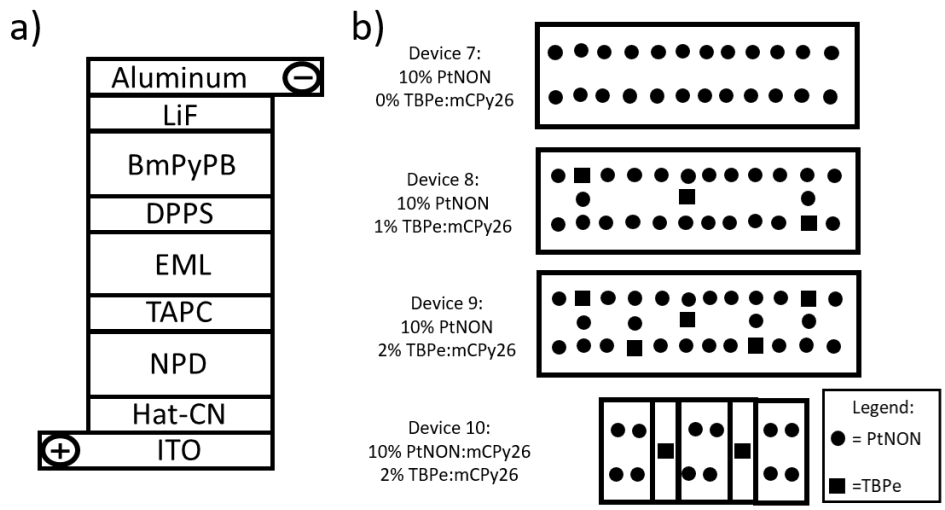

Figure 31: a) Schematic showing charged confined OLED structure used in device 7-10, layer thickness are ITO (40nm), Hat-CN (10nm), NPD (40nm), TAPC (10nm) DPPS (10nm), BmPyPB (40nm), LiF (1nm), Aluminum (100nm). b) EML structure of device 7-10, 7: 10% PtNON in mCPy26 (25nm), 8: 10%PtNON:1%TBPe:in mCPy26 (25nm), 9: 10% PtNON:2% TBPe: in mCPy26 (25nm), 10: 10%PtNON: in mCPy26 (4nm), 2% TBPe: in mCPy26 (2nm), 10%PtNON: in mCPy26 (4nm), 2% TBPe: in mCPy26 (2nm), 10%PtNON: in mCPy26 (4nm).

Device 7 is 10% PtNON in mCPy26, this establishes a baseline of PtNON's performance and color before the introduction of the fluorescent sensitizing agent. This device has a broad forward directional EL spectrum that peaks at 496nm with a peak EQE of 20.3% with an EQE at 1000 cd/m^2 of 17.6%. Device 8 is a 10% PtNON:mCPy26 device that is co-deposited with TBPe at 1%. The introduction of TBPe resulted in a drop in peak EQE from over 20% down to 15%, with an EQE at 1000 cd/m^2 of 10%. Despite the drop in efficiency, the peak EL emission of this device shifts significantly with the introduction of TBPe. The new emission color peaks at 466 nm and closely resembles pure TBPe emission. This suggests that nearly all the emission from this device is being generated by the low concentration of TBPe in the system. Device 9 is a 10% PtNON:mCPy26 device that is co-deposited with a higher concentration of TBPe at 2%. As the TBPe concentration is

increased there is a continued reduction in device efficiency, device 9 has a peak EQE of 12.4%

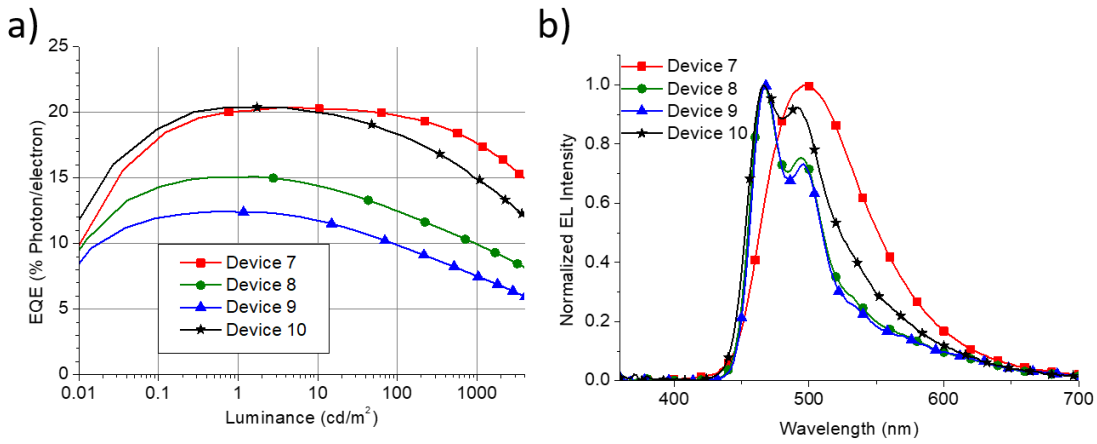

Figure 32: a) EQE vs Luminance, b) EL spectra measured at 1mA/cm² of devices in charge confined structure.

with an EQE at 1000 cd/m² of 7.5%. The reduced efficiency likely results from self-quenching of the TBPe. This is common in devices that employ fluorescent emitters and is generally avoided by using fluorescent doping concentrations less than 1%. [68] Additionally, there was little change in the EL spectrum with the increased TBPe concentration, further enforcing the claim of near-exclusive TBPe emission in device 8. To avoid the issues of self-quenching in the co-deposited structure, device 10 uses a layered structure with thin TBPe:mCPy26 layers. Device 10 has a peak EQE of 20.3%, the same as device 7 when no TBPe is present, and an EQE at 1000 cd/m² of 15%. Although the EL peak position remains unchanged the ratio between the main peak at 466nm and sideband at 492nm change. The increase in the sideband peak is attributable to PtNON emission in the system. Despite the increase in PtNON emission, device 10 demonstrated improved color and similarly high efficiencies when compared to the PtNON only device.

To further explore the potential of this material system TBPe layers were introduced in the stable and efficiency three-layer structure used in device 3 (Figure 26b). In order to minimize the self-quenching of TBPe, 2nm layers of 2% TBPe: mCBP were strategically placed in the EML. The doping scheme and performance of these devices is shown below in Figure 33, these devices employ the same stable structure used for devices 1-4.

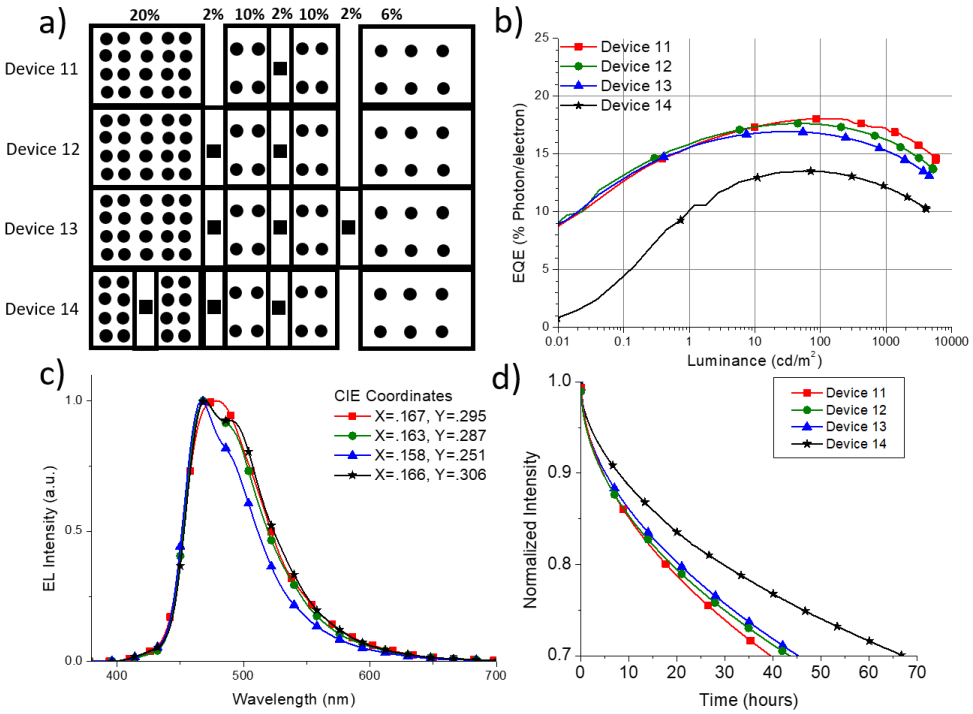

Figure 33 a) Schematic showing the doping scheme for devices 11-14, b) EQE vs Luminance for devices 11-14, c) EL spectra of devices 11-14 with respective CIE coordinates, d) Normalized relative intensity vs operational lifetime at a constant driving current of 20mA/cm^2.

Device 11 has a single TBPe layer inside the 10% doped PtNON layer and shows a peak EQE of 18% and an EQE at 1000 cd/m^2 of 17.1%. The addition of this single layer of TBPe did impact the EL spectrum by shifting the peak emission to 478nm. Along with a peak shift, the full width half maximum (FWHM) of the emission spectrum is narrowed from 76nm to 70nm. The peak shift, narrowing of the emission profile and the Gaussian

shape of the emission profile suggest a system where both PtNON and TBPe are strongly emitting. The stability of the device under accelerated testing conditions is 39.5 hours at 5700 cd/m^2 with an estimated Lt_{70} at 1000 cd/m^2 of 761 hours. It is worth noting that changes in the emission color of devices make comparing the calculated lifetime at 1000 cd/m^2 less meaningful. This is because the change of emission color will impact photopic response that contributes to brightness calculations. This will lead to deeper blue devices having a lower calculated brightness that will lead to a lower lifetime at 1,000 cd/m^2. To circumvent this issue the lifetime at a constant current of 20mA/cm^2 will be compared to determine device improvement.

Device 12 has the same TBPe layer inside the 10% PtNON layer as before with the addition of a 2nm 2% TBPe layer between the 20% PtNON layer and the 10% PtNON layer. This device has a peak EQE of 17.6% and an EQE at 1000 cd/m^2 of 16.2%, with a Lt_{70} of 43 hours at an initial brightness of 5200 cd/m^2. The EL peak is shifter further than device 11 to 468nm, however, the FWHM is unaffected and remains 70nm. The shift in peak height suggests that the addition of the second TBPe layer is effective at increasing the ratio of TBPe to PtNON emission. The drop in EQE results from the TBPe being in close contact with a high concentration of 20% PtNON layer. This close contact can lead to Dexter energy transfer at the interface reducing device performance.

Device 13 incorporates a third TBPe layer between the 10% and 6% PtNON layers. Device 13 has a peak EQE of 16.9% and an EQE at 1000 cd/m^2 of 15.2%. Under constant current test conditions, the device has a Lt_{70} of 46 hours at a starting brightness of 4540 cd/m^2. This device showed the largest improvement in color quality with a peak EL of 466nm and a FWHM of 60nm. The addition of the TBPe layer at the 10%-6% interface

improves the emission color quality of the device. The large difference between the emission color from device 12 to device 13 suggests that the recombination zone has successfully been shifted deep into the emission layer.

Device 14 also has three TBPe layers, the first is inside the 20% PtNON layers, the second between the 20% and 10% PtNON layers, and the third inside the 10% PtNON layer. Device 14 has a peak EQE of 13.5% and an EQE at 1000 cd/m^2 of 12.1%. The large drop in EQE results from the addition of the TBPe layer inside the 20% PtNON layers. The high concentration of PtNON surrounding the TBPe layer leads to a higher rate of triplet-triplet annihilation and non-radiative Dexter energy transfer. In addition, the color quality decreases from device 13, we believe this to be a result of lower TBPe emission rates caused by triplet-triplet annihilation in the layer inside the 20% PtNON layer. This leads to device 14 having similar emission characteristics to device 12 despite having more TBPe.

Table 1: Summary of PtNON and PtNON with TBPe devices, EQE, Brightness, Lifetime, and CIE coordinates are shown.

Device	EQE		Brightness @ 20mA/cm^2	LT_{70}		CIE
	Peak	1,000 cd/m^2		20mA/cm^2	1,000 cd/m^2	
1	12.6%	11.6%	4380 cd/m^2	37.8 h	466 h	(0.17,0.38)
2	17.8%	16.8%	6860 cd/m^2	14.3 h	378 h	(0.19,0.41)
3	17.4%	17.4%	7700 cd/m^2	41.6 h	1337 h	(0.19,0.41)
4	16.3%	16.2%	6360 cd/m^2	32.1 h	745 h	(0.17,0.35)
11	18.0%	17.1%	5700 cd/m^2	39.5 h	761 h	(0.16,0.29)
12	17.6%	16.2%	5200 cd/m^2	43.0 h	709 h	(0.16,0.28)
13	16.9%	15.2%	4540 cd/m^2	46.0 h	602 h	(0.15,0.25)
14	13.5%	12.1%	4110 cd/m^2	67.0 h	741 h	(0.16,0.30)

The stepped EML that was incorporated into the PtNON system successfully shifted the recombination zone away from the EBL serving to improve charge confinement and extend the operational lifetime of the device. As noted previously, the three-layer device exhibited EQE at high brightness that meets that reported EQE from a charge confined structure. This suggests that the three-layer structure has near perfect charge confinement. In addition, the operation stability of the device and power efficiency are improved significantly. Following these results, the color quality of the PtNON system was improved

by using a fluorescent sensitizer that can utilize the high triplet energy excitons harvested by PtNON. The CIE coordinates were successfully shifted from (0.19,0.41) to (0.15,0.25), this is much closer to the coordinates for a blue display color set by the national television standards committee (NTSC) (0.14,0.08). (Note: The NTSC standards are no longer widely used as the displays target performance. As ultra-high definition (UHD) displays are produced, new color spaces are continuously being defined.)

2.3: PtN3N Layered Structure

There are numerous reports regarding the operational stability of Pt complexes in the past 5 years, which have demonstrated performance showing promise but still deemed unsatisfactory.[58,69–72] There are several reasons for the slow progress. Firstly, the display industry tends to use LT_{97} at a high luminance of 1000 cd/m^2, i.e. the operational lifetime at 97% of initial luminance, as an important metric for emitter evaluation to minimize the image sticking effect as well as the differential aging effect on the displays. This is a much more strict requirement than typical LT_{90}-LT_{50} values reported from most literature.[73–80] Secondly, due to the strong competition among commercial material vendors, the majority of reports regarding the OLED operational stability include proprietary host and transporting materials with undisclosed molecular structures. This presents a challenge to academic groups and slows the progress of research.[71,81,82] Thirdly, specific device architecture design might be needed for Pt(II) complexes due to the fact that cyclometalated Pt(II) complexes tend to have deeper HOMO energy levels and less favorable hole trapping capabilities than their Ir analogs, resulting in a higher degree of difficulties in achieving a hole-electron balance inside the emissive layer (EML).[73] To the best of our knowledge, the most stable Pt complex presented in literature is platinum(II) [9-(4-tert-butylpyridin-2-yl-

κN)-2'-(4-phenylpyridin-2-yl-κN) −2,9'-bi-9H- carbazole-1,1'-diyl-κC1,κC1'] (PtN3N-ptb), which exhibited an estimated LT97 of 638 h at an initial luminance of 1000 cd/m^2.[58,70–72] However, its device external quantum efficiency (EQE) at 1000 cd/m^2 is too low (7.8%) to match the values of typical efficient phosphorescent OLEDs. Additionally the LT_{97} lifetime (638 h) is also unsatisfactory to meet the commercialization standard. In this chapter, we will report an efficient cyclometalated Pt(II) complex with superior efficiency and operational stability, demonstrating the satisfactory performance to break the last technical barrier impeding the commercialization process of Pt complexes.

As an analog of the previously reported PtN3N-ptb,[58] PtN3N employs a tetradentate cyclometalating ligand including a 2-pyridylcarbazole as a lumiphore bonded to 9-pyridylcarbazole, the chemical structure of which is illustrated in the inset of Figure 34. The room-temperature absorption and emission spectra of PtN3N and PtN3N-ptb in the solution of CH_2Cl_2 are shown in Figure 34. Similar to PtN3N-ptb, three characteristic types of resolved absorption bands of PtN3N are observed. The high energy, very strong absorption bands (250-400 nm, ε = 1.5-5.5×10^4 cm^{-1} M^{-1}) are attributed to allowed $^1(\pi-\pi^*)$ transitions localized on the cyclometalating ligand. The strong absorbtion bands located at longer wavelengths (435−550 nm, ε = 4787 cm^{-1} M^{-1}) can be assigned to metal-to-ligand-charge-transfer (MLCT) transitions. The weaker, lowest energy broad absorption band between (550−590 nm, ε = 87 cm^{-1} M^{-1}) can be identified as the triplet absorption (T1) on the basis of the small energy difference between absorption and emission at room temperature.[69,83,84] Compared to PtN3N-ptb, the T_1 absorption of PtN3N has a slightly lower extinction coefficient, which is partially overlapping with its own emission spectrum, indicating a more localized excited state.

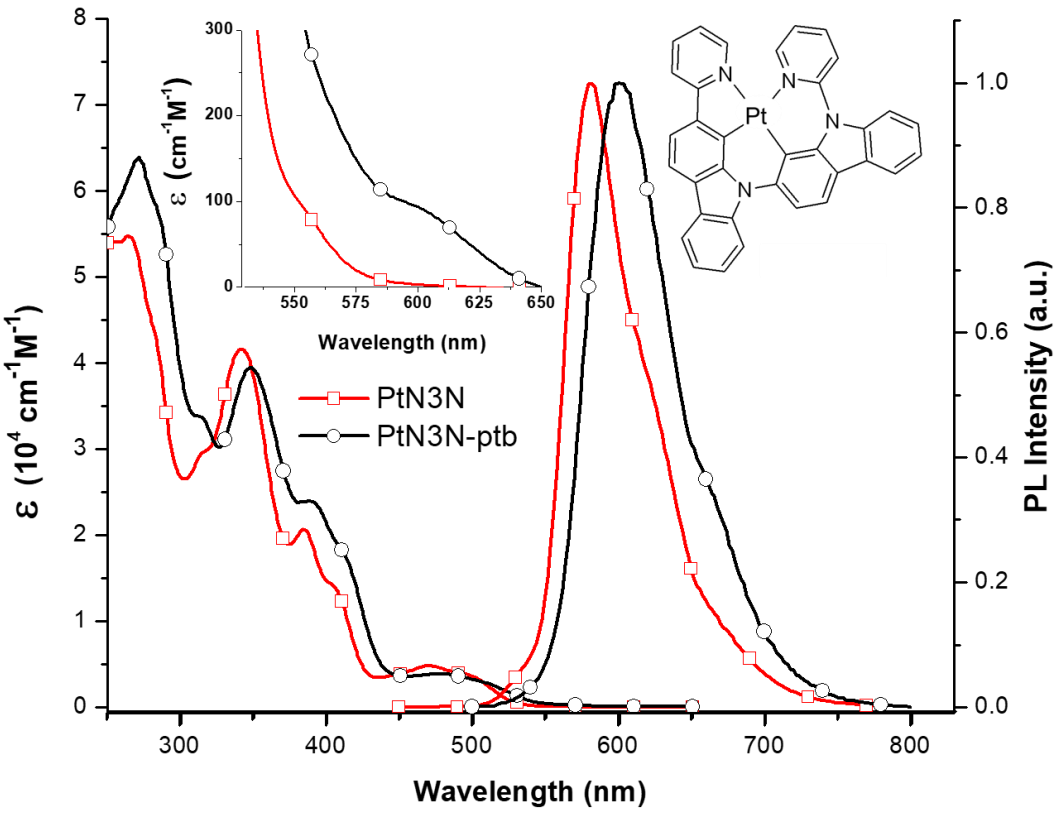

Figure 34: Absorption and emission spectra of PtN3N and its analog PtN3N-ptb.

This is also consistent with the fact that PtN3N exhibits more pronounced vibrionic features in its 77K emission spectrum. PtN3N shows an emission spectrum at room temperature with a dominant emission peak at 582 nm, a small blue shift compared to that of PtN3N-ptb with a peak at 602 nm (Figure 35). The photoluminescent quantum yield (PLQY) of PtN3N in a solution of CH_2Cl_2 is 0.64±0.10 at room temperature, which is much higher than PtN3N-ptb (0.34±0.10), indicating that PtN3N might be more suitable as phosphorescent emitter for OLED applications. The transient lifetimes for PtN3N are 9.0 μs in 2-MeTHF at 77 K and 7.3 μs in CH_2Cl_2 at room temperature. Such a short transient lifetime variation of

PtN3N at different temperatures is also a strong indication of high PLQY value for PtN3N if a near-unity PLQY is assumed for typical phosphorescent emitters at 77 K.[85]

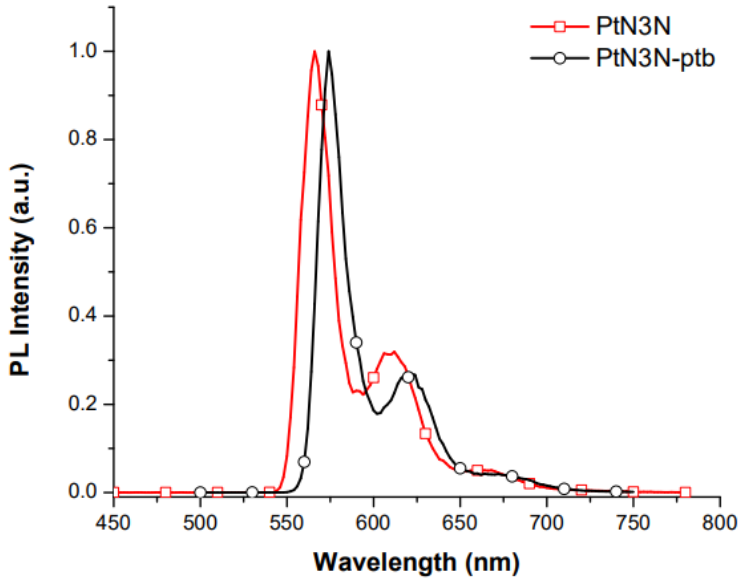

Figure 35: PL spectra at 77K in a solution of 2me-THF.

To evaluate the electroluminescent properties and operational stability of PtN3N, we fabricated and tested two devices in a known stable structures of ITO/HATCN(10 nm)/NPD(40 nm)/TrisPCz(10 nm or 0 nm)/10% PtN3N:CBP/BAlq (10 nm)/BPyTP(40 nm)/LiF(1 nm)/Al(100 nm), where CBP is 4,4'-bis(N-carbazolyl) biphenyl and BAlq is Bis(8-hydroxy-2-methylquinoline)-(4-phenylphenoxy)aluminum. The only variation between the two device structures is Tris-PCz is added to Device 2 as an electron blocking layer. The EL spectra, forward viewing EQE vs luminance curve and relative luminance vs operational lifetime characteristics of both devices are plotted in Figure 36a-c.

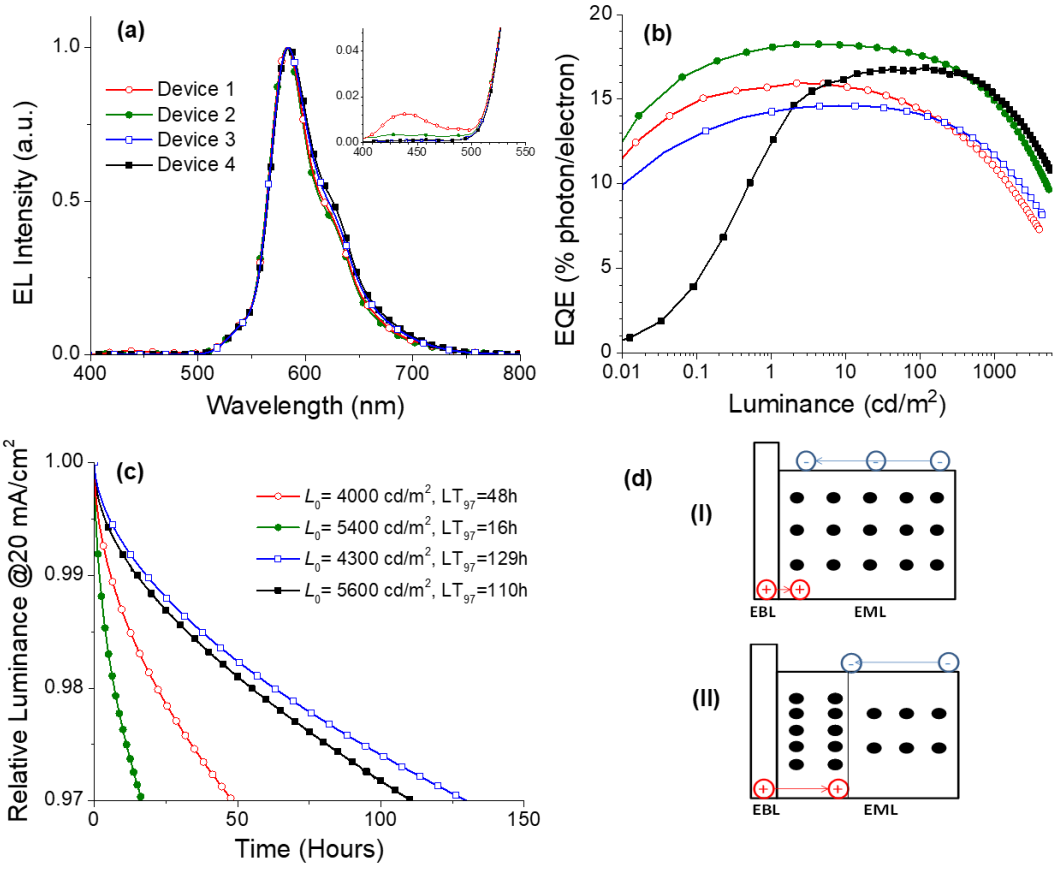

Figure 36: a) EL spectra with the inset showing nonexclusive emission from 400-450nm, b) EQE vs Luminance, c) device operational time at 20ma/cm² d) schematic of single and split EML used in device 2 and 4.

Both devices showed orange-red emission spectra peaking at 584 nm, which is slightly broader than the PL spectrum of PtN3N in a dilute solution due to a higher concentration of emitters in the solid thin films. In Device 1, the EL spectrum includes a small portion of detected emission in the range between 410 and 480 nm (Figure 36a inset), which was previously observed in similar devices employing PtON11-Me and PtN3N-ptb as emissive dopants.[58,86] The origin of blue luminescence in Device 1 is likely attributed to the emission of NPD at the interface between the EML and the hole transporting layer (HTL), indicating some degrees of electron or exciton transfer from the emissive layer to the NPD layer.

Device 1 demonstrated a maximum forward viewing EQE of 15.9%, and maintained an EQE of 10.9% at the brightness of 1000 cd/m^2 while Device 2 showed an improvement in peak EQE of 18.2%, and an EQE of 14.9% at 1000 cd/m^2 due to the incorporation of Tris-PCz layer as an additional EBL in Device 2. It is worthy of mentioning that Device 2 was more efficient than PtN3N-ptb based device in the identical settings, which exhibited a peak EQE of 10.8%, and an EQE of 7.8% at 1000 cd/m^2. Such a significant improvement in the device efficiency is consistent with the improvement in the PLQY values between PtN3N-ptb and PtN3N, making PtN3N more suitable as a phosphorescent emitter for OLED applications.

Figure 36c shows the normalized intensity versus time for both OLEDs corresponding to initial brightness's of L_0 = 4000, 5400 cd/m^2 for Device 1-2 respectively at a constant driving current of 20 mA/cm^2. LT_{97} lifetimes were chosen as metrics to evaluate the operational stability of PtN3N in various device settings where LT_{97} of Device 1 was 48 h and LT_{97} of Device 2 was 16 h. Lifetime at different luminance values can be estimated using the stretched exponential from chapter 2.1 of $LT(L_1) = LT(L_0)(L_0/L_1)^n$. For comparison, LT_{97} at 1,000 cd/m_2 was approximated and presented in Table 2 using a moderate n value of 1.7, following previous literature.[58] The estimated LT_{97} at 1,000 cd/m^2 of Device 1 was around 507 h, which is also more than that of Device 2 (281 h), but lower than the best reported PtN3N-ptb devices in the similar structure (638 h), which can be attributed to the intrinsic electrochemical instability of PtN3N or fast degradation process induced by other factors.

Table 2: Summary of PtN3N device performance metrics.

Device	EML conc.% (thickness nm)	Peak EQE (%)	EQE (%) @ 1,000 cd/m^2	L_0	LT_{97} 20 mA/cm^2	LT_{97} 1,000 cd/m^2
1	10 (25)	15.9	11.0	4,000	48	507
2	10 (25)	18.2	14.9	5,400	16	281
3	20 (10)/6(20)	14.6	11.7	4,300	129	1640
4	20 (10)/6(20)	16.9	15.3	5,600	110	2054

It is reasonable to assume that the addition of the Tris-PCz layer as an EBL eliminated the NPD emission and confined the exciton formation zone inside the emissive layer. This can also create a charge build-up at the EML-EBL interface, leading to faster degradation of the device. To circumvent such issues, it will be ideal to reduce the charge buildup at the EML-EBL interface and shift the exciton formation zone deep into the emissive layer. As previously demonstrating this can be accomplished by constructing a layered EML with differential dopant concentrations intended for balanced charge transport as illustrated in Figure 36d. The resulting change to the EML will potentially reduce the device efficiency roll-off and slow down emissive material degradation process, resulting in an increase of device operational lifetime.[45,63,80] Devices 3 and 4 are constructed following such a concept by replacing the original single EML of 10% PtN3N:CBP (25nm) in devices 1 and 2 with the bi-layer EML of 20% PtN3N:CBP (10nm)/6% PtN3N:CBP (20nm). Both devices produced a slightly broader EL spectrum while eliminating the non-exclusive NPD emission. The broadened EL spectra results from the use of a higher dopant concentration in the bi-layer EML (up to 20%), and the elimination of NPD emission in device 3 and 4 suggests that the exciton formation zone is shifted away from the EML-EBL interface.

Moreover, device 3 exhibited a maximum forward viewing EQE of 14.6%, and an EQE of 11.7% at 1,000 cd/m^2 while device 4 showed a maximum forward viewing EQE peaking at 16.9%, and maintained a high EQE of 15.3% at 1,000 cd/m^2 due to reduced efficiency roll-off. More importantly, the resulting change in devices 3 and 4 led to a significant improvement in the device operational stability. We have recorded a LT_{97} of 129 h with a L_0 of 4,300 cd/m^2 and a LT_{97} of 110 h with a L_0 of 5,600 cd/m^2 respectively for devices 3 and 4, which yielded an estimated LT_{97} of 1540 h and 2057 h respectively at a luminance of 1,000 cd/m^2. To the best of our knowledge, these are the most stable OLEDs within literature using known and publicly accessible functional materials, providing a valuable benchmark for the OLED research community.

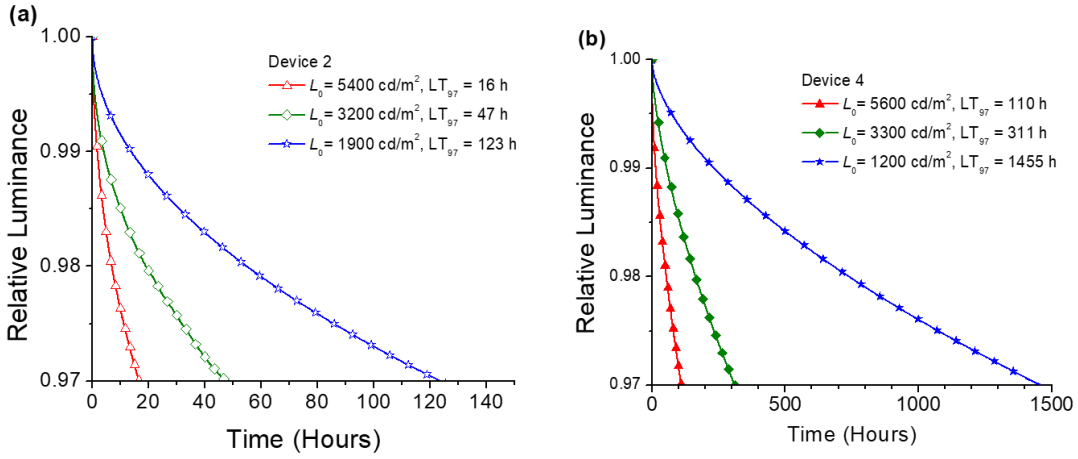

Figure 37: Variable current density lifetime a) Device 2 employing a single EML, b) Device 4 employing a split EML.

Estimating the device lifetime in an accelerated device testing condition is a quick and cost-effective way to screen materials. However, such a process might not be accurate if the escalation factor n in the stretched exponential formula is not chosen correctly. Additionally, n has been shown to be strongly dependent on the choice of emissive materials

and various device operational mechanisms.[49,63,87] In order to validate the superior operational stability of PtN3N in the device settings, we have run device 2 and device 4 in various constant current densities ranging from 5 to 20 mA/cm^2. We have recorded a LT_{97} of 16h at 5,400 cd/m^2, 47 h at 3,200 cd/m^2 and 123 h at 1,900 cd/m^2 for device 2, and a LT_{97} of 110 h at 5,600 cd/m^2, a LT_{97} of 311 h at 3,300 cd/m^2 and a LT_{97} of 1455h at 1,200 cd/m^2 for device 4. The plots of LT_{97} lifetime vs. initial luminance L_0 of device 2 and device 4 are shown in Figure 38 and the n values were obtained by fit LT_{97} vs L_0 in log-log scale using $(LT_{97})(L_0)^n$ = constant, resulting in n value of 1.65 and 1.95 for Device 2 and Device 4 respectively. By extrapolating the fitting curve, we have obtained the estimated LT_{97} of 439 h and 2036 h for device 2 and device 4 respectively at 1,000 cd/m^2. This demonstrates that the layered EML structures have a significant impact on the degradation mechanism of the PtN3N devices.

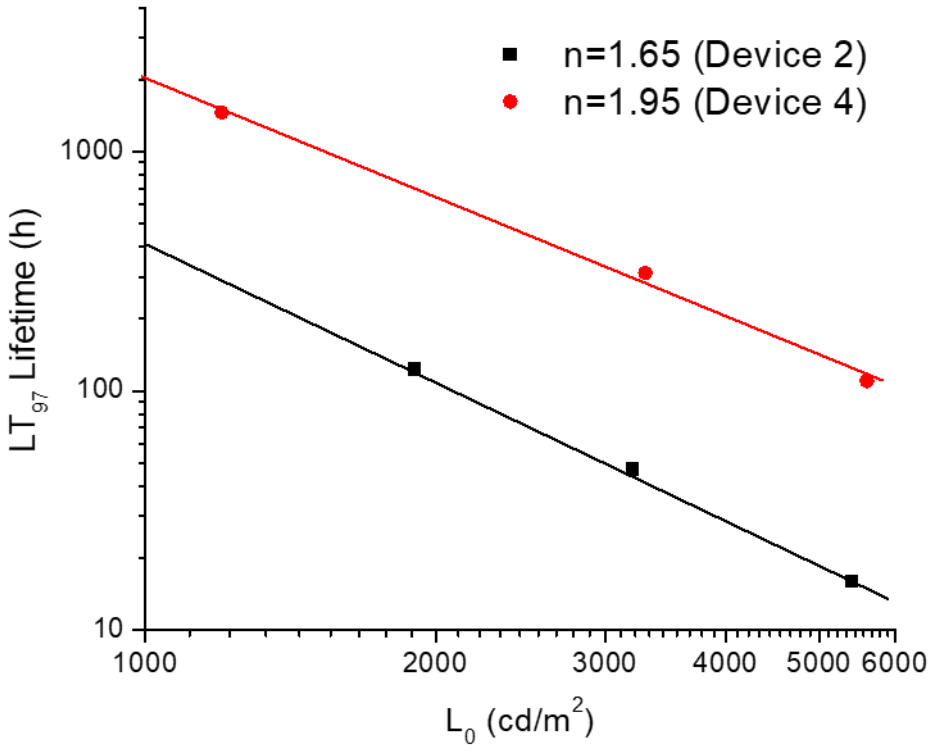

Figure 38: Escalation factor of single and split EML.

In this section, we have demonstrated that cyclometalated Pt(II) complex can be efficient in the device settings with superior operational stability. In a charge balanced device structure, one PtN3N device has demonstrated an estimated LT_{97} of 2057 h at an initial luminance of 1,000 cd/m^2 while maintaining an EQE of 15.3% at such high brightness. The utilization of the state-of-the-art charge transporting and blocking materials will further improve the performance of PtN3N in the device settings, which will make Pt complexes more appealing as phosphorescent emitters in the display industry.

2.4: Conclusion

In this chapter, a novel and practical technique for improving charge balance and the exciton formation dynamics in an OLED have been demonstrated. Implementing a layered EML structure is shown to alter the charge injection barriers and charge transport characteristics of a stable OLED device. In a stable PtNON device this improved the EQE at 1,000 cd/m^2 from 11.6% to 17.4% while increasing the estimated LT_{70} from 466 hours to over 1,300 hours from a starting brightness of 1,000 cd/m^2. This stable PtNON device was further improved through the design of a fluorescent sensitized device that achieved an EQE at 1,000 cd/m^2 of 15.2% with an LT_{70} of 46 hours at a constant current density of 20 mA/cm^2. This device demonstrated a significant blue shift in EL emission with CIE coordinated improving from (0.17, 0.38) to (0.15, 0.25). Furthermore, this layered EML technique was successfully applied to a red OLED device improving its EQE from 14.9% to 15.3% at 1,000 cd/m^2 while and its estimated LT_{97} from a starting brightens of 1,000 cd/m^2 increased from 281 hours to 2054 hours. The layered EML structure has been shown to have a significant impact on device performance without the need for implementing additional materials or overly complex structures.

3: Metal-Assisted Delayed Fluorescence

The development of stable blue phosphorescent OLED devices remains a primary hurdle to the widespread implementation of OLED technology. As the emission energy increases, it is widely speculated that the formation of multiply excited triplet excitons tends to directly facilitate the dissociation of σ-bonds. This has been demonstrated for Si-Si in polysilane materials and other similar material systems, indicating a greater challenge for developing stable deep blue triplet emitters.[88] A logical solution to this issue, from an energy standpoint, is to develop efficient blue emitters with triplet energy in the "green" or "red" region that can also harvest all of "blue" singlet excitons. While this describes many conventional blue fluorescent emitters that only harvest singlet excitons, it limits device IQE to 25% and wastes triplet excitons. Conversely, phosphorescent emitters with "green" triplet energies can attain 100% IQE but are incapable of using the higher energy singlet excitons to emit blue. Thus, an innovative molecular design will be needed to achieve such a goal.

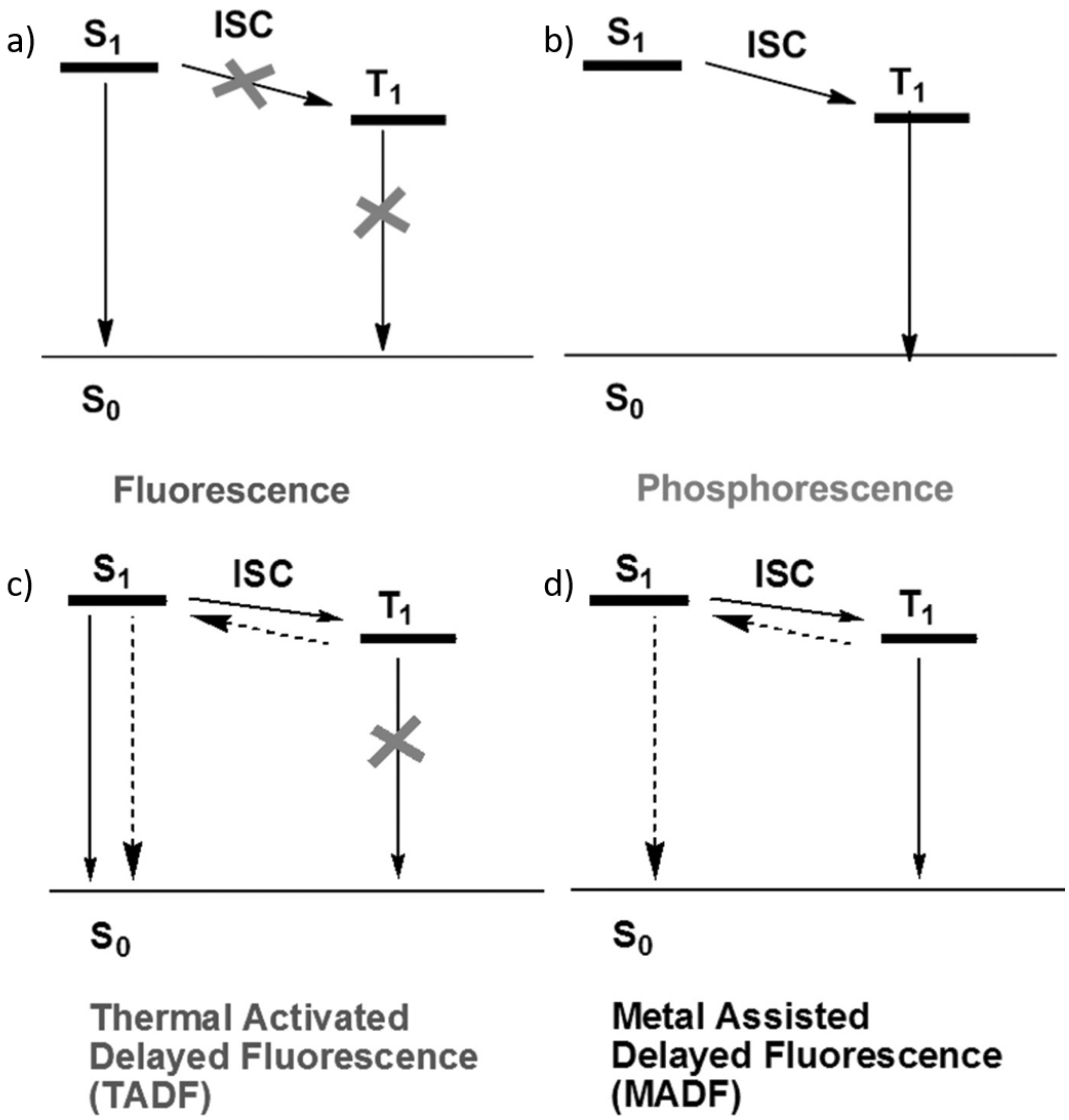

Figure 39: Summary of singlet and triplet transitions associated with a) Fluorescence, b) Phosphorescence, c) Thermal Activated Delayed Fluorescence and d) Metal assisted Delayed Fluorescence.

Investigations on the detailed mechanism of harvesting electrogenerated excitons inside of organic electroluminescent devices have been well documented in the past two decades. [89–91] For most organic fluorescent emitters, fluorescence (Figure 39a) is the only pathway to radiative decay, where phosphorescence is severely suppressed due to its symmetry forbidden character. On the other hand, cyclometalated Ir and Pt complexes have

fast intersystem crossing and rapid phosphorescence processes (Figure 39b) due to strong spin-orbit coupling, enabling them to harvest both electrogenerated singlet and triplet excitons, resulting in a theoretical 100% electron to photon conversion efficiency.[28,92,93] Recent studies on carbazolyl-dicyanobenzene derivatives and copper(I) based metal complexes, characterized as thermal activated delayed fluorescent (TADF) emitters, have also demonstrated high emission quantum yield at the room temperature and can be utilized in the device settings to harvest both singlet and triplet excitons.[94–96] As illustrated in Figure 39c, when the energy levels of the lowest triplet excited state (T_1) and the lowest singlet excited state (S_1) are similar in energy, the triplet excitons can decay radiatively through the combination of reverse intersystem crossing ($T_1 \rightarrow S_1$) and a delayed fluoresent ($S_1 \rightarrow S_0$) processes. This approach has the benefit of being able to achieve a higher energy emission for a given triplet energy. This enables the incorporation of these emitters into structures using known stable host and transport materials unlike many conventional phosphorescent deep-blue Ir or Pt emitters.[97] Nevertheless, the endothermic nature of this process will result in a portion of the triplet excitons experiencing "cold" nonradiative decay. This is caused by insufficient thermal energy to overcome the ($T_1 \rightarrow S_1$) energy barrier leaving excitons in the triplet state to decay nonradiatively due to the absence of an efficient phosphorescent emission pathway. This restricts the usefulness of TADF emitters. High efficiencies can only be achieved for very small S_1–T_1 energy splitting leading to high triplet energies still being required for deep blue fluorescent emission.[98,99] In this chapter, a new mechanism of utilizing electrogenerated excitons, denoted metal-assisted delayed fluorescence (MADF), where a heavy metal ion will be incorporated into the complex system to ensure both efficient phosphorescence and delayed fluorescent processes, will be presented. As shown in Figure 39d, when the energy levels of the T_1 state and the S_1 state are

reasonably close, the two radiative decay process, i.e., phosphorescence ($T_1 \rightarrow S_0$) and thermally activated delayed fluorescence ($S_1 \rightarrow S_0$) can occur simultaneously. Due to its efficient triplet emission process, MADF emitters can harvest all singlet and triplet excitons regardless of larger energy difference between the T_1 and S_1 states compared to TADF. In this chapter, a study of three primary MADF emitters and their analogs, PdN3N, PdN1N-dm, and PdON1a, is presented.

3.1: PdN3N: Green MADF

The absorption spectra for PdN3N as well as the N3N ligand is shown in Figure 40. Both the complex and ligand exhibit very strong absorption bands below 400 nm ($\varepsilon > 10^4$ cm^{-1}) assigned to $^1\pi$–π^* transitions, localized on the cyclometalating ligands. The shift to lower energy of these transitions in the complex is attributed to the planar molecular geometry of the ligand when covalently bonded to the Pd ion as well as the anionic nature of the ligand in the complex. The intense band in the 400–500 nm range for the complex ($\varepsilon \approx 10^3$–10^4 cm^{-1} M^{-1}) is redshifted relative to any absorption from the ligand and is assigned to singlet metal to ligand charge transfer (^{1}MLCT) transitions.

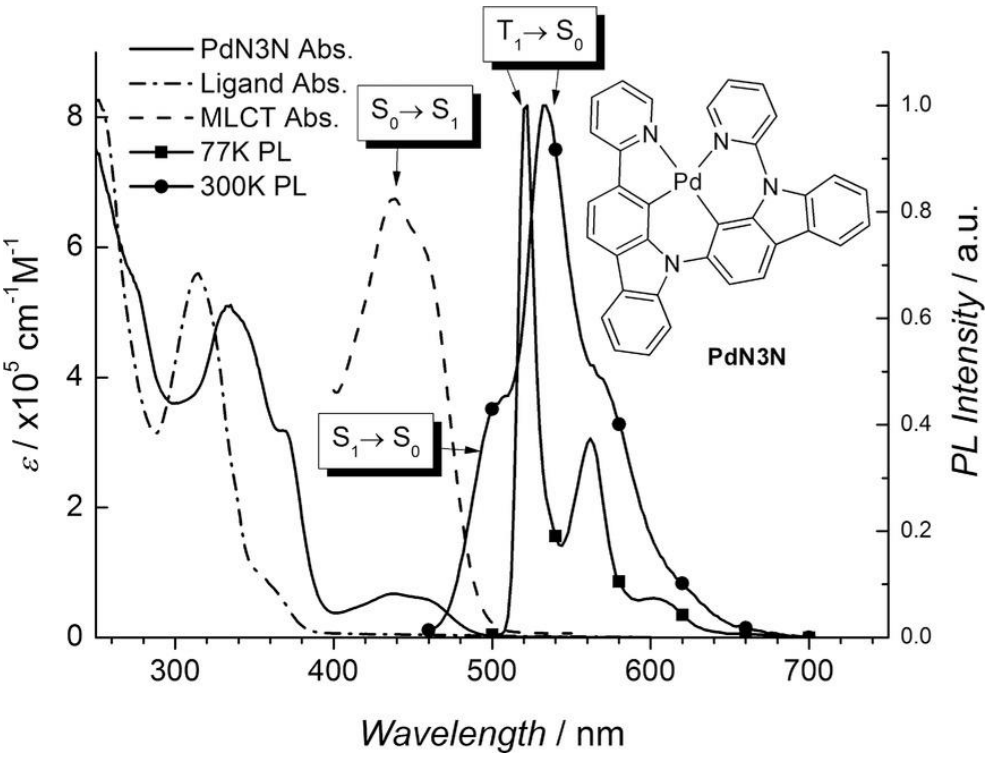

Figure 40: Absorption of PdN3N and N3N ligand with enhanced MLCT absorption peak, PL of PdN3N at 300K and 77K.

The 77 K photoluminescence (PL) emission spectrum shows a narrow primary emission peak at 522 nm with small vibronic peaks characteristic of many phosphorescent emitters. The emission at 522 nm is attributed to a $T_1 \rightarrow S_0$ transition on the basis of the large Stokes shift from the absorption cut-off. This is a higher wavelength than many existing phenyl-pyridine complexes due to its extended conjugation through the carbazole units.[78,100] At room temperature (300 K) the dominant emission peak is slightly redshifted to 534 nm and significantly broadened, typically seen at elevated temperatures. Unlike previously reported heavy metal phosphorescent complexes, an emission side-band at a shorter wavelength range (between 480 and 510 nm) appears at the elevated temperatures indicating the presence of a thermally activated emission process. When measured at

detector wavelengths of 530 and 485 nm, respectively, the identical excitation spectra and comparable room temperature radiative decay lifetimes of 142 and 145 μs indicate both emission species share the same origin.

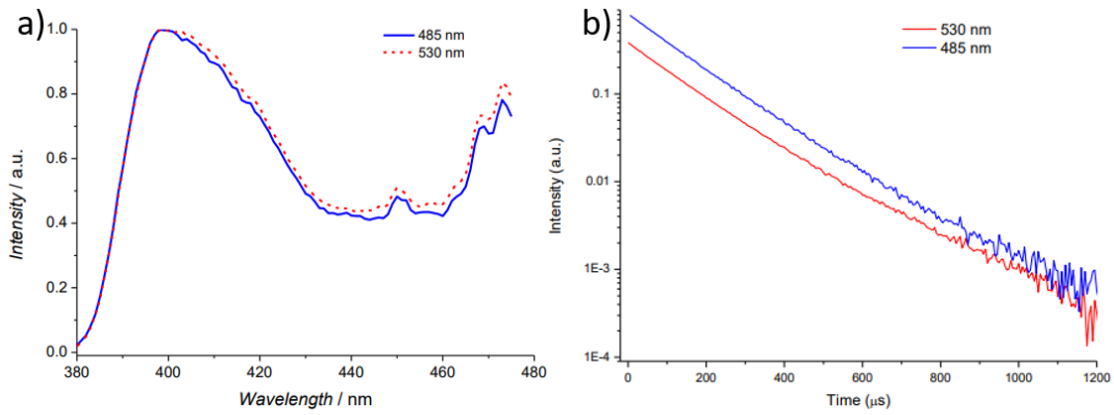

Figure 41: a) excitation spectra measured at 485nm and 530nm corresponding to the thermally activated peak and the primary phosphorescent peak, b) Transient lifetime of PdN3N measured at 485nm and 530nm.

These assignments are similar to those recently reported for Cu(I) complexes exhibiting both phosphorescent and TADF emission.[101,102] This indicates the existence of both phosphorescence and thermally activated delayed fluorescence within the single emitter.

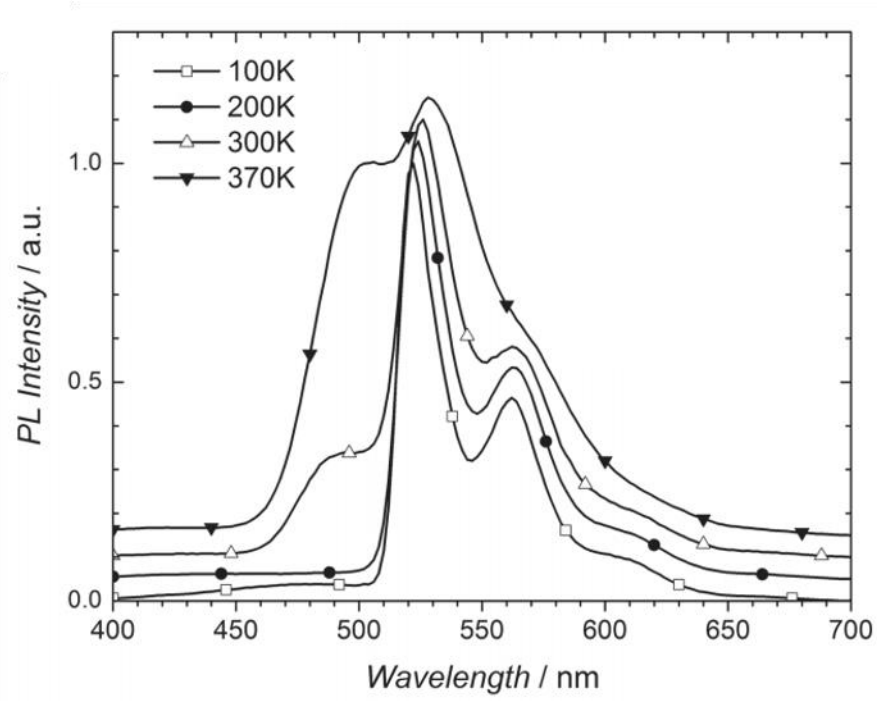

Figure 42: Variable temperature PL measurements offset in the Y direction for clarity.

To explore the origins and characteristics of the MADF emission, PL spectra as a function of temperature was measured for PdN3N, shown in Figure 42. The designed molecules can be described as containing two parts: a C^N cyclometalating ligand containing the pyridyl-carbazole portion of the molecules and the donor–acceptor (D–A) portion of carbazole-carbazolyl-pyridine. The triplet state consists mostly of the lower energy C^N portion of the molecules which is localized on the pyridyl-carbazole and as such has a phosphorescent peak at of 522nm at 77K.[85] At higher temperatures, a thermally activated delayed fluorescence peak appears. The carbazolyl-pyridine ligand of PdN3N is correlated to the delayed fluorescent emission peak resulting from comparison to PdN3N's analog.[32] The absorption emission overlap of PdN3N at room temperature of 2.83eV corresponds well to the singlet energy estimated from CV with a reduction peak at −2.39 eV versus Fc/Fc^+, and

an oxidation potential of 0.40 eV, shown in Figure 43a. This can be attributed to the charge transfer character of the singlet state and thus related to the HOMO and LUMO which are primarily located on this D–A region.[86]

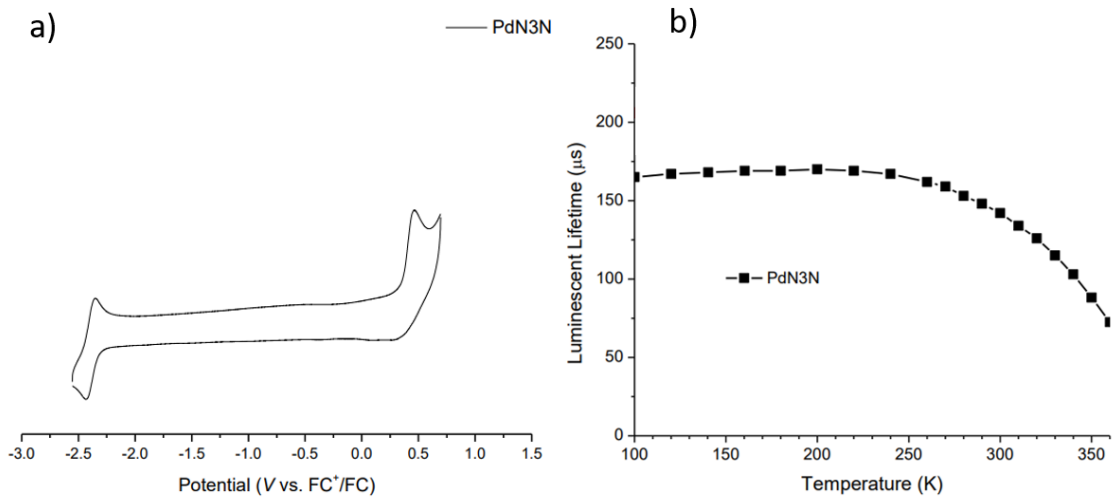

Figure 43: a) Cyclic Voltammetry of PdN3N vs Fc/Fc^+ b) transient lifetime Vs temperature of PdN3N.

Additionally, the photoluminescent quantum yield was high at 0.72 ± 0.10 at room temperature indicating that this emitter would both be a good candidate for efficient OLED devices. It should be noted that the luminescent lifetime of the doped film of PdN3N steadily decrease with increasing temperature (Figure 43b) which provides further indication of the TADF pathway occurring in this material.[103]

To explore the device performance of this novel MADF emitter, OLED devices were fabricated on glass substrates pre-coated with a patterned layer of indium tin oxide (ITO) to serve as the transparent anode for the structure ITO/HATCN(10 nm)/ NPD(30nm)/ TAPC(10 nm)/ 6% dopant: 26mCPy (25 nm)/ DPPS(10 nm)/ BmPyPB(40

nm)/ LiF/ Al, this architecture will be referred to as structure one.[104,105] The EQE is shown in Figure 44 with the electroluminescent spectrum inset in the figure. The EQE of PdN3N peaked at 20.9%, and is comparable to many of the Ir and Pt analogs in a similar device setting.[106] One apparent drawback to devices employing these complexes is the large efficiency roll-off at higher luminance dropping to 14.3% at 100 cd/m^2. This is commonly attributed to a combination of poor charge balance due to the poor electron transporting properties of DPPS and the long phosphorescent lifetime of 142μs. This issue can be addressed through improved charge balance or by improving the spontaneous radiative decay rate, previously demonstrated by employing more advanced structures such as plasmonic nanostructures or microcavities.[106–108]

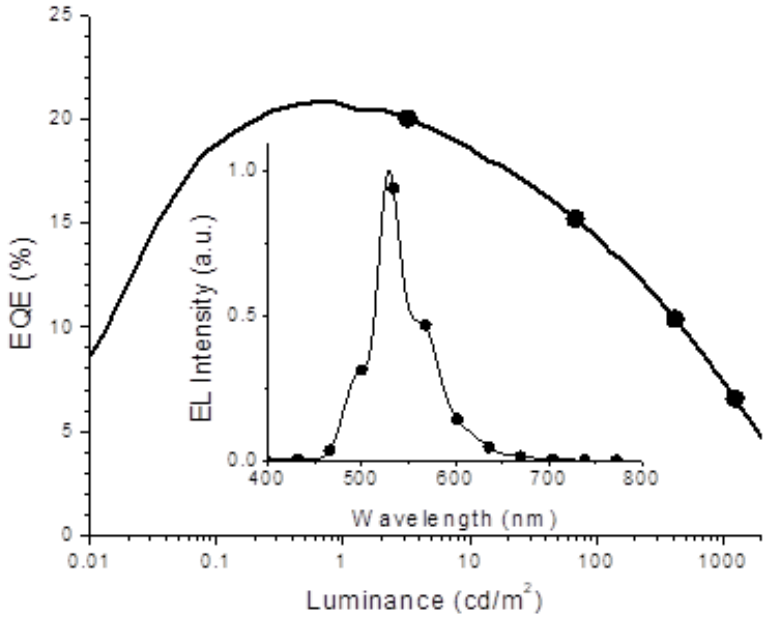

Figure 44: EQE versus Luminance with the corresponding EL spectra at 1 mA/cm2 inset for devices of PdN3N in the structure: ITO/ HATCN/ NPD/ TAPC/ 6% PdN3N:26mCPy/ DPPS/ BmPyPB/ LiF/ Al.

The electroluminescent characteristics show both fluorescent and phosphorescent emission in the devices. PdN3N devices showed a delayed fluorescence peak of

approximately 30% of the phosphorescence peak height but the color was still dominated by the primary green phosphorescent emission with CIE (0.30, 0.61). The high emission efficiency despite the moderate ($T_1 \rightarrow S_1$) splitting, highlights the benefits of MADF emitters over their organic TADF counterparts. Excitons that would otherwise be unable to overcome the ($T_1 \rightarrow S_1$) energy barrier can still emit through the efficient phosphorescent radiative pathway. Furthermore, alterations to the molecular structure can be used to adjust the relative height of the delayed fluorescence peak and shift the phosphorescent emission profile leading to even more ideal spectra.

In order to further explore the potential application of this Pd based MADF complex as stable emitter, three devices were evaluated employing a layered EML in a stable structure of is ITO/HATCN (10 nm)/NPD (40nm)/Tris-PCz (10nm)/EML (30nm)/BAlq (10nm)/BPyTP (40nm)/LiF/Al. Where the EML for the three devices are 6% PdN3N:CBP (30nm) for device 1, 10% PdN3N:CBP (10nm)/ 6% PdN3N:CBP (20nm) for device 2, and 20% PdN3N:CBP (10nm)/ 10% PdN3N:CBP (10nm)/ 6% PdN3N:CBP (10nm). The device performances of these structures are crucial to determining the viability of MADF complexes as a potential solution to high-energy stable emitters.

The EL performance of the layered PdN3N devices is shown in Figure 45. As the doping concentration near the EBL interface is increased, the turn-on voltage and the voltage at 20 mA/cm^2 is reduced. This results from improved hole injection directly to the PdN3N compared to CBP. All 3 devices have a peak EL of 538 nm with a MADF peak between 500 and 520nm at 50% the intensity of the phosphorescent peak. The change in EML doping concentration has a negligible impact on EL emission. Furthermore, all three devices show high peak EQE's of 22%. Unfortunately, the long transient lifetime of PtN3N leads to significant roll-off in the 6% PtN3N device with an EQE at 1,000 cd/m^2 of 10%.

The layered structures serve to slightly reduce the roll-off by spreading the exciton formation zone allowing device 3 to demonstrates an EQE at 1,000 cd/m^2 of 13.7%. Finally, all three devices show promising stability at 20mA/cm^2 with LT_{95} values between 25 and 33 hours. This translates to a PdN3N device having an estimated LT_{95} of 350 hours from a brightness of 1,000 cd/m^2. This demonstrates that MADF emitters have the potential to be stable and efficient alternatives to both TADF and phosphorescent emitters.

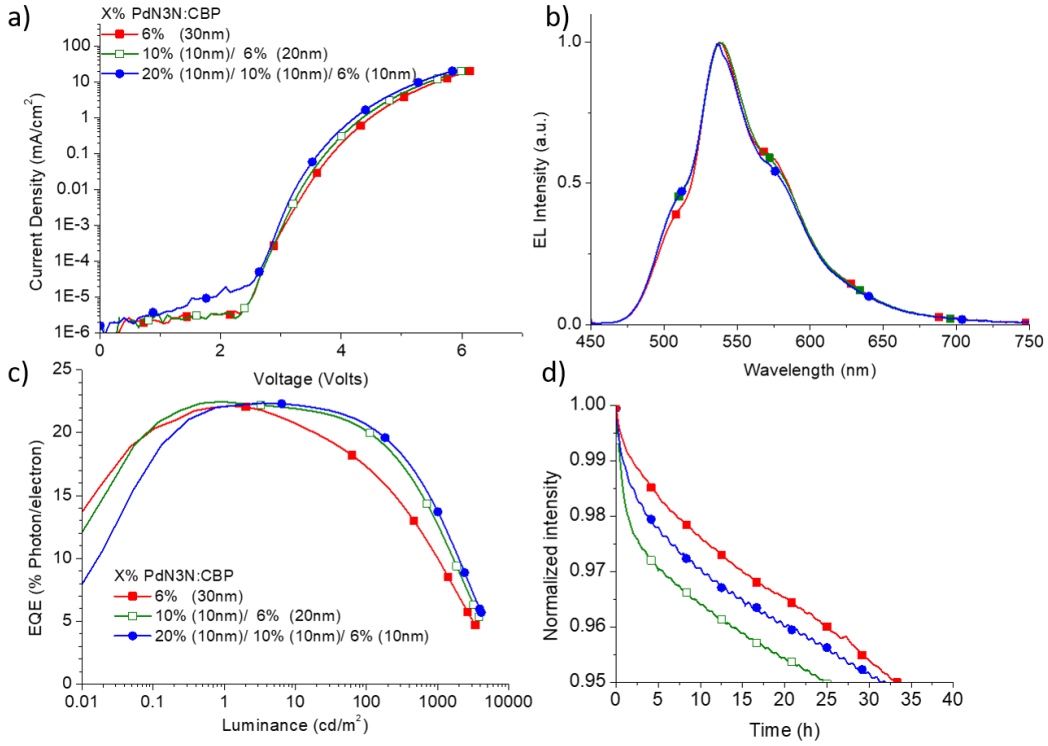

Figure 45: a) Current Density vs Voltage, b) EL spectra, c) EQE vs luminance and d) device operational lifetime.

3.2: PdN1N-dm: Blue MADF

Building off the success of PdN3N, new blue-shifted MADF emitters were developed to evaluate how this system behaves at higher energies. In this section, a series of MADF Pd (II) complexes, PdN1N, PdN1N-dm, and PdN6N, were rationally designed through the structural modification of PdN3N to achieve a blue-shifted emission. In general, a blue-shifted emission can be achieved by lowering the HOMO level or raising the LUMO level. It is well known that the LUMO can be increased by replacing pyridine groups with azole groups such as pyrazole, methylimidazole or imidazol-2-ylidene.[109–111] For this section, pyrazolyl-carbazole based PdN1N, PdN1N-dm, and PdN6N were designed as shown in Figure 46.

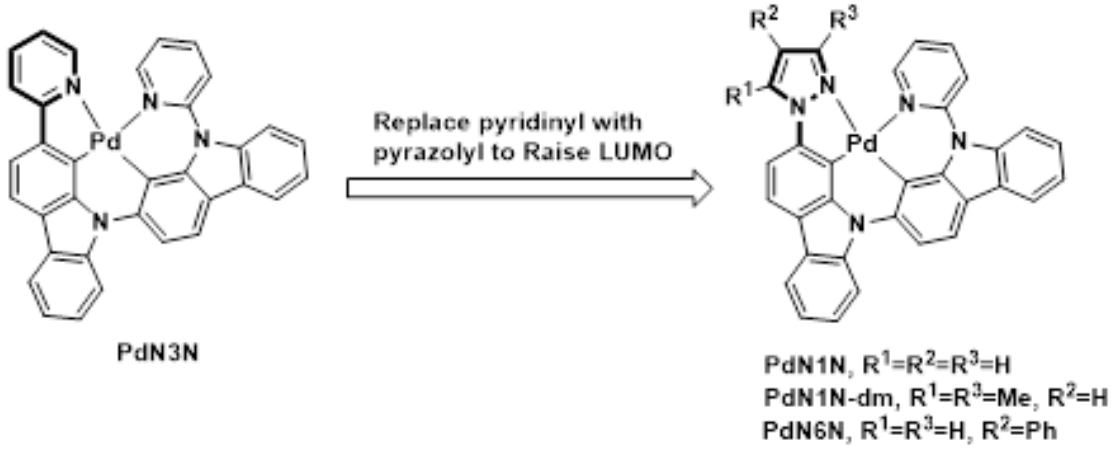

Figure 46: Illustrates the design of blue shifted MADF emitter by replacing the pyridine with a Pyrazolyl to raze the LUMO.

The absorption spectra for PdN1N, PdN1N-dm, and PdN6N measured in a solution of dichloromethane are shown in Figure 47. Three characteristic types of resolved absorption bands are observed in all three of the Pd (II) complexes. All complexes

demonstrated intense absorption bands below 370 nm that can be assigned to allowed $^{1}(\pi\text{-}\pi^{*})$ transitions localized on the pyrazolyl-carbazole cyclometalating ligands (^{1}LC).

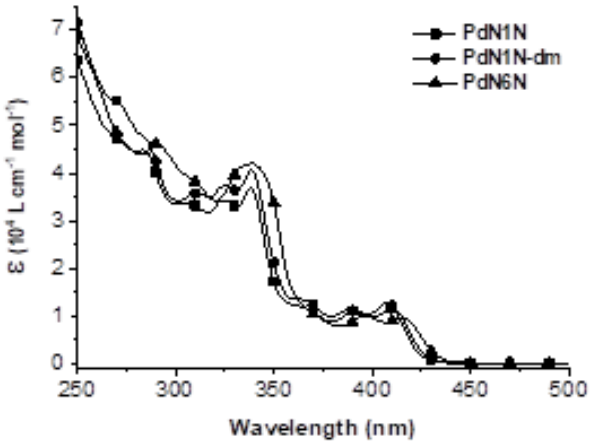

Figure 47: Room temperature absorption spectra of PdN1N, PdN1N-dm, and PdN6N in dichloromethane.

The extinction coefficients (ε) for the $^{1}(\pi\text{-}\pi^{*})$ transitions fall between 12,000 and 70,000 cm^{-1} M^{-1}. The broad bands (ε<13,000 cm^{-1} M^{-1}) located at longer wavelength (370-440 nm) are attributed to MLCT transitions. Additionally, the MLCT absorption bands for these Pd complexes are partially overlapped with their PL emission spectra as confirmed by Figure 48 showing PL onset as low as 420nm.

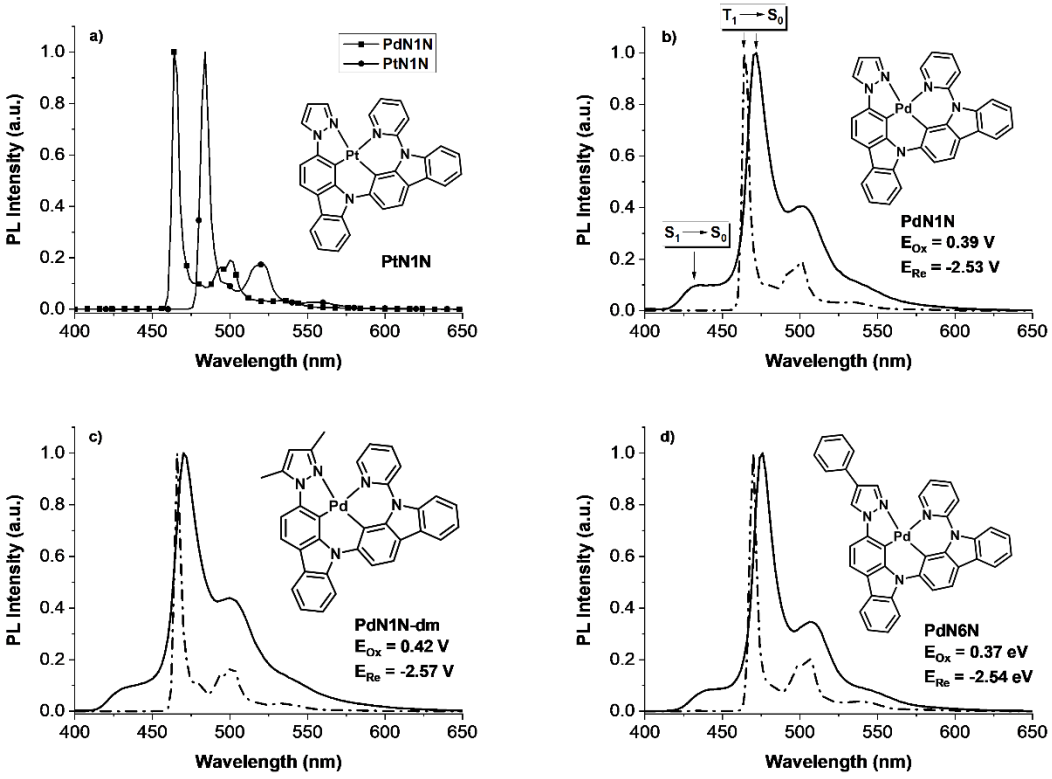

Figure 48: Photoluminescence spectra of PtN1N, PdN1N, PdN1N-dm, and PdN6N at room temperature in dichloromethane (solid lines) and at 77 K in 2-methyltetrahydrofuran (dash-dotted lines). The redox potentials for each complex were also given.

The PL emission spectra of PtN1N, PdN1N, PdN1N-dm and PdN6N measured at 77 K in 2-methyltetrahydrofuran and at 300K in dichloromethane are shown in Figure 48. PtN1N contains a pyrazolyl-carbazole group as the emitting ligand that is bonded to a pyridyl-carbazole group as the ancillary ligand.[69] As shown in Figure 48a, the replacement of platinum with palladium resulted in the blue shift and increase in the triplet energy from 484 nm to 464 nm, according to the 77 K PL spectra of PtN1N and PdN1N. The higher triplet energy of PdN1N over PtN1N is within our expectation because palladium complexes tend to have deeper HOMO energy levels resulting from increased oxidation potential when compared with platinum (II) and iridium (III) complexes.[112] The 77K PL emission spectrum

of PdN1N, given in Figure 48(b), shows a primary emission peak at 464 nm along with small vibronic peaks. At room temperature, the primary emission peak of PdN1N is slightly redshifted to 472 nm, accompanied by broadening of the EL spectra, this is typically seen at elevated temperatures for most emitters. More importantly, room temperature PL spectrum shows a sideband at a shorter wavelength between 410 nm and 450 nm, which is indicative of the presence of a thermally activated emission (MADF, $T_1 \rightarrow S_1 \rightarrow S_0$). This observation is also in good agreement with the previously reported Cu (I) complexes.[101] The photoluminescence quantum yield (PLQY) of PdN1N measured in DCM solution at room temperature is 0.70±0.1, which is very high. However, the vacuum sublimation yield of PdN1N was quite poor due to its low thermal stability. The introduction of two methyl groups (PdN1N-dm) dramatically improved the thermal stability. Furthermore, the PLQY is also been raised to 0.77±0.10 while the PL emission remains largely unchanged at 77 K or room temperature. On the contrary, when a phenyl group is introduced (PdN6N), both decreased thermal stability and a lower PLQY (0.59±0.1) are observed. The high similarity in PL spectra of these Pd (II) complexes is further supported by their electrochemical analysis shown in Figure 49. All the compounds have very similar reduction and oxidation potentials at around −2.54 eV and 0.4 eV versus Fc/Fc^+, respectively.

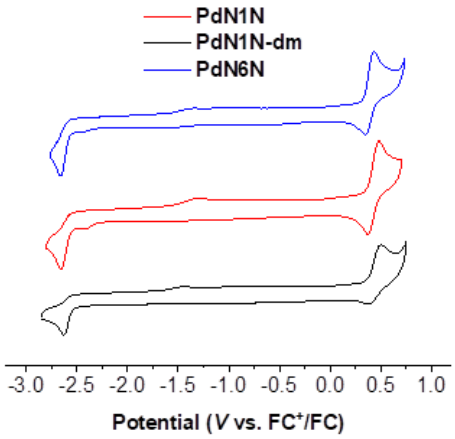

Figure 49: Cyclic voltammograms for PdN1N, PdN1N-dm, and PdN6N.

To investigate the electroluminescence properties of the Pd (II) complexes, two devices employing PdN1N-dm have been fabricated and tested. PdN1N-dm was selected for further study due to its high thermal stability and PLQY compared with its analogs. A known charge confined device structure is adopted: ITO/HATCN (10 nm)/NPD (40nm)/TAPC (10 nm)/10% PdN1N-dm: x % PtN3N-ptb: 26mCPy (25 nm)/DPPS (10 nm)/BmPyPB (40 nm)/LiF (1nm)/Al (100 nm).[32,58] The only difference of the two device structures is 1% PtN3N-ptb was added to Device 2 as a co-dopant. The EL spectra collected at 1 mA/cm^2 and the EQE-luminance curve for both devices is plotted in Figure 50.

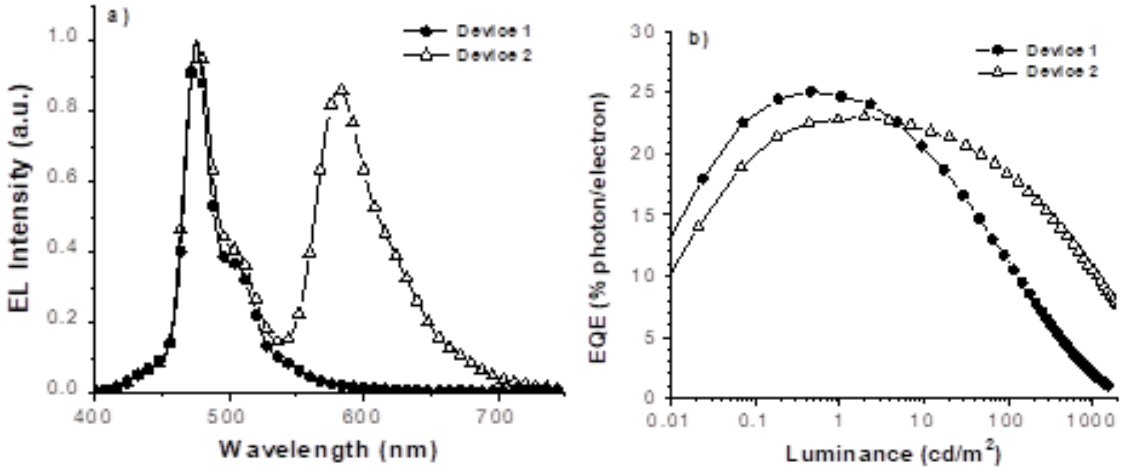

Figure 50: a) EL spectra collected at 1 mA/cm2, b) EQE vs. luminance for Device 1-2 with structure: ITO/HATCN/NPD/TAPC/10% PdN1N-dm: x % PtN3N-ptb: 26mCPy/DPPS/BmPyPB/LiF/Al, wherein x is 0% for Device 1 and 1% for Device 2.

As expected, the EL spectrum of the blue OLED (Device 1) showed a broad MADF band between 410-450 nm ($S_1 \rightarrow S_0$) and a dominant triplet phosphorescent emission peak at 476 nm ($T_1 \rightarrow S_0$). Moreover, like previously reported PdN3N, no aggregate emission was observed for Device 1 even with the dopant concentration of 10%, indicating the nonplanar molecular geometry of PdN1N-dm. In Device 2, a known stable red emitter PtN3N-ptb was co-doped with PdN1N-dm to afford a white OLED.[58] The EL spectrum was shown in Figure 50**a**. The blue OLED (Device 1) demonstrated a notable maximum forward viewing EQE of 25.1 %, and an EQE of 11.1 % at a brightness of 100 cd/m^2. The 25.1% EQE suggests an internal quantum efficiency approaching unity on the basis of 20%–30% outcoupling efficiency.[113] Even with the large EQE roll off at higher luminance, it is worth noting that the maximum EQE of 25.1 % represents the first demonstration of highly efficient blue OLEDs based on MADF Pd (II) complexes. In addition, by co-doping with 1 % PtN3N-ptb the white OLED (Device 2) demonstrated a CIE coordinate of (0.39, 0.37)

and the maximum EQE of 23 % demonstrating MADF emitters potential for use in white OLEDs

To further study on the potential application of PdN1N-dm as an efficient and stable blue emitter, electrochemically unstable TAPC and DPPS were removed from the device.[114] By employing the more stable Tris-PCz as the electron blocking layer and Balq or mCBT as the hole blocking layer, four devices were fabricated with the structure: ITO/HATCN (10nm)/NPD (40 nm) /Tris-PCz (0 or 10 nm)/10% PdN1N-dm: CBP (25nm)/BAlq or mCBT (10 nm)/BPyTP (40 nm)/LiF (1nm)/Al (100 nm).[115] As shown in Figure 51a, the changes to the blocking layer structure had a negligible influence on the EL spectra. Figure 51b illustrates a reduced charge injection barrier in devices 3 and 4 resulting from the use of Balq as a hole blocker. BAlq is better aligned with CBP's LUMO level helping to facilitate electron injection into the EML. Device 3 in Figure 51c employs Balq as the hole blocking layer without Tris-PCz, this device showed the peak EQE of 2.2 %. When Tris-PCz is added as an EBL, the peak EQE of device 4 is slightly improved to 2.7%. These low efficiencies are commonly explained by exciton quenching at the Balq interface. Furthermore, the device efficiency can be improved by replacing the Balq with mCBt, a material with a higher bandgap known to aid in reducing quenching and improving hole blocking. Device 5 and 6 (without and with Tris-PCz) demonstrate a significantly improved peak EQE to 9.3% and 9.8% respectively. However, the overall efficiency of devices 5 and 6 is still significantly lower than devices 1-2 in the known charge confined structure. This results from poor change balance within the device leading to charge buildup and increased TTA, TPQ, and non-radiative quenching of excitons.

The operational lifetimes of these blue OLEDs have also been tested at a constant current density of 20 mA/cm^{-2}. Device 5 demonstrated an operational lifetime LT_{70} of 11.5 h

with an initial luminance (L_0) of 706 cd m^{-2}. This approximately corresponds to a LT_{70} of 319 h at 100 cd m^{-2} using the stretched exponential formula with n=1.7.[49]

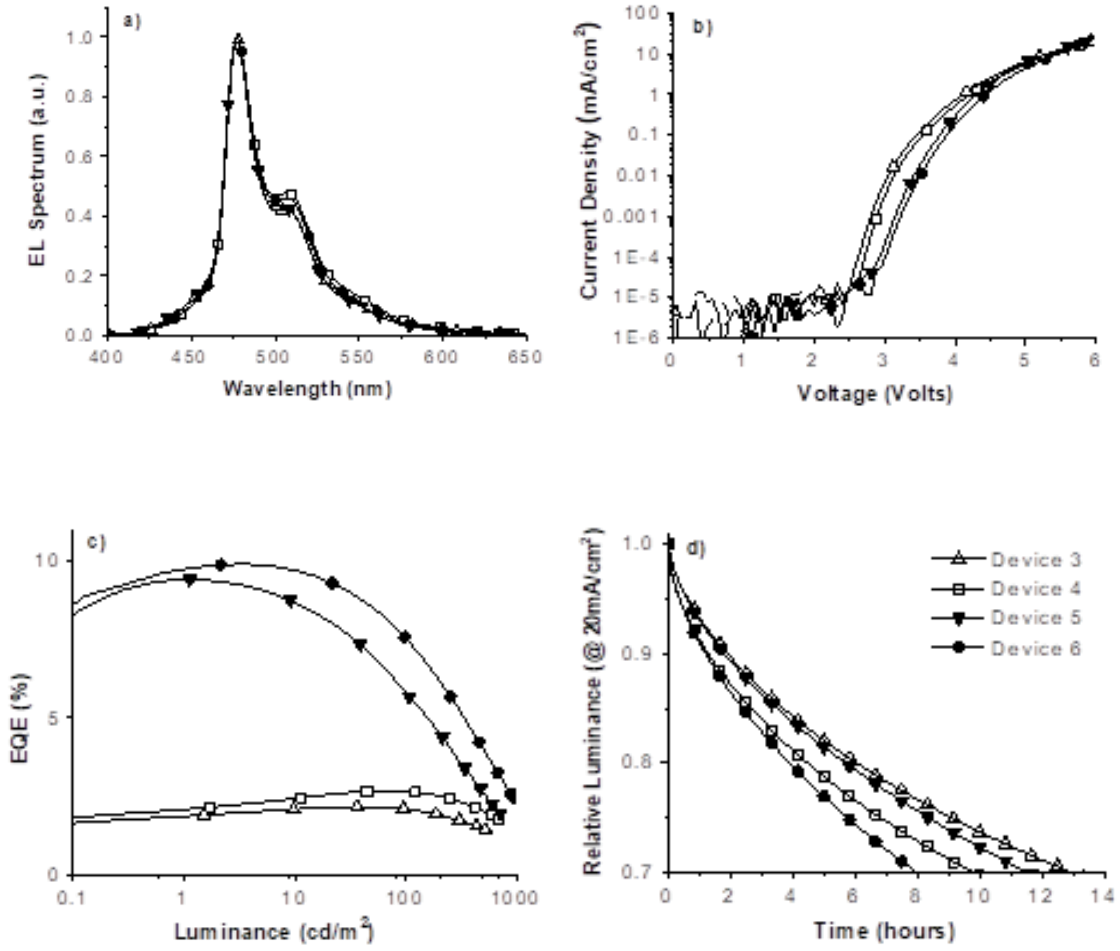

Figure 51: a) EL spectra, (b) current density vs voltage, (c) EQE vs luminance, and (d) plots of relative luminance vs. operation time for Device 3-6.

Meanwhile, device 6 showed the shortest operational lifetime LT_{70} of 8 h, while demonstrating the highest initial luminance of 930 cd m^{-2} as shown in Figure 51d. However, it should be noted that the estimated operational lifetime LT_{70} at 100 cd m^{-2} for device 6 turned out to be the highest at 354 h due to its high initial brightness.

In this section, the design and photophysical study of a series of deep blue MADF palladium (II) complexes have been reported. The introduction of two methyl groups on PdN1N dramatically improved the thermal stability while maintaining a blue emission spectrum (PdN1N-dm). Devices employing PdN1N-dm demonstrated an EL emission peak at 466 nm, CIE coordination of (0.14, 0.25), and the maximum EQE of 25.1 % in a known charge confined structure. The implementation of electrochemically stable charge blocking materials resulted in a stable device of PdN1N-dm demonstrating a maximum EQE of 9.8 %, CIE coordinates of (0.14, 0.32) and an estimated operational lifetime LT_{70} of 354 h at a brightness of 100 cd/m^2. Although the device performances reported here still cannot meet commercial requirements, the unique and innovative molecular design will serve as a promising strategy for the future development of efficient and stable blue OLEDs employing MADF materials.

3.3: PdON1a: Blue MADF with Improved Fluorescent Component

To continue the development of blue MADF emitters, focus was turned to the development of a MADF emitter with improved fluorescent emission component. This is necessary if MADF emitters will be implemented in display technologies as a result of the need for narrow "pure" blue emission. In order to evaluate the impact of such blue shifting on MADF materials PtON1a-TBU was developed, capable of sustaining deep blue emission as low as 430nm while maintaining a low triplet energy of 2.62 eV. Subsequently, its non-MADF analog PtON1a-DM-TBU is also studied to improve the understanding of these materials.

The room temperature absorption and emission spectra of PtON1a-tBu, PtON1a-DM-tBu and their analog (PtON1-tBu) are shown in Figure 52. Their photophysical and electrochemical properties are summarized in

Table 3. For all three platinum(II) complexes, the high energy absorption bands in the range of 250-330 nm (ε > 1.5×104 cm-1M-1) can be attributed to the $^1(\pi\ \pi^*)$ transitions on the cyclometalating ligands (LC). The relatively intense bands between 330-425 nm (ε > 5×10^3 $cm^{-1}M^{-1}$) are assigned to spin-allowed metal-to-ligand charge-transfer (^{1}MLCT) transitions involving both the cyclometalating ligands and the platinum metal ions.[116] Compared to PtON1a-DM-tBu, removing the two methyl groups from the pyrazole ring in PtON1a-tBu can significantly enhance the absorption intensities between 275-425 nm, due to the extended conjugation of the biphenyl-pyrazole moiety.

Table 3: Photophysical and Electrochemical Properties of the Platinum(II) Complexes (a) Measured in a CH_2Cl_2 solution at room temperature. (b) Measured in a 2-Me-THF solution at 77K. (c) Measured in a PMMA film at room temperature. (d) $k_r = \Phi/\tau$. (e) $k_{nr} = (1-\Phi)/\tau$. Where the k_r and k_{nr} are the radiative and non-radiative rate constants, respectively. (f) The HOMO and LUMO levels were calculated by using $Cp_2Fe^{0/+}$ values of 4.8 eV below the vacuum level. (g)Calculated from the λ_{max} of the 77K emission spectra measured in 2-Me-THF solution.

Complex name	PtON1a-tBu	PtON1a-DM-tBu	PtON1-tBu
Absorption (nm)	264, 303 ,352, 439	265, 299, 320, 366, 436	264, 294, 318, 363, 436
$\lambda_{max}{}^a$ *(nm)*	448, 482	444	444
$\lambda_{max}{}^b$ (nm)	472	438	438
$\lambda_{max}{}^c$ (nm)	470	442	449

Φ^{c} (%)	72	75	85
τ^{c} (μs)	54	5.5	4.5
$k_r^{c,d}$ ($10^4 s^{-1}$)	1.3	13.6	18.9
$k_{nr}^{c,d}$ ($10^4 s^{-1}$)	0.5	4.5	3.3
E_{ox} (V)	.49	0.53	0.48
E_{red} (V)	-2.65	-2.68	-2.63
HOMO[f] (eV)	-5.29	-5.33	-5.28
LUMO[f] (eV)	-2.15	-2.12	-2.17
T_1[g] (eV)	2.627	2.831	2.831

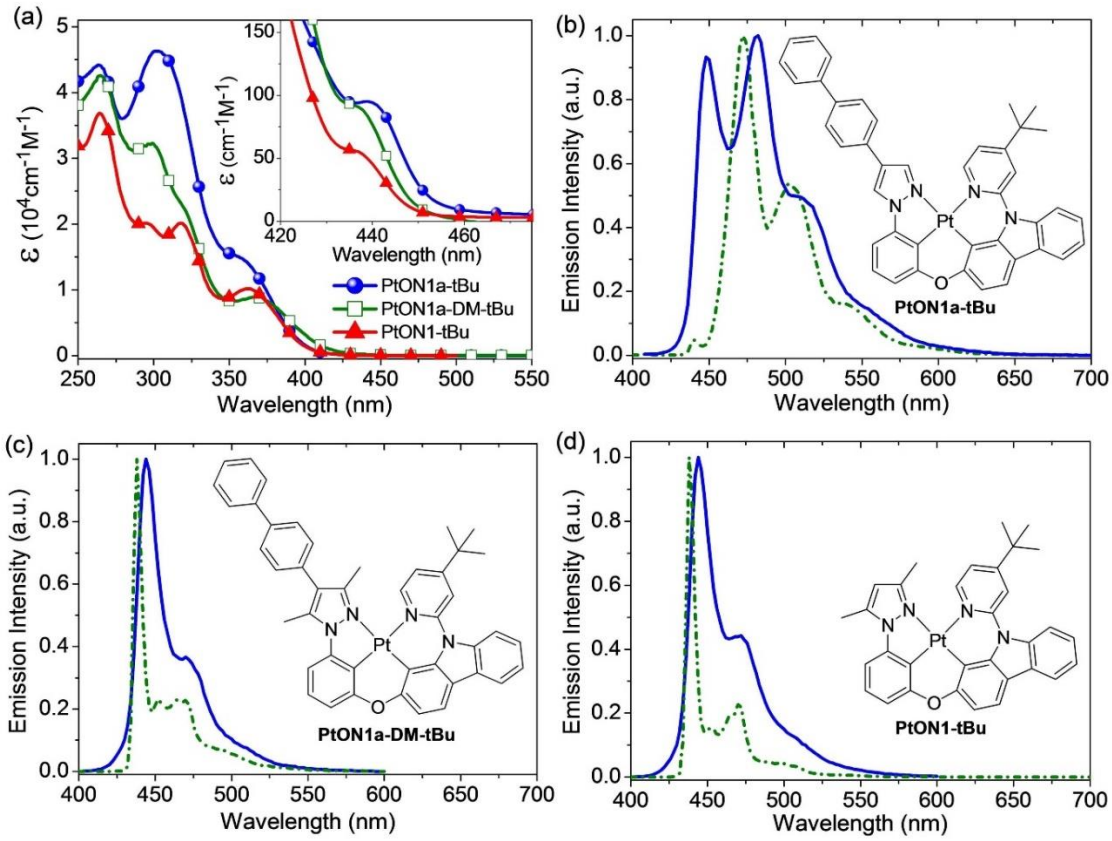

Figure 52:(a) UV-vis absorption spectra of PtON1a-tBu, PtON1a-DM-tBu and PtON1-tBu in CH2Cl2 solution at room temperature. The chemical structures (inset) and emission spectra of PtON1a-tBu (b), PtON1a-DM-tBu (c) and PtON1-tBu (d) in degassed CH2Cl2 (solid lines).

Moreover, the weak absorption bands in the 430-450 nm region ($\varepsilon < 100$ $cm^{-1}M^{-1}$) can be identified as direct absorption to the T_1 for PtON1a-DM-tBu and PtON1-tBu, and S_1 for PtON1a-tBu on the basis of the small energy shift between room temperature absorption and emission at 77 K. The T_1 absorption band for PtON1a-tBu is in the region of 455-470 nm with ε of 8-20 $cm^{-1}M^{-1}$. Structural modifications to the pyrazole rings with biphenyl group result in significant increases to the extinction coefficient of excited state absorption (Figure 52a). For example, molar absorptivity of the PtON1a-tBu at 439 nm ($\varepsilon = 95$ $cm^{-1}M^{-1}$)

and PtON1a-DM-tBu at 436 nm (ε = 92 $cm^{-1}M^{-1}$) is much larger than that of PtON1-tBu at 436 nm (ε = 60 $cm^{-1}M^{-1}$).

A set of blue emitting phenyl pyrazole based emitters and their corresponding emission spectra are shown in Figure 52b-d. The parent compound, PtON1-tBu, exhibits a narrow blue emission peaking at 438 nm at 77K in 2-methyltetrahydrofuran with a slight broadening, and redshift to 444 nm at room temperature in dichloromethane. On the basis of this spectrum a triplet energy of ~2.83 eV can be assigned to this molecule which renders it less compatible with many of the common carbazole based host materials like 4,4'-bis(N-carbazolyl)biphenyl (CBP, E_T = 2.65 eV), 3,3'-bis(N-carbazolyl)biphenyl (mCBP, E_T = 2.9 eV) or 2,6-bis(N-carbazolyl)pyridine (mCPy, E_T = 2.91 eV). [84,87] Upon the addition of biphenyl to the dimethyl pyrazole moiety for PtON1a-DM-tBu, minimal change to the emission at 77K or room temperature is observed with identical peaks at 438 nm and 444 nm respectively. If the two methyl groups are removed in the case of PtON1a-tBu, then the spectra at both 77K and room temperature are dramatically altered. Firstly, a significant red shift and broadening at 77K is observed. The red-shift to 472 nm is likely due to extended conjugation through the biphenyl pyrazole with broadened features resulting from the high degree of rotational freedom. At room temperature, an intense blue-shifted emission peak appears at 448 nm indicating the presence of a thermally activated emission pathway, similar to that which was observed for the PdN3N.[117] In this case, however, the splitting between the two emission bands is larger, and the higher energy emission state is much more intense. These two factors lead to a strong deep blue emitting component which will enable efficient blue and white devices despite a lower-lying triplet state at only 2.627 eV.

To further explore the nature of the blue-shifted emission, the emission spectra were collected at several temperatures from 77K to 298K as shown in **Error! Reference source not found.**. At 77K, a small emission feature at 440 nm can be observed, however, the emission is dominated by a vibronically structured emission peaking at 472 nm, which is attributed to phosphorescence from the lowest lying triplet state. However, at 140K, the small peak at 440nm completely disappears. This is a result of 2-MeTHF melting at 137K and becoming a solution. As the temperature is increased, the phosphorescence peak red shifts slightly as is typically observed for phosphorescent complexes. Also, beginning at about 200K the thermally activated emission at ~450 nm gains intensity as the temperature is increased. At room temperature, the thermally activated emission becomes to be even more intense than that of the lower energy triplet emission.

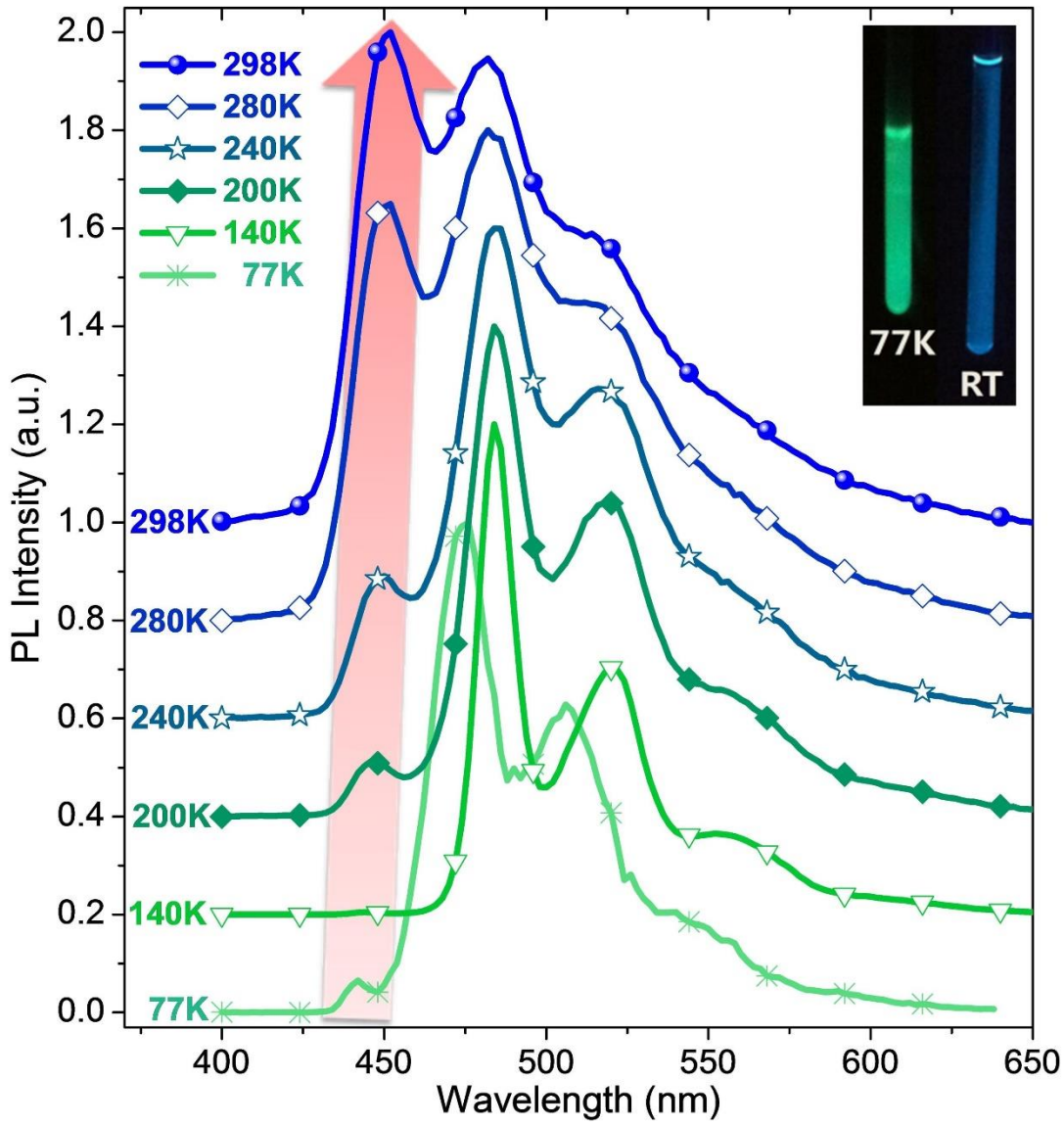

Figure 53: Emission spectra of PtON1a-tBu in 2-Me-THF solution at the variable temperatures ranging from 77K to 298K.

Further evidence for a thermally activated delayed emission process can be determined from the quantum yield and emission transient measurements of 5% doped PMMA films. The photophysical parameters for films of the three emitters are shown in. At room temperature, the emission in a doped PMMA film of PtON1a-DM-tBu has a

photoluminescent quantum yield (Φ) of 0.75 and a mono-exponential emission decay with a lifetime of 5.5 μs. These emission parameters are similar to those reported for PtON1-tBu and indicate very high radiative rates and low non-radiative rates, similar to those observed for many of the other tetradentate platinum(II) emitters.[75,83,110,116,118] At 77K, however, the decay is biexponential with the major component having a 9 μs lifetime and the minor component of 832 μs, indicating there may be a minor delayed component resulting from the addition of the biphenyl, but it does not contribute much to the emission at room temperature.

The emission for PtON1a-tBu was also very efficient with Φ of 0.72. In order to probe the decay of both the delayed emission band and the phosphorescence band, the transient decay was measured at both 450 nm and 525 nm. As seen in

Table 3, the decay is an order of magnitude slower ~50 μs for both emission bands. This results in the radiative rate of PtON1a-tBu being nearly ten times lower than PtON1a-DM-tBu and PtON1-tBu. It is worth noting that there was also a minor fast component with a lifetime of ~10 μs for both detection wavelengths of the PtON1a-tBu. At 77K, the emission is significantly slowed to 439 μs, indicating that emission from the lowest triplet state is inhibited compared to the dimethyl derivative of PtON1a-DM-tBu. The combined factors of the slower emission process and the red shift in emission indicate that the localization of the lowest lying triplet emitting at 472 nm is more ligand centered, due to the extended conjugation of the biphenyl-pyrazole moiety.

The photophysical properties of PtON1a-tBu, are very encouraging. Unlike most previously reported heavy metal phosphorescent complexes, a shorter wavelength peak

appears (~445 nm) at the elevated temperatures, indicating the presence of a thermally activated emission process. Furthermore, the green phosphorescent emission at 77K was shifted to a beautiful blue emission at room temperature, due to the increased intensity of higher energy delayed emission band compared to previous dual channel emitters (Figure 52 b).[32,117] Thus, this emitter makes a great candidate for blue and white OLED devices in carbazole based hosts due to its lower triplet energy level.

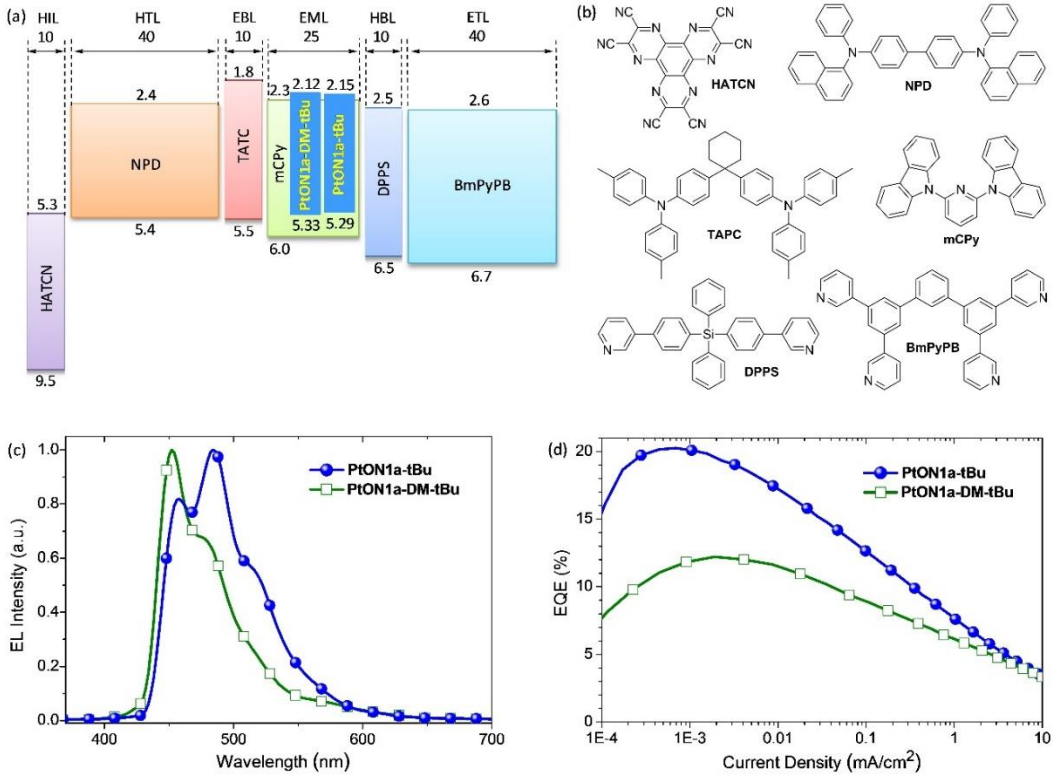

Figure 54: a) Energy level diagram of materials used in the devices. b) Molecular structures of the materials employed in the devices. c) The electroluminescent spectra of PtON1a-tBu and PtON1a-DM-tBu at room temperature. d) The plots of external quantum efficiency.

In order to characterize the electroluminescent properties of PtON1a-tBu and PtON1a-DM-tBu a series of devices were fabricated in structure ITO/HATCN (10 nm)/NPD (40 nm)/TAPC (10 nm)/6% dopant:mCPy (25 nm)/DPPS (10 nm)/BmPyPB

(40 nm)/LiF (1 nm)/Al shown in Figure 54a. The corresponding electroluminescent spectra are shown in Figure 54c. The EL spectrum at room temperature for PtON1a-tBu in mCPy shows similar features to the corresponding PL spectrum with a phosphorescent emission peak at 480 nm and a MADF emission peak at 450 nm. In contrast, the PtON1a-DM-tBu exhibits only a phosphorescent emission spectra peaking at 450 nm. The corresponding external quantum efficiencies (EQEs) plot for the device of PtON1a-tBu and PtON1a-DM-tBu is given in Figure 54d. The peak EQE for the PtON1a-tBu is over 20% while that of PtON1a-DM-tBu remains at just 12%. This is attributed to quenching of the triplets by the host material and is reflected in the PLQY of the doped thin films of $\Phi = 0.65$ and 0.43 for PtON1a-tBu and PtON1a-DM-tBu respectively. This result clearly indicates that the lower triplet energy (by nearly 0.21 eV) leads to greatly enhanced device performance despite both having significant emission in the deep blue range of 430-460 nm. Such drastic difference for the EQEs of PtON1a-DM-tBu and PtON1a-tBu devices strongly support the motivation behind achieving enhanced blue emission at a lower triplet energy and illustrates the potential advantage of this up-conversion strategy.

To further utilize the dual band nature of PtON1a-tBu, devices with a small 1% dopant concentration of an efficient blue fluorescent emitter TBPe were fabricated in the structure ITO/HATCN (10 nm) /NPD (40 nm)/TAPC (10 nm)/10% PtON1a-tBu:1% TBPe:mCPy (25 nm)/DPPS (10 nm)/BmPyPB (40 nm)/LiF (1 nm)/Al. The EQE and corresponding emission spectrum is given in Figure 55. As shown in the spectrum, the emission is generated exclusively on TBPe indicating efficient energy transfer from the platinum(II) complex to the fluorescent emitter. This efficient energy transfer leads to a substantial sharpening of the emission spectrum centered at 466 nm giving CIE coordinates of (0.14, 0.25) compared to (0.16, 0.27) for the reference device without the fluorophore.

These more ideal CIE coordinates are achieved by eliminating the vibrionic progressions in the 480-550 nm region that was attributed to the phosphorescence from PtON1a-tBu. The device efficiency suffered some losses in efficiency, peaking at only 14.1%. This loss is likely due to some direct charge trapping on the fluorophore which is unable to efficiently harvest the electrogenerated triplets. Nevertheless, the sharpening of the emission spectrum indicates the utility of fluorescent sensitized devices with a dual emission band phosphors.

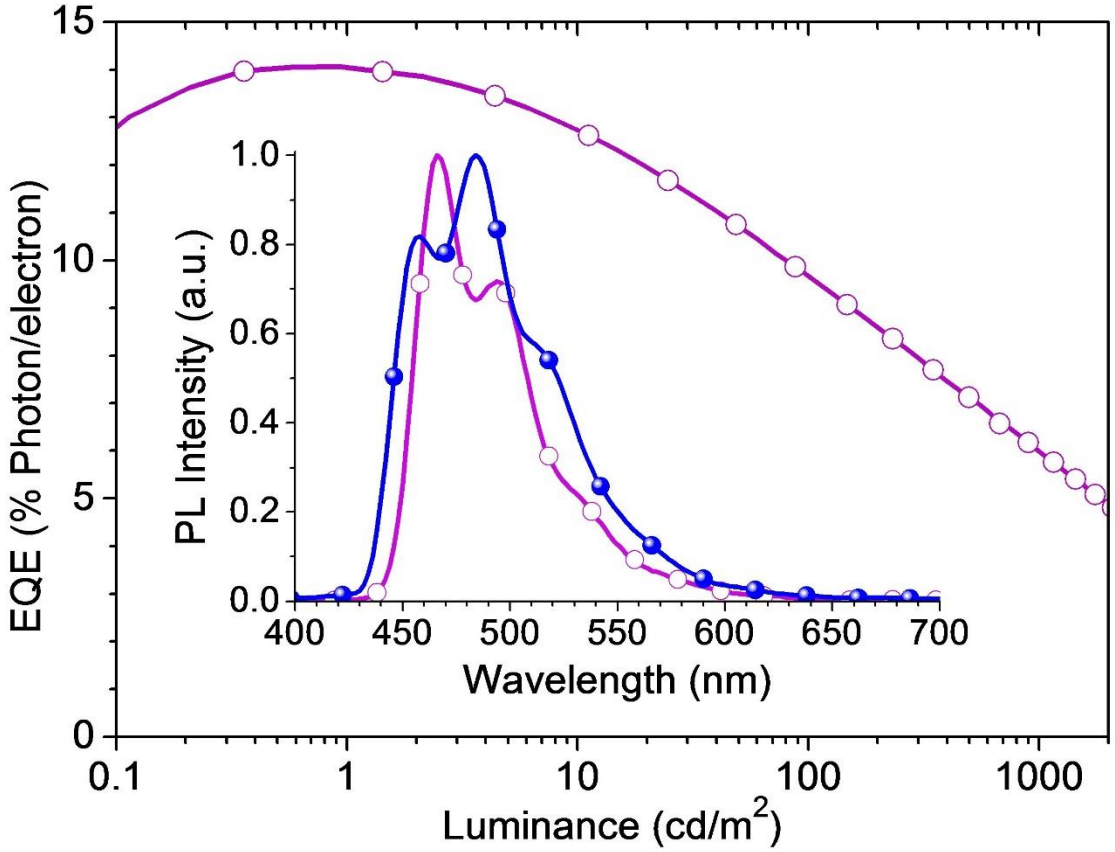

Figure 55: The external quantum efficiency versus luminance for devices in the structure: ITO/HATCN/NPD/TAPC/10% PtON1a-tBu:1% TBPe:mCPy/DPPS/BmPyPB/LiF/Al. The emission spectrum of the device (purple) is shown in the inset as well as the spectrum for the PtON1a-tBu reference device (Blue).

3.4: Conclusion

In this chapter a new technique for achieving efficient high energy emission from a molecules S_1 state while maintaining a lower T_1 is demonstrated. The conventional method for this is through TADF emission. However, this emission process is restricted by the size of the ΔE_{ST}, and can only approach 100% IQE at small ΔE_{ST} values. This means that the advantage of having a lower T_1 is reduced as T_1 is moved closer to the S_1 state. The dual emission pathway of MADF emitters allows for larger ΔE_{ST} emitters to maintain 100% IQE. This was demonstrated with three key emitters. PdN3N in a stable structure demonstrated a green OLED device with a peak EQE of 22% with an EQE at 1,000 cd/m^2 of 13.7% with an LT_{95} of 32 hours from a starting brightness of 4,100 cd/m^2. This demonstrates that the MADF emission system has the potential to be stable and efficient. Devices employing PdN1N-DM demonstrated a peak EL emission of 466 nm with CIE coordination of (0.14, 0.25), and the maximum EQE of 25.1 % in a charge confined structure. Additionally, in a stable structure PdN1N-dm demonstrating a maximum EQE of 9.8 %, CIE coordinates of (0.14, 0.32) and an estimated operational lifetime LT_{70} of 354 h at a brightness of 100 cd/m^2. This shows proof of concept for developing higher energy MADF emitters that have the potential for stable and efficient emission. Finally, a charge confined device of PtON1a-tBu demonstrated a peak EQE above 20% with CIE coordinated of (0.16, 0.27), an emission onset at 425 nm and a MADF to phosphorescent peak ratio of over 80% in a standard host of mCPy26. This validated the compatibility of deep blue MADF emitter in conventional hosts. The work in this chapter has the potential to revolutionize the way the community approaches deep blue OLED emitter design.

4: Development of New Host Materials

In a conventional OLED host-guest emissive layer the triplet energy of the host material must be higher than the triplet energy of the emitter to ensure efficient energy transfer from host to the dopant via the Förster or Dexter energy transfer mechanisms.[119–121] Host materials require a triplet energy over 2.8 eV to be compatible with common deep blue emitters (E_T of 2.70-2.75 eV).[122] Thus, host materials must adopt core structures with high E_T, like carbazole, triphenylamine, fluorene, dibenzofuran, dibenzothiophene, arylsilane, diphenylphosphine oxide and dimesitylborane.[122–124] Moreover, large conjugated systems should be avoided, this can be achieved by employing sp^3-hybridized atom linkers, ortho or meta substituted aromatic structures, or large sterically hindered molecular structures.[122] Furthermore, to enhance the stability of the host materials, both thermal and electrochemical stabilities are critical and must be considered. Thus, core structures like diphenylphosphine oxide and dimesitylborane are less suitable because of their poor thermal or electrochemical stability.

Based on the above guidelines, many excellent host materials have been developed.[122–124] Carbazole moiety is the most widely utilized core structure in host materials, such as the well-known hosts 4,4'-bis(9-carbazolyl)-1,1'-biphenyl (CBP), 3,3'-bis(9-carbazolyl)-1,1'-biphenyl (mCBP) and 4,4'-bis(9-carbazolyl)-2,2'-dimethyl-1,1'-biphenyl (DmCBP) with E_T's of 2.55, 2.9 and 3.0 eV, respectively.[87] These structures indicate that the position of substituents and the steric hindrance of a molecule can significantly alter the E_T. These host materials have been widely used in stable and efficient red,[50,58,70] green,[69] and blue[63,67,74,125,126] OLEDs. For example, Chapter 2.1 concluded with a sky-blue phosphorescent OLED employing mCBP as the host and PtNON (ET=2.83 eV) as the dopant. This device demonstrated an estimated LT_{70} from a starting brightness of 1,000

cd/m^2 over 1,330 hours with an EQE at 1,000 cd/m^2 of 17.4% and CIE coordinates of (0.19, 0.41). In 2018, Adachi and co-workers also adopted mCBP as the host material to fabricate a sky-blue OLED (CIEy<0.4) with an EQE of 16.6% and an operational lifetime to 90% initial luminance at 1,000 cd/m^2, of ~38 h using 3Ph2CzCzBN (E_T: 2.55 eV) as a TADF emitter.[127] Because of fluorenes relatively low E_T (2.95 eV),[128] fluorene-based host materials with an E_T over 2.80 eV are relatively scarce.[128,129] However, in 2006, Shu and co-workers developed a series of carbazole/fluorene hybrids with E_T of 2.88 eV. When implemented as host materials for the well-studied blue emitter FIrpic (E_T: 2.65 eV) a peak EQE of about 12.5% was achieved.[130] In 2007, Qiu and co-workers designed a sterically hindered carbazole/fluorene hybrids incorporating four tert-butyl groups (TBCPF) to demonstrate a peak EQE of 12.9% in a FIrpic-doped blue OLEDs.[129] A high E_T alternative to carbazole/fluorene hybrids can be achieved by implementing Si into the host structure. The sp^3-hybridized Si can break up the conjugation of host molecules resulting in a wider energy gap and higher E_T. Thus, many high E_T host materials containing a tetraphenylsilane moiety have been developed.[131–140] In 2004, Forrest, Thompson and co-workers reported the first series of triphenylsilane-based host materials with E_T of ~3.5 eV, and successfully fabricated a deep blue OLED doped with FIr6 (E_T: 2.72 eV) with an EQE of nearly 10%.[97] After that, several other types of Si-based host materials incorperating carbozole, triphenylamine,[135,136] oxadizole,[137] carbozale/diphenylphosphine oxide,[138] or spiro-annulated fluorene/triphenylamine moiety,[139,140] were also developed. Most of these Si-

based host materials were shown to be compatible with the blue emitter FIrpic and achieved EQE's ranging from 13.1% to 18.7%.[108,131,133,134,136–140]

4.1: "M"-Type Hosts

In this chapter, we describe the design and implementation of two novel carbazole/fluorene and carbazole/9-silafluorene hybrids with high triplet energies to act as stable host materials shown in Figure 56. Fluorene and carbazoles were connected at their 9-position with two para-substituted phenyl groups to afford a "V"-type molecule 9,9-bis(4-(9H-carbazol-9-yl)phenyl)-9H-fluorene (pDCzPF) shown in Figure 57a. The conjugation system of this molecule is disconnected by a sp^3-hybridized carbon atom to give a high E_T of 2.88 eV, which also exhibits a high glass transition temperature of 165°C, and a high decomposition temperature of over 500°C.[129] However, if a meta-substituted phenyl group is used as a linker, a more rigid "M"-type molecule 9,9-bis(3-(9H-carbazol-9-yl)phenyl)-9H-fluorene (mDCzPF), can be obtained with the same E_T. Moreover, the E_T could be further increased by incorporating 9-silafluorene with a sp^3-hybridized silicon atom. This results in another "M"-type molecule 9,9-bis(3-(9H-carbazol-9-yl)phenyl)-9H-silafluorene (mDCzPSiF) with a higher E_T of 3.03 eV.

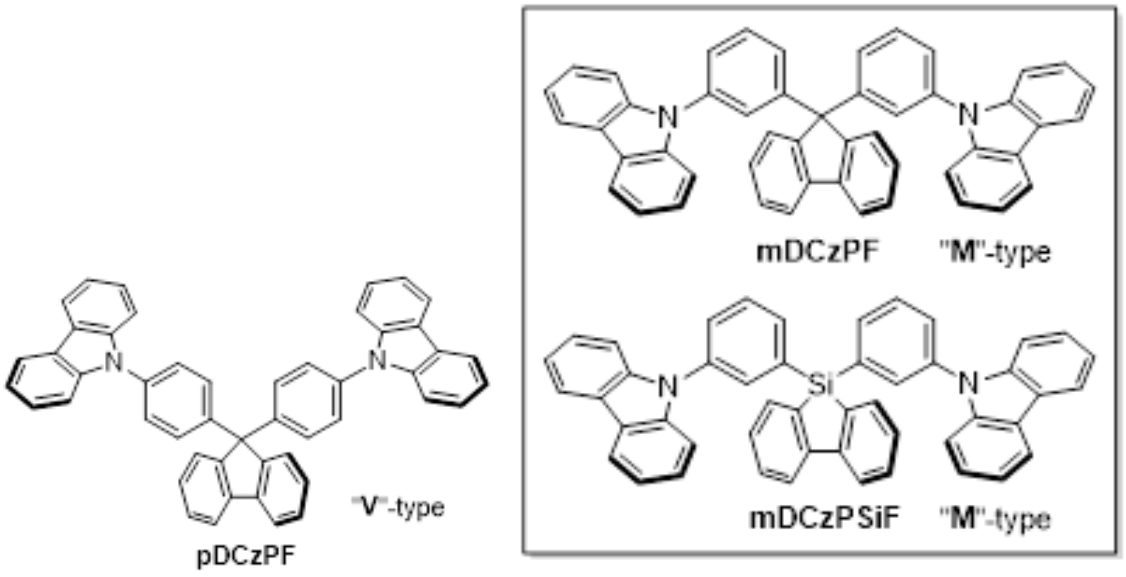

Figure 56: Molecular Structures of the newly developed "M"-type host materials and the structure of "V"-type host.

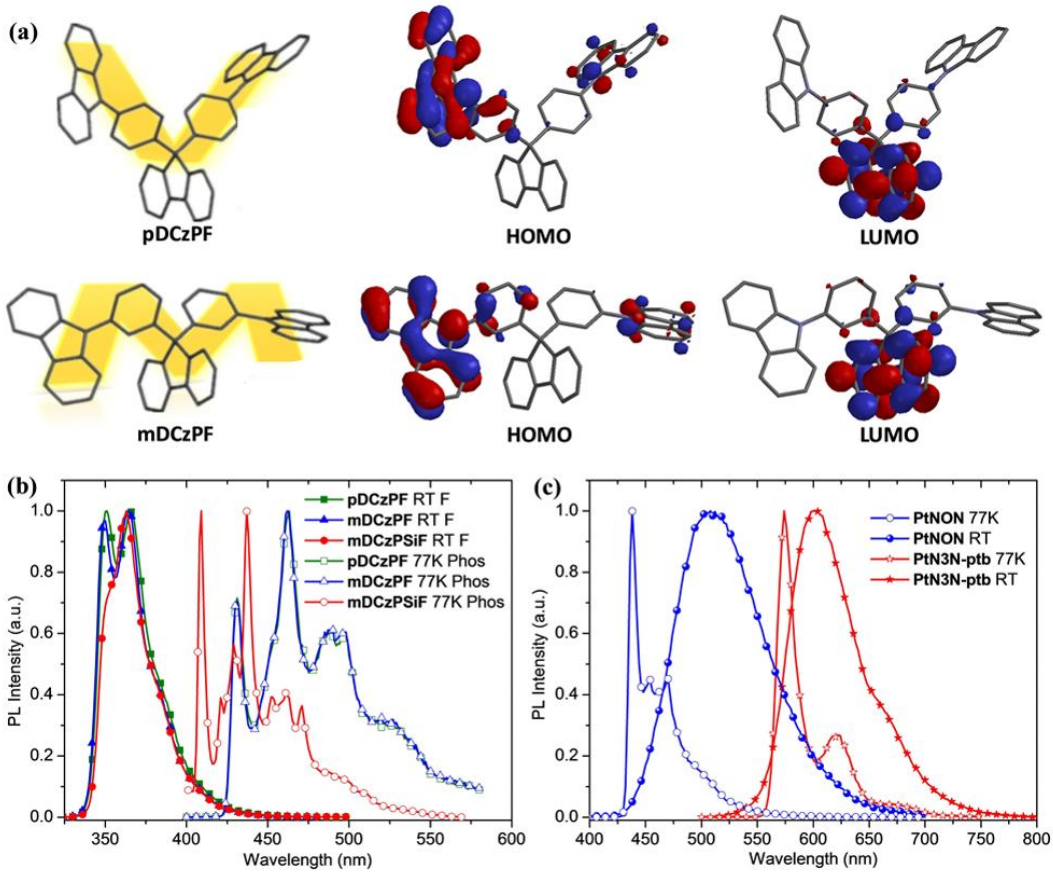

Figure 57: (a) Optimized structures, HOMO and LUMO distributions of pDCzPF and mDCzPF calculated by DFT (Titan/B3LYP/6–31G*). Hydrogen atoms were omitted for clarity. (b) The fluorescent spectra of pDCzPF, mDCzPF and mDCzPSiF in CH2Cl2 solution at room temperature.

Density functional theory (DFT) calculations were performed to optimize the ground state of the host materials, the calculation results are shown in Figure 57a. The highest occupied molecular orbitals of the carbazole/fluorene hybrids pDCzPF and mDCzPF mainly consist of carbazole-π orbitals with a small contribution from the phenyl-π orbitals, while their lowest unoccupied molecular orbitals predominantly occupy on the fluorene-π orbitals. Similar HOMO and LUMO distributions are observed in the carbazole/9-silafluorene hybrid mDCzPSiF molecule. All the phenyl-carbazole moieties in the hybrids are non-planar indicating a high rigidity of the molecules. Additionally, the two electron-donating carbazole

groups in the "M"-type mDCzPF are much farther from each other than those in the "V"-type pDCzPF, further indicating a more rigid molecular configuration. The two carbazole groups arrange in an opposite vector direction, resulting in a very small dipole moment of only 0.50 Debye for the "M"-type mDCzPF compared to 2.25 Debye for the "V"-type structure (Table 4). This may be advantageous to prevent charge trapping in the EML.

Table 4: Photophysical and electrochemical properties of host materials.

Compound	77K λ_{PL} [nm]	E_T [eV]	HOMO/LUMO [eV]	Dipole moment [Debye]
pDCzPF	431	2.88	-5.32/-1.82	2.25
mDCzPF	431	2.88	-5.38/-1.80	0.50
mDCzPSiF	409	3.03	-5.45/-1.70	1.03
CBP	486	2.55	-6.0/-2.9	0.21

The fluorescent spectra of the pDCzPF, mDCzPF and mDCzPSiF in a dichloromethane solution at room temperature and their phosphorescent spectra in 2-methyltetrahydrofuran solution at 77K are shown in Figure 57b. Both the carbazole/fluorene hybrids pDCzPF and mDCzPF exhibit a structured fluorescent emission spectra at room temperature with peaks at 350 and 365 nm and transient decay lifetimes (τ) of 4.5 and 4.7 ns, respectively. At 77 K, they show nearly identical phosphorescent spectra with a peaks at short wavelength of 431 nm and τ's in the microsecond range. Thus, the E_T of both pDCzPF and mDCzPF is calculated to be 2.88 eV, which is higher than the E_T of most common deep blue phosphorescent emitters (E_T: 2.70-2.75 eV).[141] The carbazole/9-silafluorene hybrid mDCzPSiF has a fluorescent spectrum at room temperature peaking at

363 nm with a higher energy shoulder at 352nm, however, its phosphorescent spectra at 77 K is significantly blue-shift compared to that of the pDCzPF and mDCzPF, with the first peak at 409 nm. Hence, the E_T of the mDCzPSiF is calculated to be 3.03 eV, which is higher than previously reported tetraphenylsilane/carbazole-based host materials.[97,129,130]

Tetradentate Pt(II) complex PtN3N-ptb has been shown to be an extremely stable phosphorescent red emitter in a host of CBP.[58] To evaluate the operational stability and electroluminescent (EL) properties of pDCzPF, mDCzPF and mDCzPSiF compared to the standard host CBP devices were fabricated and tested using a known stable device structure of, ITO /HATCN (10 nm) /NPD (40 nm) /10% PtN3N-ptb:Host (25 nm) /BAlq (10 nm) /BPyTP (40 nm) /LiF (1 nm) /Al (100 nm. BAlq was selected as the hole blocking material because of its deeper HOMO level (-6.2 eV) than the host materials (-5.32–-6.0 eV), allowing for exciton formation to be confined inside of the EML. Figure 58 shows a) an energy level diagram and the chemical structures of the materials used in the PtN3N-ptb-doped OLEDs, b) the electroluminescence (EL) spectra, c) current density vs voltage characteristics, d) external quantum efficiency vs luminance and e) device operational time vs brightness. All four devices showed broad emission spectra in red visible region with a dominate peak at about 606 nm with a vibronic sideband at 660 nm.

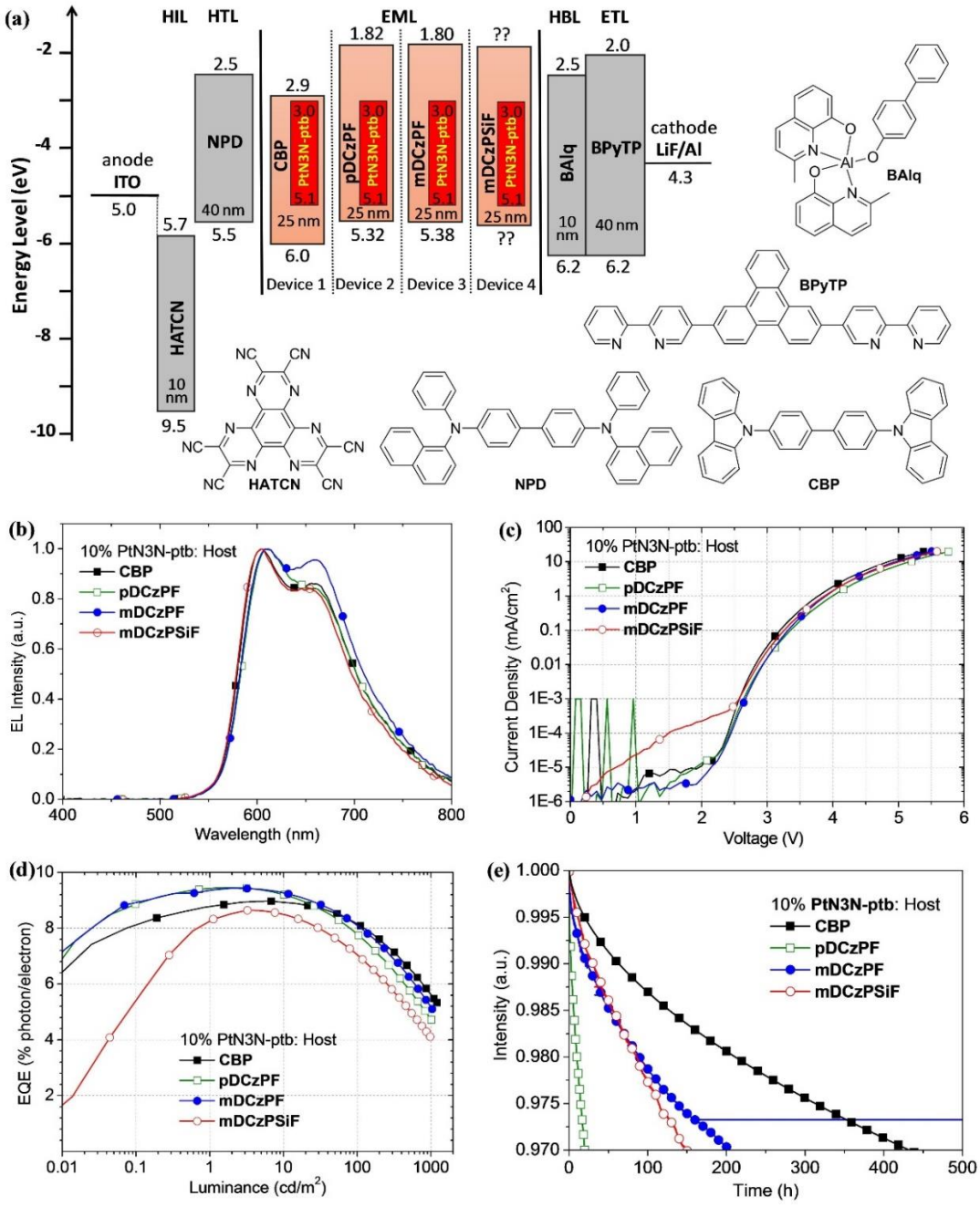

Figure 58: (a) Energy level diagram and chemical structures of the materials for the PtN3N-ptb-doped OLEDs (devices 1-4) using CBP, pDCzPF, mDCzPF or mDCzPSiF as hosts. (b) EL spectra, (c) Current density–voltage (J–V) characteristics, (d) external quantum efficiency (EQE) versus luminance plots (e) Luminance intensity-time curves of devices 1-4. HIL, hole injection layer; HTL, hole transporting layer; EML, emissive layer; HBL, hole blocking layer; ETL, electron transporting layer.

These devices exhibited low turn-on voltages of 2.5±.2 V. Devices 2 and 3, using pDCzPF and mDCzPF as hosts and demonstrate a peak EQEs of 9.5% and 9.4% respectively. It should be noted that this is superior to that of the device 1 with CBP as host. Additionally, device 3 using the "M"-type mDCzPF as host demonstrated a very good operational lifetime, LT_{97} of 205 h, with an initial luminance (L_0) of 1036 cd/cm^2, which represented a tenfold lifetime improvement over the device 2 using the "V"-type pDCzPF as host. The "M"-type pDCzPSiF based device 4 also exhibited significantly improved operational lifetime over the "V"-type pDCzPF (Table 5). The improvement in device lifetime could be attributed to the more rigid molecular configuration and small dipole moments of the "M"-type host materials that help prevent charge trapping in the EML.[142] While these "M"-type hosts do not demonstrate an operational lifetime comparable to that of CBP it is important to note that their significantly higher E_T, compared to CBP, makes them more compatible with deep blue emitters. These results demonstrated that the newly developed "M"-type mDCzPF and mDCzPSiF have the potential to be a stable and efficient host for phosphorescent OLEDs.

Table 5: Summary of PtN3N-ptb device performance.

Device	Host	Peak EQE [%]	L_0 [cd/m^2]	LT_{97} [h]
1	CBP	9.0	1200	432
2	pDCzPF	9.5	1010	20
3	mDCzPF	9.4	1036	205
4	mDCzPSiF	8.6	975	150

To further evaluate the potential application of the "M"-type host material mDCzPF in a blue phosphorescent OLEDs with high E_T, devices using the tetradentate Pt(II) complex PtNON, were evaluated. As shown in chapter 2 PtNON has a 77k emission peaking at 438 nm in 2-MeTHF suggesting it has a high E_T of 2.83 eV. Devices were fabricated and tested using strong charge blocking materials with a structure of HATCN (10 nm) /NPD (40 nm) /TrisPCz (10 nm) /10% PtNON: Host (25 nm) /DPPS (10 nm) /BPyTP (40 nm) /LiF (1 nm) /Al (100 nm). MCPy26 was utilized as a reference host for its high ET (2.91 eV) and wide uses in efficient green,[69,143] blue,[69,83,114,118] and white[144–147] OLEDs. Figure 59 show a) an energy level diagram and the chemical structures of the materials used b) the EL spectra, c) current density vs voltage characteristics, d) external quantum efficiency vs luminance and e) device operational time vs brightness.

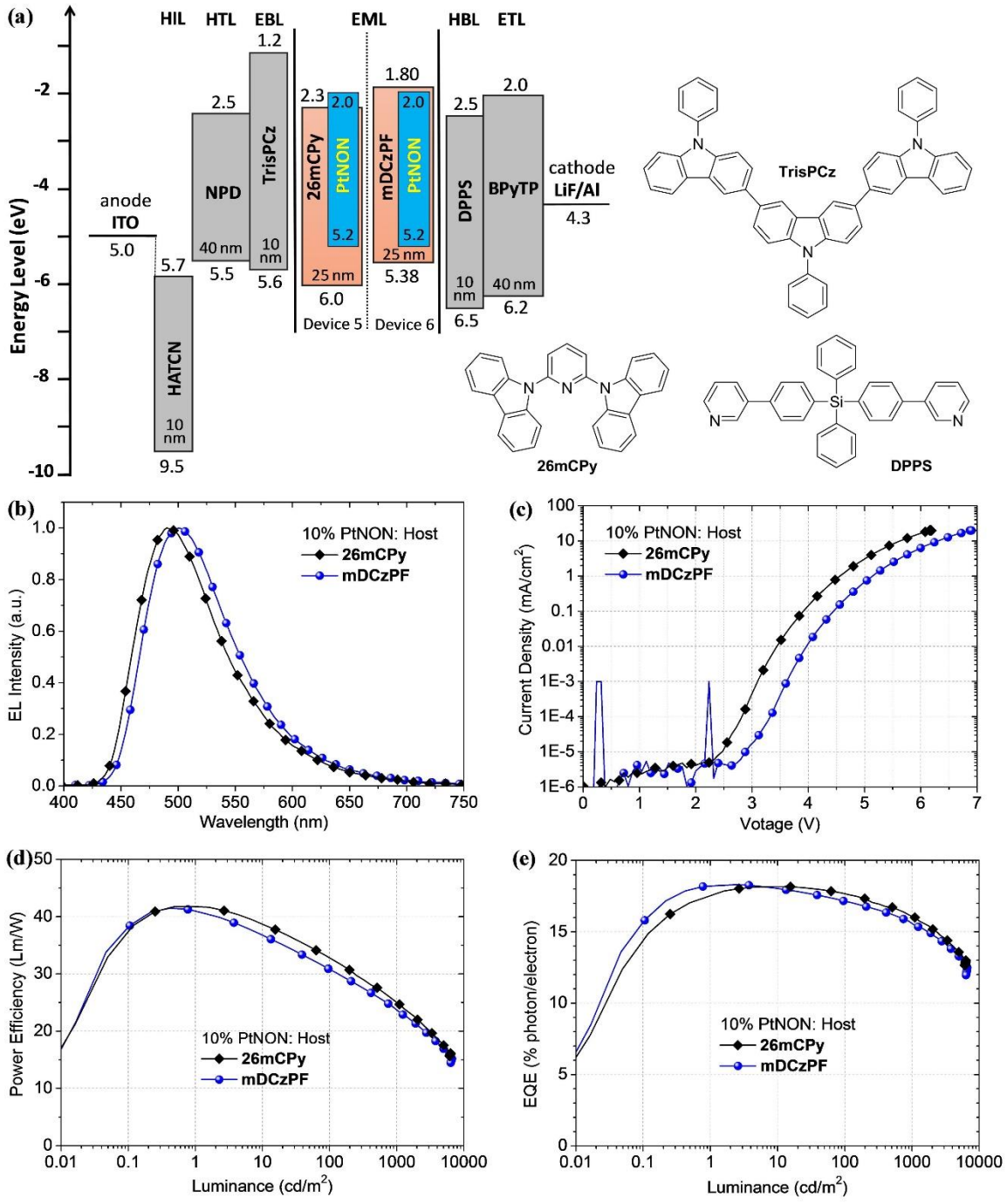

Figure 59: (a) Energy level diagram and chemical structures of the materials for the PtNON-doped OLEDs (devices 5, 6) using 26mCPy or **mDCzPF** as hosts. (b) EL spectra, (c) Current density–voltage (J–V) characteristics, (d) Power efficiency-Luminance (P–L) characteristics, and (e) external quantum efficiency (EQE) versus luminance plots of devices 5 and 6. EBL, electron/exciton blocking layer.

The EL spectrum of the device 6 employing mDCzPF is slightly red-shifted and broadened compared to that of device 5 (Figure 59b). This may result from the slightly more planer shape of mDCzPF compared to 26mCPy, however more experimentation would be required to fully validate this hypothesis. The energy diagram in Figure 59a shows the large 0.7 eV barrier between the LUMO levels of DPPS and mDCzPF compared to a 0.2 eV barrier between DPPS and 26mCPy. This is likely responsible for the increased turn-on voltage from device 5 to device 6. Both devices also exhibit a high peak power efficiency of over 40 Lm/W. Most importantly, device 6 employing the "M"-type mDCzPF as a host demonstrated a peak EQE of 18.3% with a low roll off to 17.1% and 15.6% at 100 and 1000 cd/m^2 respectively. This demonstrates that this newly developed "M"-type host is compatible with high E_T emitters.

4.2: Conclusion

In this chapter a novel "M"-type carbazole/fluorene hybrid called mDCzPF and a carbazole/9-silafluorene hybrid called mDCzPSiF are reported. Both these materials have high E_T achieved by utilizing the meta-substituted phenyl groups as linkers. Red phosphorescent OLEDs using these "M"-type mDCzPSiF and mDCzPF as hosts represented a 7 to 10-fold operational lifetime improvement over the "V"-type pDCzPF based OLED. Additionally, the "M"-type mDCzPF was implemented as a host with the high E_T emitter PtNON (2.83 eV). PtNON doped OLED using mDCzPF as host exhibited a peak EQE of 18.3% with a low roll-off. Finally, the rigid molecular configuration and small dipole moment of the "M"-type host molecules is shown to play a critical role in the device performance. This provides a viable method for new host material design in the development of stable and efficient phosphorescent OLEDs.

5: Optical Extraction

Optical modeling, simulation, and optimization of OLED devices represents an area of research that can potentially have a massive impact on OLED performance. It is widely advertised that phosphorescent OLEDs can operate at 100% internal quantum efficiency. Despite this, a conventional bottom emitting OLED can only attain an EQE of 20-25%, resulting from 75-80% of the generated light remaining trapped in the device.[93,148] Fortunately, the majority of these optical losses are recoverable through various techniques. For this section, we will focus on optical extraction techniques that can be employed on conventional bottom emitting OLED (Figure 60a) devices with ITO as the anode and aluminum and the cathode. It should be noted that the optics of an OLED device will change dramatically in an inverted bottom emitting structure (Figure 60b) or a top emitting OLED (Figure 60c). Inverted OLED structures are a colloquial term for a device where the transparent conductor (typically ITO) is used as the cathode, and the reflective metal layer is used as the anode. Top emitting OLEDs are devices that do not emit light through the substrate, they typically have a semi-transparent top layer to allow light to be emitted from the organic side of the device.

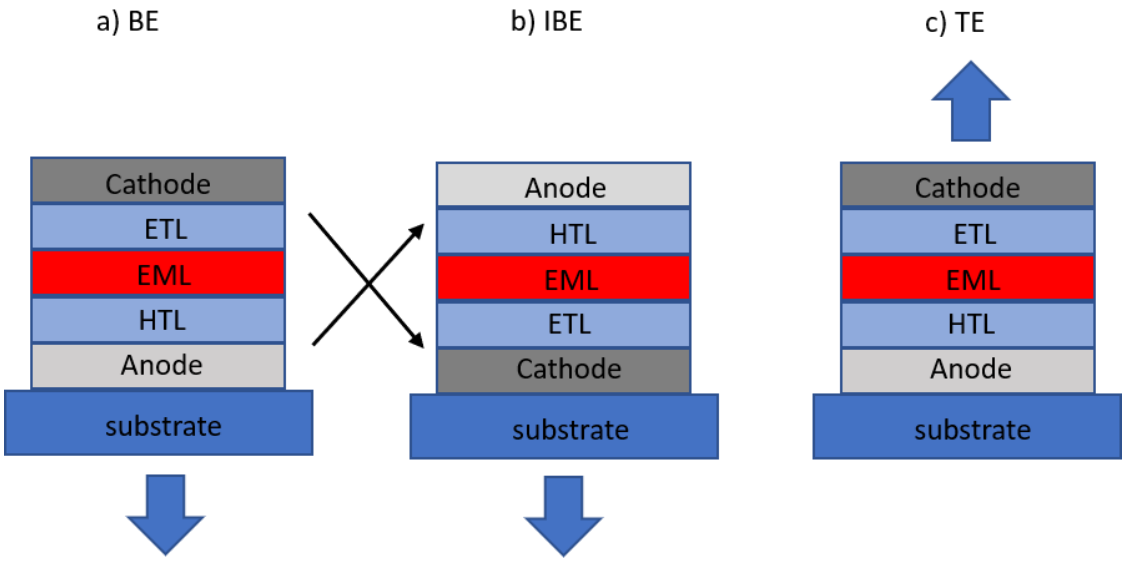

Figure 60: Schematic showing general layer structure and emission direction for a) bottom emitting OLED, b) inverted bottom emitting OLED, c) Top emitting OLED.

As previously mentioned, there are a wide range of optical extraction techniques being developed for OLED devices. These techniques can be broadly separated into three main groups, 1: internal extraction techniques, 2: external extraction techniques, 3: intrinsic material techniques. Internal extraction techniques are defined as alterations to the internal optical structure of the OLED device. This included internal diffraction layers, corrugated substrates, microcavity's, and techniques to suppress plasmon quenching. Internal diffraction layers and corrugated substrates share a similar purpose. Their primary function is to break up the planer nature of an OLED in order to reduce total internal reflection. This can be done by adding periodic or random structures to the substrate, or high refractive index anode layer (Figure 61). This technique has the potential to be compatible with roll to roll processing and is in the early stages of being evaluated by the OLED industry. Corrugated substrates can achieve high extraction enhancement on the order of 1.7-1.9 times.[149,150]

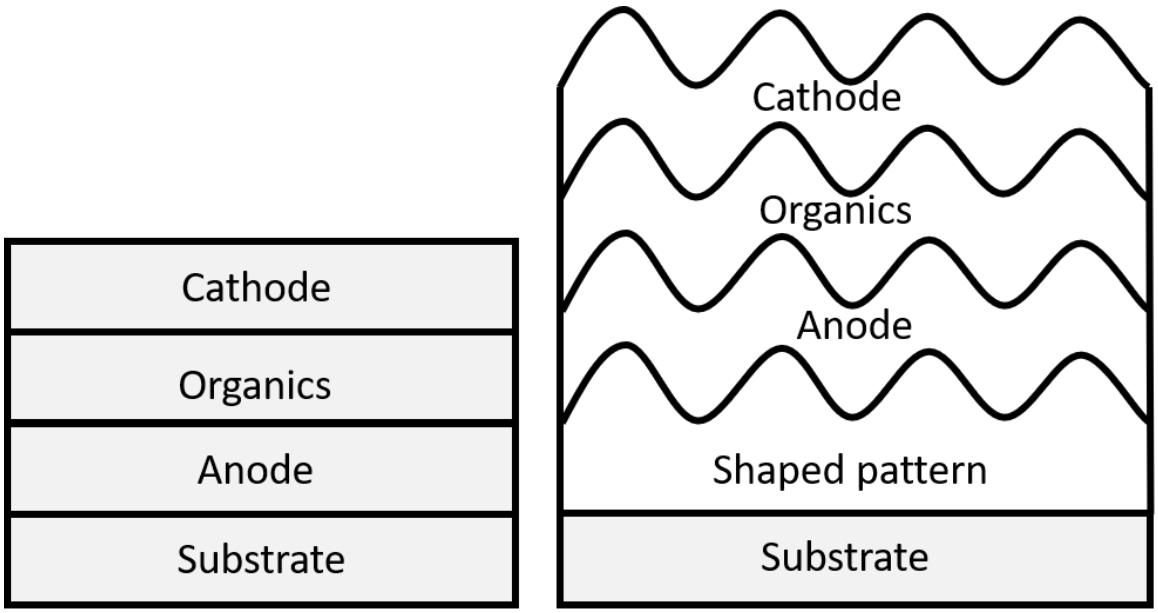

Figure 61: planer vs corrugated substrate schematic.

Microcavities employ a stack of alternating high and low refractive index layers between the ITO and the substrate. By tuning the thickness of the organic layers in the device, an optical cavity can be formed creating a constructively interfering standing wave in the device. This technique has proven useful for enhancing the light extraction of monochromatic OLEDs. Microcavities have demonstrated a 1.4 times enhancement when property tuned and applied to devices. [151–153]

External extraction techniques are comprised mainly of microlenses and scattering layers. They have the advantage of being an ex situ process to the OLED fabrication. This means that no changes need to be made to the manufacturing process, but light extracting can still be enhanced. Microlenses are typically produced as an adhesive film that can be applied to the glass substrate to reduce total internal reflection inside the substrate. This

technique can have a low cost and high impact on the device performance with some extractor layers reaching 1.7 times enhancement. [154–156]

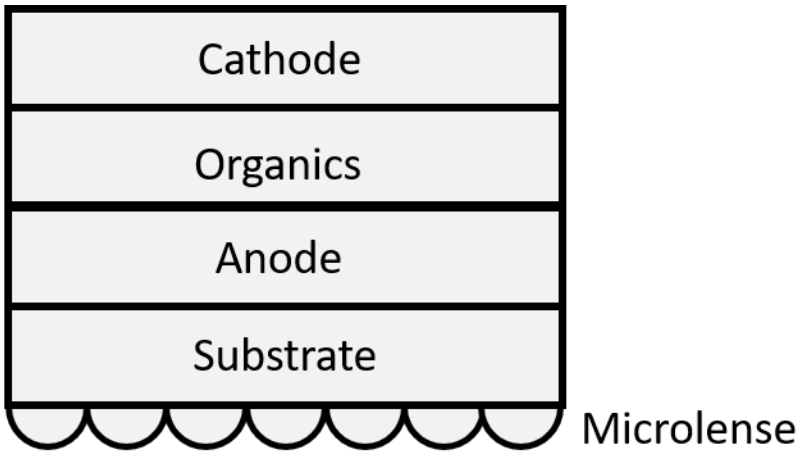

Figure 62: Schematic of microlense array on substrate.

Intrinsic material techniques are a general term for altering the physical OLED stack in the device to alter the optical properties. The most common application of this technique is changing the thickness of the hole transport layer to optimize the OLED stack for a specific wavelength of light.[143] Other common applications of this technique include designing lower refractive index materials or using materials with birefringent properties.[157–159] The common goal of this is to optimize and tune the OLED stack to minimize organic waveguide losses.[155] These techniques tend to involve more rigorous research to optimize. This is a result of changes to the organic materials often altering the electrical performance of the device, resulting in the need to re-optimize the electrical and optical performance of the device after a change in material. Finally, one of the most promising techniques for improving OLED optical performance is the development of oriented emitters. The spontaneous emission direction of a photon with respect to an organic molecule occurs

perpendicular to its transition dipole moment vector (TVD). [160] If the TVD's of the emitting molecule can be oriented parallel to the substrate, the need for many extraction techniques can be greatly reduced or eliminated. Despite this technique being widely studied, there remains a limited understanding of design rules for achieving this preferential orientation.[93,115,148,161]

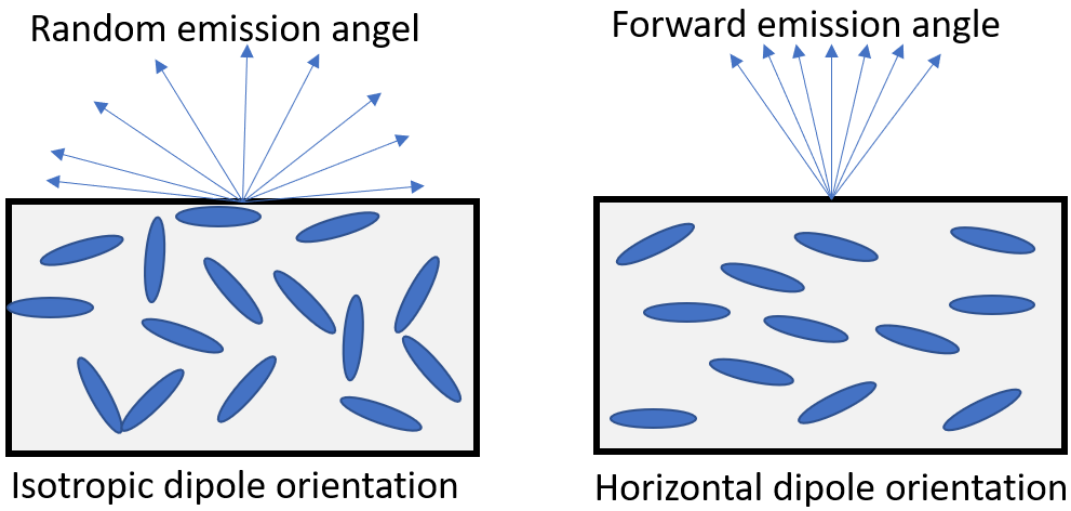

Figure 63: Schematic showing isotropic vs horizontal dipole orientation and its impact on emitted light.

For OLEDs to break many of their barriers to wide spread adoption their performance must continue to improve while the cost lowers. Keeping this fact in mind research was focused on improving light extraction while maintaining low fabrication cost. Prior to designing low-cost optical extraction techniques our conventional OLED structure must be modeled and simulated to identify existing inefficiencies in our structure.

A wide range of simulation techniques exist for modeling the optical structures in an OLED device. These range from simple techniques such as ray optics to the more detailed

simulations such finite-difference time-domain(FDTD) calculation. Simple simulations like ray optics are useful for estimating things like total internal reflecting angle. However, to obtain meaningful quantitative information about the emission process, loss channels and external performance of an OLED a much more intensive simulation is required. The current widely accepted technique for this is based on the theory of radiating dipoles in close proximity to plane interfaces. [162,163] Fluxim's Setfos package is a powerful user-friendly simulation software package that allows for complex dipole model simulations to be carried out with a high degree of accuracy. However, since this software is an off the shelf package, we wanted to begin by validating the accuracy of the model against previous simulations and experiments.

5.1: Setfos Simulations

The experiment we chose to simulate in Setfos are part of a former group member's dissertation from May 2014.[164] His work involved optimizing microcavities using finite FDTD simulations, he was able to demonstrate that the simulations he ran (shown in Figure 64a, c) proved to be closely matching to experimental data collected. Figure 64 shows the simulated outcoupled spectrum and simulated air mode extraction for a variety of microcavity devices. The devices that were simulated have an structure of Glass/ DBR cavity structure (x pairs)/ ITO (53nm)/ Hat-CN (10nm)/ NPD (Ynm)/ TAPC (10nm)/ mCPy26 (25nm)/ DPPS (10nm)/ BmPyPB (45nm)/ LiF (1nm)/ Al (100nm) where the distributed Bragg reflector (DBR) cavity consisted of layers of alternating Ta_2O_5 (n=2.2) and SiO_2 (n=1.46) to create the DBR stack. These stack have the structure Ta_2O_5 (57nm)/ SiO_2 (100nm)/ ITO (53nm) for 1 pair, Ta_2O_5 (57nm)/ SiO_2 (83nm)/ Ta_2O_5 (57nm)/ SiO_2 (100nm)/ ITO (53nm) for 2 pair, and Ta_2O_5 (57nm)/ SiO_2 (83nm)/ Ta_2O_5 (57nm)/ SiO_2 (83nm)/ Ta_2O_5 (57nm)/ SiO_2 (100nm)/ ITO(53nm) for 3 pair. Additionally the thickness of

the NPD was varied from 30nm to 60nm to evaluate how well the software handles the complex optical structure. The slight deviations between FDTD and Setfos likely arises from the use of spectroscopically dependent complex n and k values in Setfos vs simplified 'n only' values being used in FDTD. Despite this, it is apparent that the Setfos software shows a high degree of accuracy in matching the FDTD simulations and by extension physical devices. These results provide confidence that the modeling software can reliably reproduce the effects of optical extraction in a complex OLED structure.

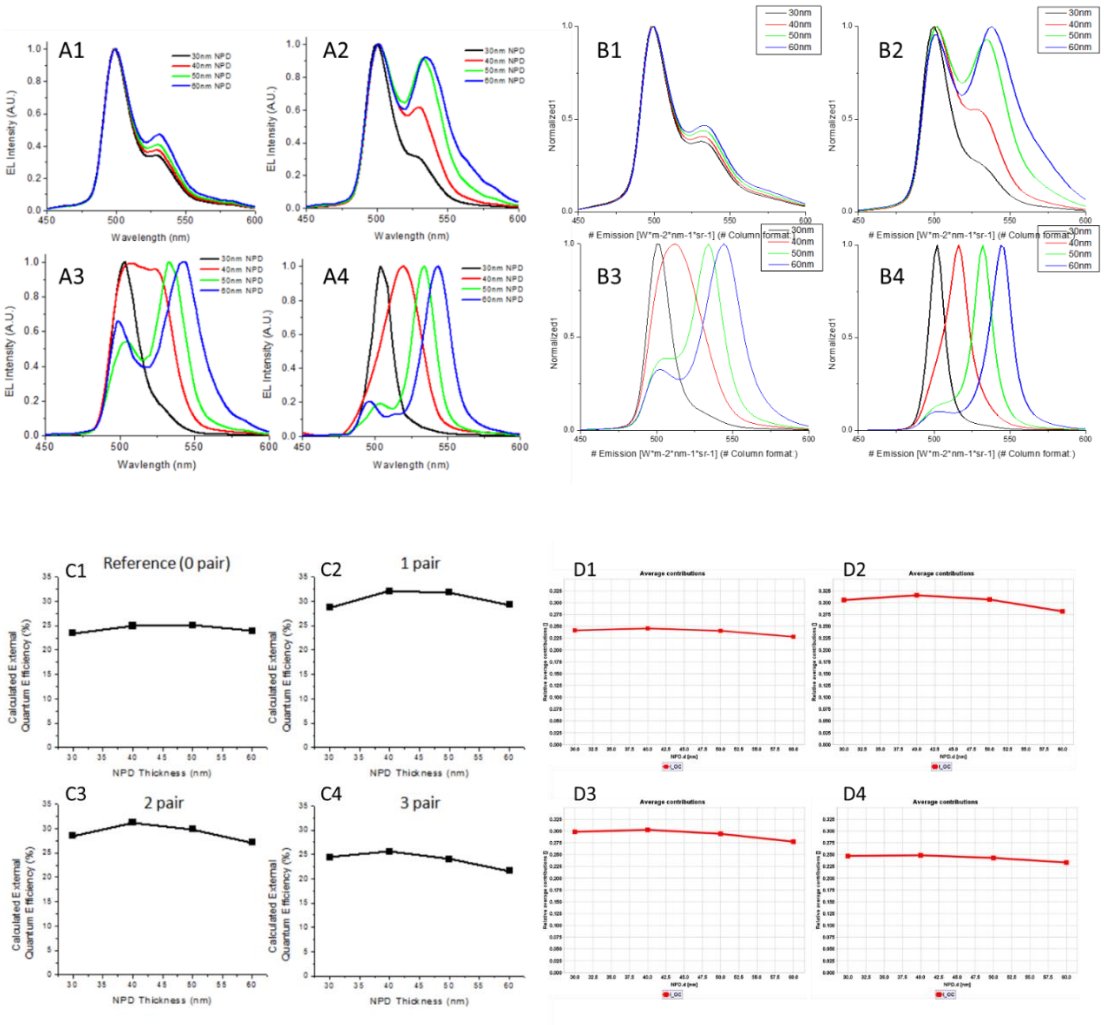

Figure 64: A1-A4 FDTD simulation of emission for 0 pair, 1 pair, 2 pair and 3 pair respectively at variable NPD thickness. B1-B4 Setfos simulation of emission for 0 pair, 1 pair, 2 pair and 3 pair respectively at variable NPD thickness. C1-C4 EQE Vs NPD thickness.

Building off a strong understanding of the modern OLED stack, it is widely acknowledged that there are 3 layers within the device whose thickness can be varied with minimal impact on the electrical properties of the device. These three layers are the transparent anode, the hole transporting layer and the electron transporting layer. These three layers will be the focus of the modeling to attempt to maximize light outcoupling of the device without incurring additional costs. In these simulations we will be evaluating the

potential enhancement to the air mode (light that escapes the substrate) and to the substrate mode (light that remains trapped in the substrate). It is important to note that the substrate mode is easily recovered by incorporating low cost microlens extractors. In the upcoming evaluation we will be examining the air and substrate modes to evaluate the potential of total extraction that can be achieved. These simulations were conducted at 580nm to match closely with the emitter that will be used in section 5.2.

Efficiency curves showing all the loss mechanisms of the device were constructed while each of the free parameters were varied. Figure 65a shows the optical structure that was modeled in the Setfos software.

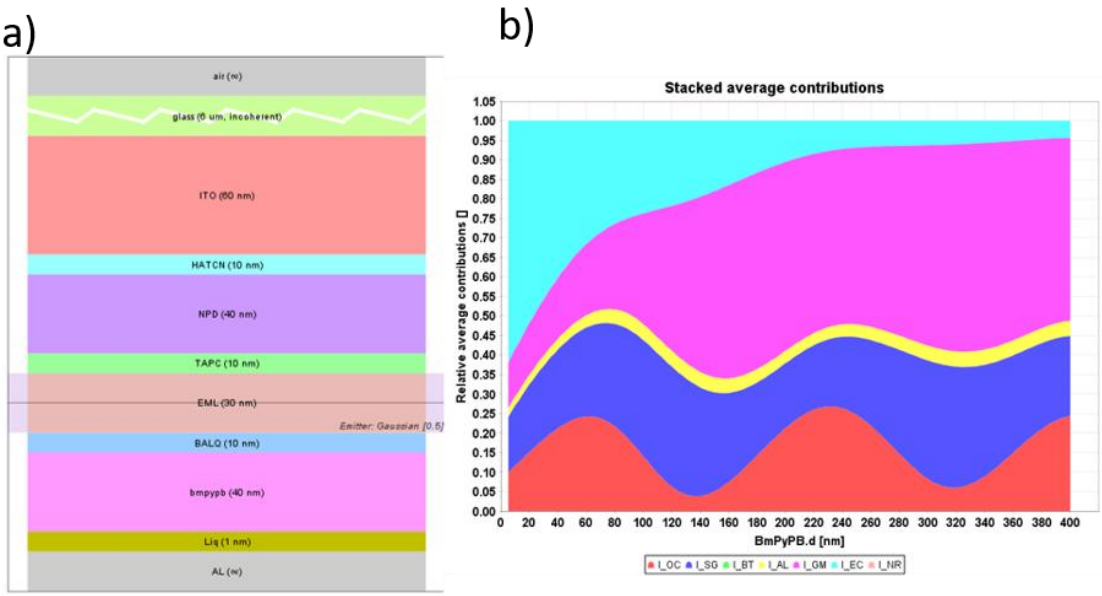

Figure 65: a) Schematic of the standard bottom emitting OLED structure that we employed, b) breakdown of probabilities of lighting in each of the different modes in a OLED structure as the ETL changes in thickness, (red-air mode, Dark blue-substrate mode, Yellow-Absorption loss, Pink-Organic waveguide mode, Light blue: plasmon quenching.

The values for reactive index of the materials were determined on a J. A. Woolam spectroscopic ellipsometer by measuring films on silicon wafers and fitting the data with a

generic oscillator model using the WVASE software. Efficiency fields where constructed while varying 1 of 3 parameters to attempt to identify local and global maximums. Figure 65b shows the optical losses vs ETL thickness. It is well studied that thickening the ETL will reduce plasmon losses within the device by helping to decouple the emissive zone and the metal cathode. Even though there is a very large portion of light lost to plasmon quenching when the ETL is below 200nm it is necessary to keep this layer thin. This helps to maintain proper electrical properties within the device. As a result of limitation in our ETL material the thickness was fixed to a value of 60nm, a local maximum for the air mode extraction. However, the model suggests that a thickness of 70-90nm would be better suited for this work. Future work might focus on development of a ETL that has high enough electron mobility to allow for a thicker layer while maintaining low driving voltage.

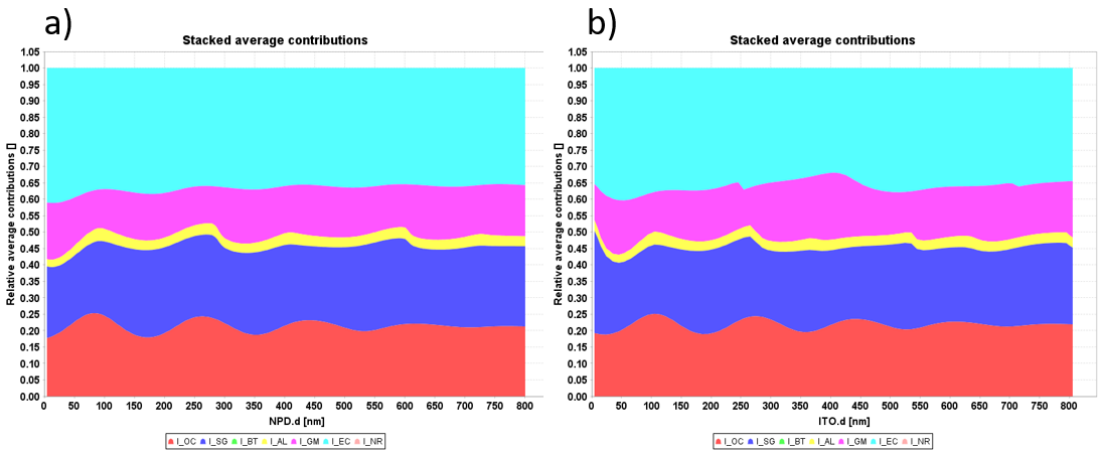

Figure 66: a) loss modes vs HTL thickness, b) loss modes vs transparent anode thickness.

The next step was to identify the local and global maximum extraction values for variable thickness HTL(Figure 66a). While the air mode is maximized at a thin HTL of 60nm (25% air mode) the sum of the air and substrate modes reach a global maximum at 270nm

for the HTL thickness. This has an air mode extraction of 24.7% and a substrate mode of 25%. However, 270nm is far thicker that most standard OLED devices. In order keep material consumption low we identify the local maximum at 90nm as a better option. At this thickness the air mode extraction is 25% and the substrate mode is 22.1%. We follow the same procedure to identify the best potential thickness for ITO. We identified the global maximum for ITO to be at 265nm. Unlike the HTL, thick ITO isn't a concern for the electrical properties of the device. Enhancement in the outcoupling of the device in both cases arises from weak cavity effects of the tuned layer. The small refractive index offset of Δn=.1-.3 is enough to cause these effects. Because of this we cannot simply combine these two independent results and expect to still achieve optimal results.

To determine the true potential for our devices maximum outcoupling, while varying only two parameters a series of simulations were run that couple the ITO thickness and the HTL thickness together to determine the maximum air mode, substrate mode and their combined totals.

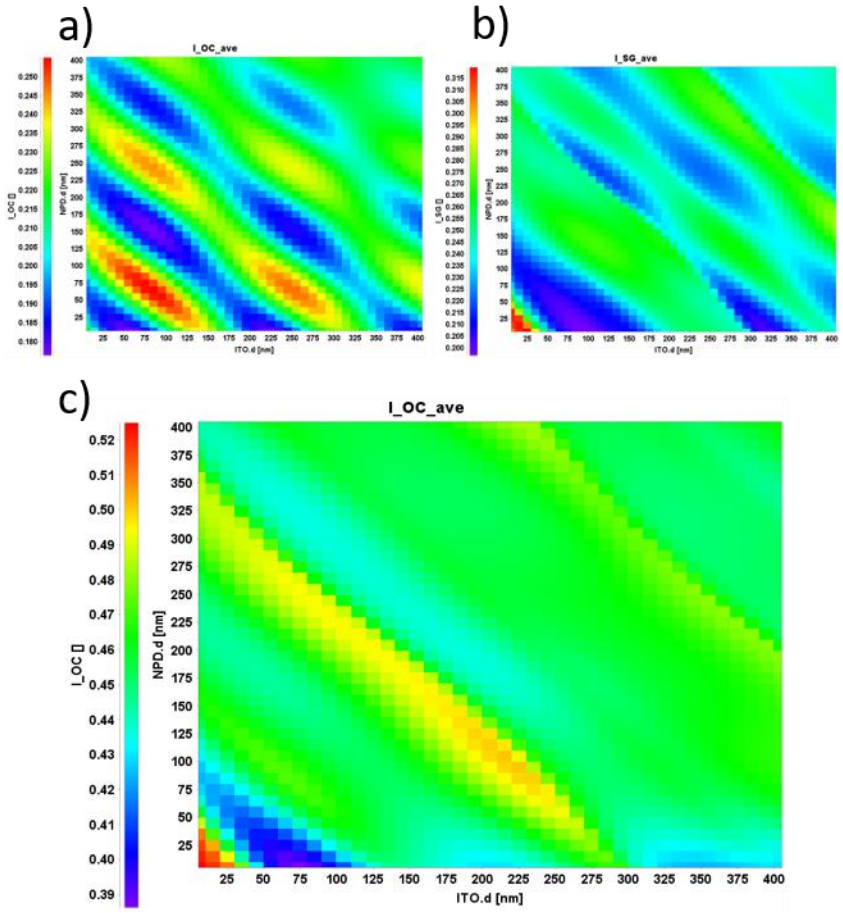

Figure 67: variable ITO and HTL thickness a) Air mode extraction, b) substrate mode and c) combined air and substrate mode.

The maximum attainable air mode is 25.4% at 75nm ITO and 60nm NPD. The maximum attainable substrate mode is 32% however this occurs at values that are too thin to be practically implemented. The local maximum substrate mode with suitable thickness occurs at 125nm ITO and 135nm NPD and is 28.5%. The maximum air and substrate mode extraction possible is 50% when ITO is 210nm and NPD is 100nm. This is the optimum structure that we identified assuming isotropic dipole orientation, 60nm ETL, and a glass substrate material. This shows that by only maximizing the air mode of an OLED device,

you are reducing the potential for total light extraction when using external extraction layers. The air mode optimized device is only capable of total extraction of 46% vs 50%.

5.2: PtN8PPy Device Study

With an optimized OLED structure identified, devices using PtN8PPy a red/amber emitter were tested. In a charge confined structure this emitter is capable of achieving 16% EQE (resulting from low PLQY) in air mode with a narrow emission profile less that 20nm full with half max and a peak emission at 580nm (Figure 68b). When testing devices, we used the technique drawn out in Figure 68c to measure the light trapped in the substrate mode. By filling the air gap between the surface of the glass and the detector with index matched gel the light travels out of the substrate without experiencing total internal reflection or any other optical phenomenon at the glass surface. By using this technique, we are able accurately quantify the amount of light in the substrate mode in a device setting and compare it directly to what was calculated in the model. The devices in this study are being specifically developed for potential applications in the automotive industry. The Economic Commission for Europe (ECE) has a stringent set of definitions for what CIE coordinates are required for automotive applications. These requirements can be found in Addendum 47: Regulation No. 48, revision 9 of the "Uniform provisions concerning the approval of vehicles with regard to the installation of lighting and light-signaling devices".

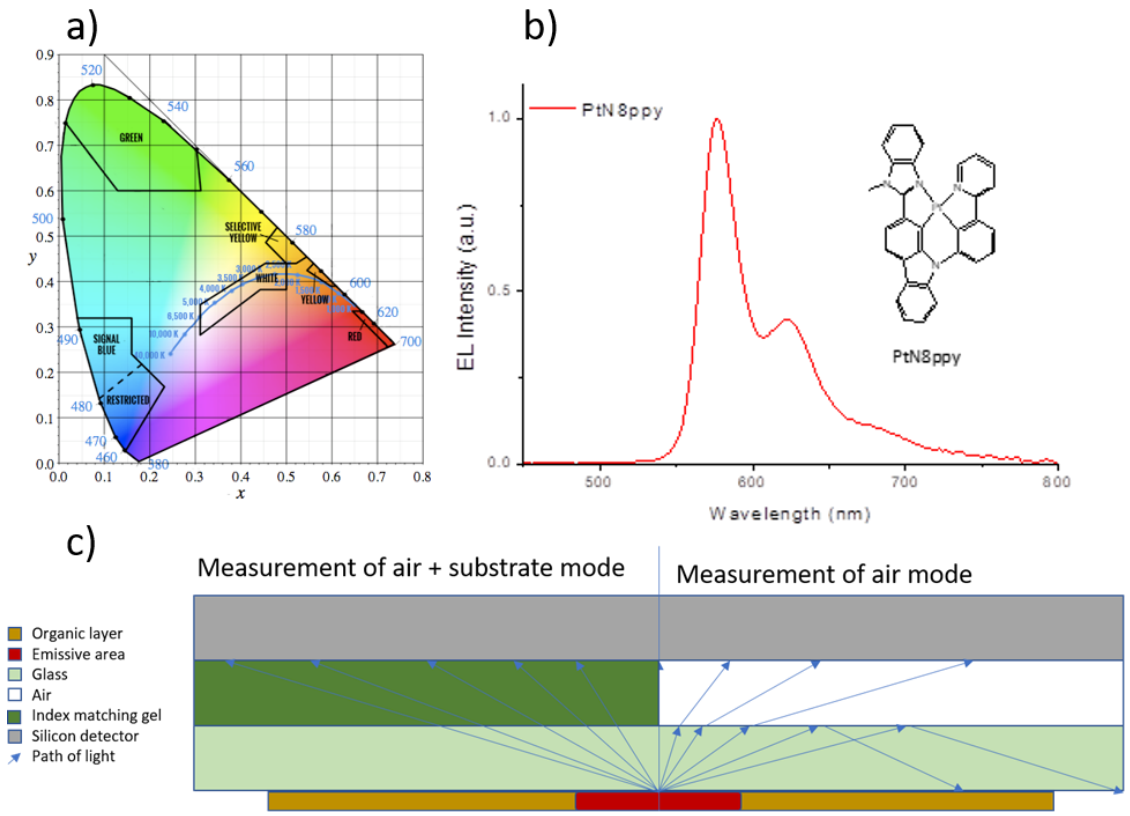

Figure 68: a) CIE plot showing the ECE defined red and yellow (amber) regions, b) narrow band emitter electroluminescent emission with chemical structure, and c) schematic showing how air mode and substrate mode are measured.

Fabricating a stable OLED device with this optimized structure yields promising results. The CIE coordinates are shifted closer to the ECE defined red region, however, this leads to more emission beyond the visible range resulting in a reduction of device brightness from 2,800 cd/m^2 to 1,700 cd/m^2. In addition to the color shift we see validation of our technique to maximize light extraction. Comparing the standard structure (device 1) to the optimized structure (device 2) demonstrates the positive effect our structure has on the ratio of substrate to air mode (Figure 69). Device 1 has a peak EQE of 16% in air mode and has another 14.5% trapped in the substrate. Device 2 has a peak air mode contribution of 12.8%

with a substrate mode contribution of 22.2%. Despite device 2 having a lower air mode value it has much higher potential for light extraction.

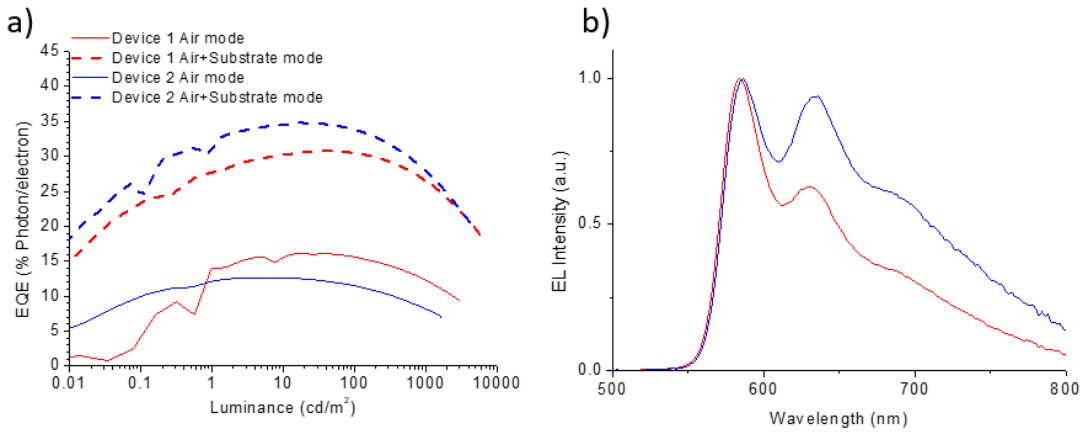

Figure 69: a) EQE vs luminance of standard and optimized OLED, measuring air mode and airmode + substrate mode, b) EL spectra of standard and optimized device.

As the efficiency of the surface extractors increases this technique will yield better results. The graph in Figure 69a shows the results if the surface extractors are assumed to be 100% efficient.

Table 1 shows how the overall device efficiency changes with the quality of the surface extractors. If the microlense has a 50% extraction efficiency, the new optimized structure will yield higher total device EQE.

Table 6: Summary of device performance of PtN8ppy EQE with various theoretical extractor efficiency.

Peak EQE	Air mode	Substrate mode	50% surface extractor	75% surface extractor	100% surface extractor
Device 1	16.0%	14.5%	23.25%	26.9%	30.5%
Device 2	12.8%	22.2%	23.9%	29.5%	35.0%

With an assumed microlense efficiency of 75% (a reasonable estimation based on industry available extractors) we see a notable improvement in the EQE from 26.9% up to 29.5%. This counterintuitive technique of optimizing the optical structure of a device for something other than maximum air mode extraction is shown to yield a modest improvement in EQE with minimal additional cost. Despite this positive progress, the lifetime and color of the PtN8ppy is lacking and needs further exploration to improve its commercial viability.

5.3: Pd3O3 Device Study

To further evaluate the performance of this optimized optical structure, additional analysis was conducted using a newly developed oriented emitter. Pd3O3 is an previously reported stable and efficient excimer emitter.[112] Excimer emitters have a high energy (blue/green) emission from the monomer state (one emissive complex isolated in the host) and a broad band lower energy (orange/red) emission in the excimer state (two or more complexes in close proximity in the host). In addition to Pd3O3's high efficiency and stability, it has also been shown to demonstrate TDV orientation in a thin film. This orientation can be quantified by conducting angular dependent PL spectroscopy measurements with a half-cylinder lens shown in Figure 70a.

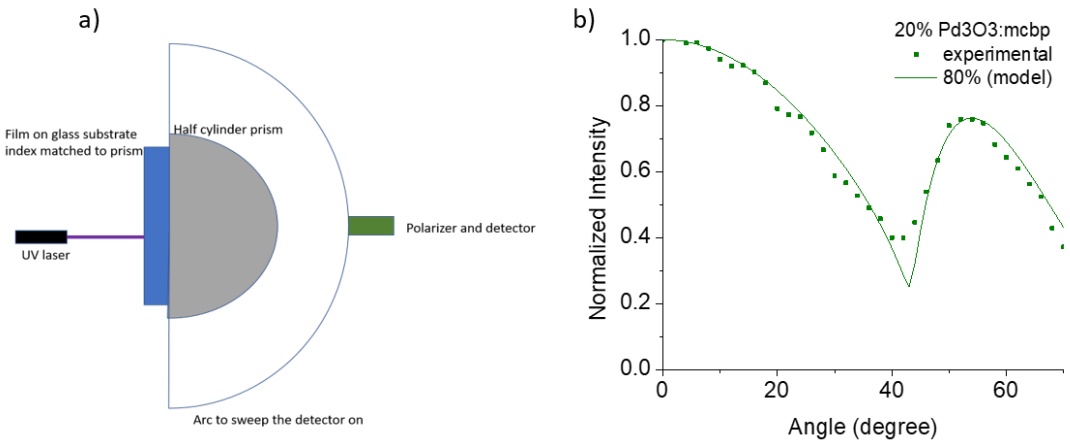

Figure 70: a) schematic of angular dependent PL spectroscopy measurement, b) experimental vs simulated intensity vs detection angle.

Pd3O3 demonstrated approximately 80% orientation (Figure 70b) where 66% is isotropic and 100% is the ideal condition. To evaluate the impact of emitter orientation on OLED extraction, the dipole orientation of the optimized OLED device was simulated.

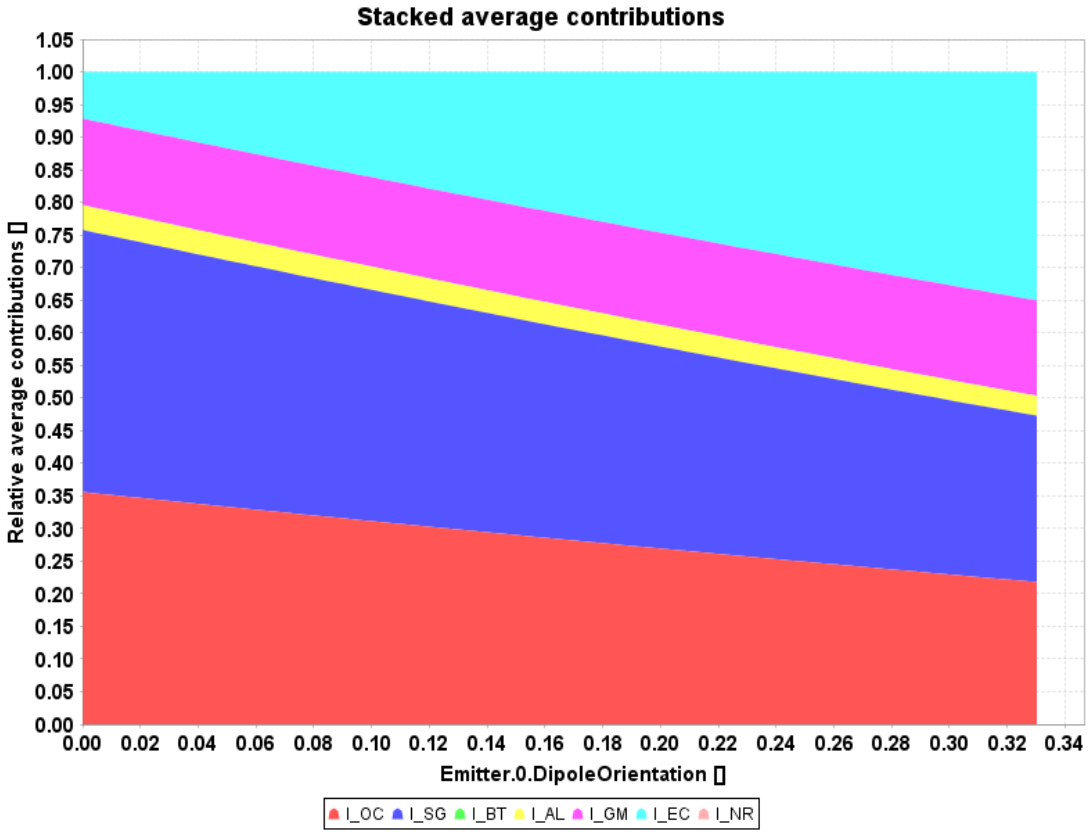

Figure 71: Setfos simulation of emitter dipole orientation and its impact on optical extraction.

The simulation shows a simple linear improvement to extraction as the dipole orientation approaches unity. With a dipole orientation of 80% the model suggests a peak EQE of 57% (air and substrate mode) is attainable with a maximum air mode of about 27.5%.

To evaluate the simulation, a Pd3O3 device was fabricated in a stable structure of ITO (210nm)/HATCN (10 nm) /NPD (100 nm)/Tris-PCZ (10 nm)/20% Pd3O3:mCBP (30 nm)/Balq (10 nm)/BPyTP (60 nm)/LiF (1 nm)/Al (100nm). The EQE vs luminance curve shows the performance of the planer air mode only device, a device with a low quality extraction layer, and a device with idealized substrate extraction. Pd3O3 demonstrates that a low-cost optical structure can reach a peak air mode EQE of 30% (Figure 72a). Under ideal

extraction conditions we can achieve over 58% peak EQE, with an EQE at 1,000 cd/m^2 of 50%. This is comparable to the performance of current OLED products on

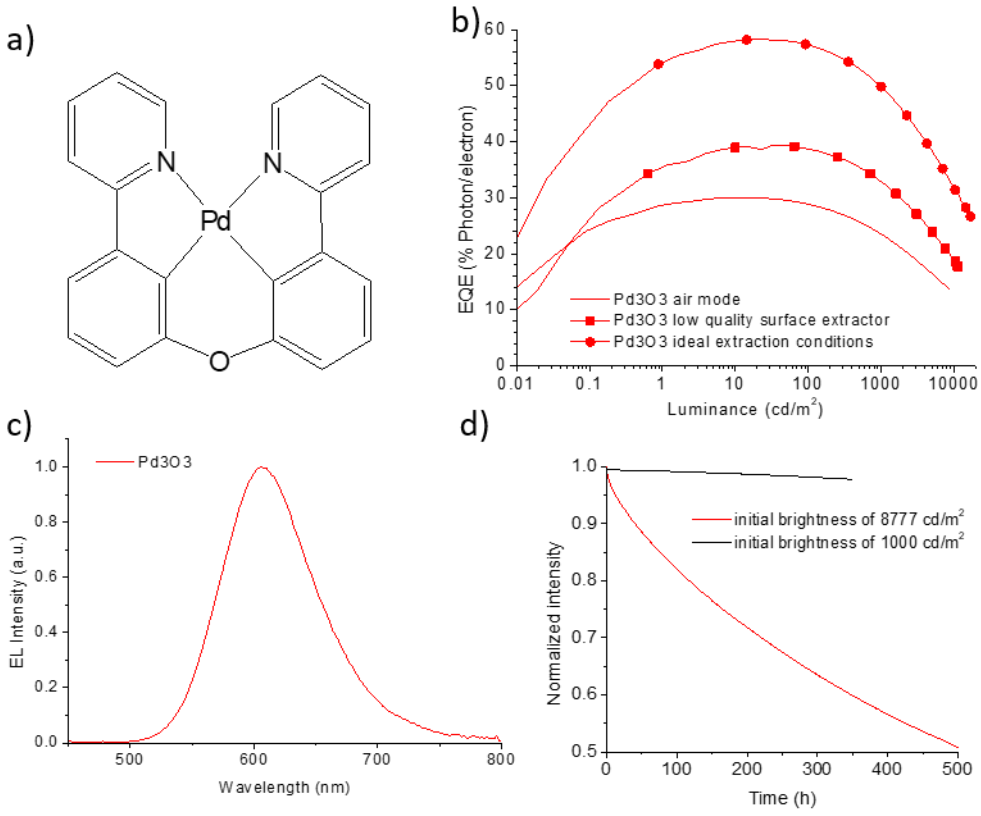

Figure 72: a) Pd3O3's chemical structure, b) EQE vs luminance, c) EL emission spectrum, and d) device operation time at variable brightness.

the market employing complex high-cost structures. In addition to high device efficiency we have tested the operational lifetime under accelerated conditions to 50% of its initial intensity. We have recorded a lifetime over 500 hours at an initial brightness of 8,777 cd/m^2 only measuring the air mode. Using the stretched exponential equation assuming an escalation factor of 1.8 we show the LT_{50} =24,000 hours. Examining the lifetime under the ideal extraction condition we have an initial brightness of 16,700 cd/m^2 using this value in the stretched exponential equation with the same escalation factor the lifetime increases to

LT_{50} =80,000 hours. The estimation for the escalation factor is a widely contested point in both industry and academic settings. Depending on the device structure as well and the degradation pathways of the emissive species, the escalation factor can vary widely. To estimate the escalation factor for our device we measured the lifetime under 2 driving conditions of 8,777 cd/m^2 and 1,000 cd/m^2. These two data points give us the ability to estimate the escalation factor. However, as a result of the high stability and our relatively short testing period (LT_{97}) we have a potential for a high degree of error. We calculated an escalation factor of 2.1±.2 however, more data points are required to improve the accuracy of these findings. In addition to being stable and efficient the CIE coordinates of Pd3O3 are X=.579 Y=.416. This falls within the ECE requirements for amber colored light.

5.4: Conclusion

In this chapter we have successfully demonstrated the optimization of a conventional OLEDs optical structures. Furthermore, we identified an alternative technique to achieving improved outcoupling when implementing microlenses ex situ to the device fabrication process. This has resulted in highly efficient and stable amber emitting OLED being developed that can compete with current OLED products without the need for high-cost techniques.

6: Conclusions

In this dissertation, numerous techniques are outlined and demonstrated for bringing OLED technology closer to commercial implementation. Among the major hurdles to widespread adoption of this technology are the development of stable and efficiency blue OLEDs, the development of high energy host materials for use in efficient phosphorescent deep blue devices, and optimization of cost-effective light extraction techniques. Examples of each of the following techniques have been demonstrated in this work.

6.1: Blue OLEDs

Two techniques for achieving efficient and stable blue emission have been demonstrated. In chapter 2, a novel and practical technique for improving charge balance and the exciton formation dynamics in a sky-blue OLED was demonstrated. Implementing a rationally designed layered EML structure is shown to alter the charge injection barriers and charge transport characteristics of a stable OLED device. In a stable structure, a PtNON device demonstrated an EQE at 1,000 cd/m^2 of 17.4% with an estimated LT_{70} of over 1,300 hours from a starting brightness of 1,000 cd/m^2. This stable PtNON device was further improved through the design of a fluorescent sensitized device that achieved an EQE at 1,000 cd/m^2 of 15.2% with an LT_{70} of 46 hours at a constant current density of 20 mA/cm^2. This device demonstrated a significant blue shift in EL emission with CIE coordinated improving from (0.17, 0.38) to (0.15, 0.25). These devices demonstrate current literature records for highly stable blue OLED devices operating at high efficiency and similar CIE coordinates.[63,165,166] In addition to improved device performance a new class of highly efficient OLED emitters were presented in chapter 3. MADF emitters allows for delayed fluorescent materials with a large ΔE_{ST} to maintain 100% IQE. This was demonstrated with three key emitters. PdN3N in a stable structure demonstrated a green OLED device with a

peak EQE of 22% with an EQE at 1,000 cd/m^2 of 13.7% with an LT_{95} of 32 hours from a starting brightness of 4,100 cd/m^2. This demonstrates that the MADF system process has the potential to be a stable and efficient OLED emitter. PdN1N-DM demonstrated a peak EL emission of 466 nm with CIE coordination of (0.14, 0.25), and the maximum EQE of 25.1 % in a charge confined structure. Additionally, in a stable structure PdN1N-dm demonstrating a maximum EQE of 9.8 %, CIE coordinates of (0.14, 0.32) and an estimated operational lifetime LT_{70} of 354 h at a brightness of 100 cd/m^2. This shows proof of concept for developing higher energy MADF emitters that have the potential for stable and efficient blue emission.

6.2: High Energy Host Materials

The development of high energy host materials for use in stable and efficient deep blue devices remains a major roadblock in research and industry. Chapter 4 outlines the development of two novel "M"-type hosts. A carbazole/fluorene hybrid called mDCzPF and a carbazole/9-silafluorene hybrid called mDCzPSiF, both with high E_T utilizing the meta-substituted phenyl groups as linkers. Red phosphorescent OLEDs using these "M"-type mDCzPSiF and mDCzPF as hosts represented a 7 to 10-fold operational lifetime improvement over previously reported "V"-type pDCzPF based OLEDs. Additionally, the "M"-type mDCzPF was implemented as a host for a high E_T emitter PtNON (2.83 eV). PtNON doped OLED using mDCzPF as host exhibited a peak EQE of 18.3% with a low roll-off demonstrating its compatibility with higher energy systems. This provides a new viable design scheme for host materials targeted at stable and efficient high energy phosphorescent OLEDs.

6.3: Enhanced Low-Cost Optical Extraction

A common hurdle to the wide spread adoption of any new technology is the cost. As cost is brought down, risk to adopters is reduced, and the adoption rate of the new technology grows. In chapter 5 a new technique to improve light extraction with minimal impact on cost was presented. By optimizing an OLEDs outcoupling to maximize the light channeled into the substrate mode of the device, the total light extraction can be improved after implementing a microlens array. By following this technique and assuming a microlens extraction efficiency of 75%, the EQE of PtN8ppy devices can be improved from 26.9% to 29.5%. By employing an amber emitter that demonstrates 80% horizontal orientation, a final device was able to achieve a peak EQE of 51% (assuming 75% efficient microlens films) with a long LT_{50} over 500 hours. This modest improvement in the optical outcoupling is achieved solely by thoughtful optimization of the optical structure of the OLED. Altering the thickness of the transparent anode layer would incur nearly no additional cost in a production setting making this a practical improvement to OLED device design.

6.4: Commercial Impacts of Research

Much of the research enclosed in this dissertation is targeted directly towards commercial applications. There are three primary innovations in this work that support this, 1) Layered EML structures for exciton management, 2) Low cost optical extraction techniques, 3) Phosphorescent excimer emitters for blue-free lighting.

Many tailored EML structures exist that are designed to improve the exciton management of an OLED. Unfortunately, many of these structures are complicated and require depositions techniques and levels of control that cannot be reproduced in a scaled environment, for example, linearly graded doped EMLs. This was among the primary drivers

for the design and optimization of the layered EML project. The layered EML has demonstrated significant performance enhancements while maintaining a simplified deposition technique. Conventional OLED manufacturing uses linear deposition tools with isolated chambers for each layer deposition. A complicated technique such as graded doped EML's would not be able to be adopted in this system. However, a layered EML could be fabricated with the addition of deposition chambers. While this would incur extra startup cost, it could yield improved OLED performance with minimal impact on production time or yield.

The need for improved optical extraction in OLED lighting applications is well reported and documented. Developing low cost techniques that can achieve this will continue to reduce the cost per lumen of OLED lighting. The tuning of optical cavity of an OLED discussed in Chapter 5 can allow for the maximization of light extraction from a given microlense array to be achieved. This technique does not change any crucial portion of the OLED fabrication process and would incur little to no additional cost on the manufacturing of an OLED. This improved extraction and cost saving measure will further help to bring down the cost per lumen of OLED lighting bringing it closer to widespread adoption.

Finally, the development of a highly efficient and stable excimer emitter Pd3O3 is briefly discussed in Chapter 5.3. Pd3O3 and its analogs have demonstrated an impressive amber emission that satisfies the requirements for blue-less lighting. The performance of this emitter in a simple planer OLED structure, using non-proprietary materials has matched or exceeded the performance of current commercial OLEDs using more complex structures and state-of-the-art materials. This high-performance emitter can be easily implemented into

a manufacturing setting with minimal work required to re-optimize its performance with state-of-the-art materials. With partnership from a commercial OLED vendor, Pd3O3 or its analog could dramatically improve the performance of blue-less OLED lighting products.

While all the research present here will have an impact on the OLED research field, the three sections mentioned can have a direct impact on the OLED industry and help bring this technology closer to widespread adoption.

REFERENCES

[1] H. Inokuchi, H. Akamatu, *Solid State Physics*, **1961**, 12, 93.

[2] J. Hwai, -Yuan Hsu, *Energy Policy*, **2018**, 117, 463.

[3] E. Mckenna, J. Pless, S.J. Darby, *Energy Policy*, **2018**, 118, 482.

[4] P. Shen, G. Wang, B. Kang, W. Guo, L. Shen, *ACS Applied Materials and Interfaces*, **2018**, 10, 6513.

[5] C.-C. Chen, L. Dou, J. Gao, W.-H. Chang, G. Li, Y. Yang, *Energy & Environmental Science*, **2013**, 6, 2714.

[6] R.R. Lunt, V. Bulovic, *Applied Physics Letters*, **2011**, 98, 113305.

[7] C. Reese, M. Roberts, M. Ling, Z. Bao, *Materials Today*, **2004**, 7, 20.

[8] S.J. Kim, S. Yoon, H.J. Kim, *Japanese Journal of Applied Physics*, **2014**, 53, 02BA02.

[9] J. Bornholt, R. Lopez, D.M. Carmean, L. Ceze, G. Seelig, K. Strauss,

[10] S.M.H. Tabatabaei Yazdi, Y. Yuan, J. Ma, H. Zhao, O. Milenkovic, *Scientific Reports*, **2015**, 5, 14138.

[11] S. Chand, J. Kumar, *Journal of Applied Physics* , **1997**, 82, 5005.

[12] C.R. Wronski, D.E. Carlson, R.E. Daniel, *Appl. Phys. Lett.*, **1976**, 29, 602.

[13] C.W. Tang, S.A. Vanslyke, *Appl. Phys. Lett*, **1987**, 51.

[14] V. Coropceanu, J. Cornil, D.A. Da, S. Filho, Y. Olivier, R. Silbey, J.-L. Brédas,

[15] I.G. Hill, A. Kahn, Z.G. Soos, R.A. Pascal, *Chemical Physics Letters*, **2000**, 327, 181.

[16] C. Groves, *Rep. Prog. Phys.*, **2017**, 80.

[17] N. Tessler, Y. Preezant, N. Rappaport, Y. Roichman, *Advanced Materials*, **2009**, 21, 2741.

[18] Z. Deng, S.T. Lee, D.P. Webb, Y.C. Chan, W.A. Gambling, *Synthetic Metals*, **1999**, 107, 107.

[19] O. Rubel, S.D. Baranovskii, P. Thomas, S. Yamasaki, *Physical Review B*, **2004**, 69.

[20] Abhishek P. Kulkarni, Christopher J. Tonzola, and Amit Babel, S.A. Jenekhe*, **2004**.

[21] R.R. Lunt, J.B. Benziger, S.R. Forrest, *Advanced Materials*, **2010**, 22, 1233.

[22] Y. Malozovsky, J.D. Fan, Y.M. Malozovsky, *International Journal of Modern Physics B* , **2013**, 27.

[23] R.R. Lunt, N.C. Giebink, A.A. Belak, J.B. Benziger, S.R. Forrest, *Journal of Applied Physics*, **2009**, 105, 53711.

[24] M. Pope, H.P. Kallmann, P. Magnante, *The Journal of Chemical Physics*, **1963**, 38.

[25] C.W. Tang, S.A. Vanslyke, C.H. Chen, *Journal of Applied Physics*, **1989**, 65, 3610.

[26] J. WEISS, *Nature*, **1943**, 152, 176.

[27] C. Adachi, M.A. Baldo, M.E. Thompson, S.R. Forrest, *Journal of Applied Physics*, **2001**, 90.

[28] M. Baldo, D. O'Brien, Y. You, A. Shoustikov, S. Sibley, M. Thompson, S. Forrest, *Letters to Nature*, **1998**, 395, 151.

[29] S. Hirata, Y. Sakai, K. Masui, H. Tanaka, S.Y. Lee, H. Nomura, N. Nakamura, M. Yasumatsu, H. Nakanotani, Q. Zhang, K. Shizu, H. Miyazaki, C. Adachi, *Nature Materials*, **2015**, 14, 330.

[30] T. Nakagawa, S.-Y. Ku, K.-T. Wong, C. Adachi, *Chem.*, **2012**, 48, 9580.

[31] T.-A. Lin, T. Chatterjee, W.-L. Tsai, W.-K. Lee, M.-J. Wu, M. Jiao, K.-C. Pan, C.-L. Yi, C.-L. Chung, K.-T. Wong, C.-C. Wu, *Advanced Materials*, **2016**, 28, 6976.

[32] Z.-Q. Zhu, T. Fleetham, E. Turner, J. Li, *Advanced Materials*, **2015**, 27, 2533.

[33] P. Atkins, J. De Paula, Physical Chemistry. 2010.

[34] W. Helfricht, W.G. Schnelder, *Phys. Rev. Letters* , **1965**, 14, 229.

[35] J. Dresner, *RCA Review*, **1969**, 30, 322.

[36] D.F. Williams, M. Schadt, *Proceedings of the IEEE*, **1970**, 58, 476.

[37] S.-J. Su, H. Sasabe, T. Takeda, J. Kido, *Chem. Mater.*, **2008**, 20, 1691.

[38] Y. Park, B. Kim, C. Lee, A. Hyun, S. Jang, J.-H. Lee, Y.-S. Gal, T.H. Kim, K.-S. Kim, J. Park, *The Journal of Physical Chemistry C*, **2011**, 115, 4843.

[39] S.-J. Su, Y. Takahashi, T. Chiba, T. Takeda, J. Kido, *Advanced Functional Materials*, **2009**, 19, 1260.

[40] M. Kimura, S. Kuwano, Y. Sawaki, H. Fujikawa, K. Noda, Y. Taga, K. Takagi, *Journal of Materials Chemistry*, **2005**, 15, 2393.

[41] M. Ben Khalifa, D. Vaufrey, J. Tardy, *Organic Electronics*, **2004**, 5, 187.

[42] V.I. Adamovich, S.R. Cordero, P.I. Djurovich, A. Tamayo, M.E. Thompson, B.W. Dõandrade, S.R. Forrest, *Organic Electronics*, **2003**, 4, 77.

[43] G.E. Jabbour, B. Kippelen, N.R. Armstrong, N. Peyghambarian,) B Kippelen, *Appl. Phys. Lett.*, **1998**, 731.

[44] S.-F. Chen, C.-W. Wang, *Appl. Phys. Lett*, **2004**, 85, 765.

[45] A.B. Chwang, R.C. Kwong, J.J. Brown, *Appl. Phys. Lett*, **2002**, 80, 725.

[46] R.J. Holmes, B.W. D'Andrade, S.R. Forrest, X. Ren, J. Li, M.E. Thompson, *Appl. Phys. Lett.* , **2003**, 83, 3818.

[47] H. Klauk, John Wiley & Sons., Organic electronics : materials, manufacturing and applications. Wiley-VCH, 2006.

[48] T.-W. Lee, T. Noh, H.-W. Shin, O. Kwon, J.-J. Park, B.-K. Choi, M.-S. Kim, D.W. Shin, Y.-R. Kim, *Advanced Functional Materials*, **2009**, 19, 1625.

[49] C. Féry, B. Racine, D. Vaufrey, H. Doyeux, S. Cinà, *Appl. Phys. Lett.*, **2005**, 87, 213502.

[50] Z.-Q. Zhu, K. Klimes, S. Holloway, J. Li, *Advanced Materials*, **2017**, 29.

[51] H. Aziz, Z.D. Popovic, **2004**, 4522.

[52] L.F. Cheng, L.S. Liao, S.T. Lee, **2000**, 418.

[53] L.-S. Liao, C.W. Tang, *Journal of Applied Physics*, **2008**, 044501.

[54] S.C. Xia, R.C. Kwong, V.I. Adamovich, M.S. Weaver, J.J. Brown, **2007**.

[55] T.P. Nguyen, J. Ip, P. Jolinat, P. Destruel, **2001**, 172, 75.

[56] M. Matsumura, A. Ito, Y. Miyamae, **2003**, 1042, 1.

[57] D. Zou, M. Yahiro, T. Tsutsui, **1997**, 91, 191.

[58] T. Fleetham, G. Li, J. Li, *ACS Applied Materials and Interfaces*, **2015**, 7, 16240.

[59] Q. Wang, H. Aziz, *ACS Appl. Mater. Interfaces*, **2013**, 5, 8733.

[60] N.C. Giebink, M.S. Weaver, J.J. Brown, S.R. Forrest, *Journal of Applied Physics*, **2009**, 105, 124514.

[61] N.C. Giebink, M.S. Weaver, P.B. Mackenzie, J.J. Brown, M.E. Thompson, S.R. Forrest, *Journal of Applied Physics*, **2008**, 103, 044509.

[62] K. Saxena, V.K. Jain, D.S. Mehta, *Optical Materials*, **2009**, 32, 221.

[63] Y. Zhang, J. Lee, S.R. Forrest, *Nature Communications*, **2014**, 5, 5008.

[64] Y. Sun, N.C. Giebink, H. Kanno, B. Ma, M.E. Thompson, S.R. Forrest, *Nature*, **2006**, 440, 908.

[65] J.-M. Kim, C.-H. Lee, J.-J. Kim, *Appl. Phys. Lett*, **2017**, 111, 203301.

[66] D. Ma, C.S. Lee, S.T. Lee, Hung. L. S., *Appl. Phys. Lett*, **2002**, 80, 3641.

[67] T.B. Fleetham, L. Huang, K. Klimes, J. Brooks, J. Li, *Chemistry of Materials*, **2016**, 28, 3276.

[68] K. Okumoto, H. Kanno, Y. Hamaa, H. Takahashi, K. Shibata, *Applied Physics Letters*, **2006**, 89, 169901.

[69] G. Li, T. Fleetham, E. Turner, X. Hang, J. Li, *Advanced Optical Materials*, **2015**, 3, 390.

[70] G. Li, J. Ecton, B.O. Brien, J. Li, *Organic Electronics*, **2014**, 15, 1862.

[71] H. Fukagawa, T. Shimizu, H. Hanashima, Y. Osada, M. Suzuki, H. Fujikake, *Advanced Materials*, **2012**, 24, 5099.

[72] L. Zhou, C.-L. Kwong, C.C. Kwok, G. Cheng, H. Zhang, C.-M. Che, *Chem. Asian J.*, **2014**, 9, 2984.

[73] E. Turner, N. Bakken, J. Li, *Inorganic Chemistry*, **2013**, 52, 7344.

[74] G. Li, T. Fleetham, J. Li, *Advanced Materials*, **2014**, 26, 2931.

[75] T. Fleetham, J. Ecton, Z. Wang, N. Bakken, J. Li, *Advanced Materials*, **2013**, 25, 2573.

[76] J. Kalinowski, V. Fattori, M. Cocchi, J.A.G. Williams, *Coordination Chemistry Reviews*, **2011**, 255, 2401.

[77] J. Brooks, Y. Babayan, S. Lamansky, P.I. Djurovich, I. Tsyba, R. Bau, M.E. Thompson, *Inorganic Chemistry*, **2002**, 41, 3055.

[78] D. a K. Vezzu, J.C. Deaton, J.S. Jones, L. Bartolotti, C.F. Harris, A.P. Marchetti, M. Kondakova, R.D. Pike, S. Huo, *Inorganic Chemistry*, **2010**, 49, 5107.

[79] Z. Wang, E. Turner, V. Mahoney, S. Madakuni, T. Groy, J. Li, *Inorganic Chemistry*, **2010**, 49, 11276.

[80] R.C. Kwong, M.R. Nugent, L. Michalski, T. Ngo, K. Rajan, Y. Tung, M.S. Weaver, T.X. Zhou, M. Hack, M.E. Thompson, S.R. Forrest, J.J. Brown, *Appl. Phys. Lett*, **2002**, 81, 162.

[81] Y.J. Cho, K.S. Yook, J.Y. Lee, *Advanced Materials*, **2014**, 26, 4050.

[82] M. Kim, S.K. Jeon, S. Hwang, J.Y. Lee, *Advanced Materials*, **2015**, 27, 2515.

[83] T. Fleetham, G. Li, L. Wen, J. Li, *Advanced Materials*, **2014**, 26, 7116.

[84] Y. Tao, C. Yang, J. Qin, *Chem. Soc. Rev.*, **2011**, 40, 2943.

[85] J. Li, P.I. Djurovich, B.D. Alleyne, M. Yousufuddin, N.N. Ho, J.C. Thomas, J.C. Peters, R. Bau, M.E. Thompson, *Inorganic Chemistry*, **2005**, 44, 1713.

[86] E. Turner, N. Bakken, J. Li, *Inorganic Chemistry*, **2013**, 52, 7344.

[87] H. Nakanotani, K. Masui, J. Nishide, T. Shibata, C. Adachi, *Scientific Reports*, **2013**, 3, 1.

[88] J. Michl, *Acc. Chem. Res.*, **1990**, 23, 127.

[89] N.J. Turo, Modern Molecular Photochemistry. University Science Books, 1991.

[90] M.A. Baldo, S. Lamansky, P.E. Burrows, M.E. Thompson, S.R. Forrest, *Appl. Phys. Lett*, **1999**, 75, 4.

[91] M.A. Baldo, M.E. Thompson, S.R. Forrest, *Letters to Nature*, **2000**, 403, 750.

[92] C. Adachi, M.A. Baldo, S.R. Forrest, M.E. Thompson, *Appl. Phys. Lett*, **2000**, 77, 904.

[93] S. Kim, W. Jeong, C. Mayr, Y. Park, K. Kim, J. Lee, C. Moon, W. Brütting, J. Kim, *Advanced Functional Materials*, **2013**, 23, 3896.

[94] H. Uoyama, K. Goushi, K. Shizu, H. Nomura, C. Adachi, *Nature*, **2012**, 492, 234.

[95] F.B. Dias, K.N. Bourdakos, V. Jankus, K.C. Moss, T. Kamtekar, V. Bhalla, J. Santos, M.R. Bryce, A.P. Monkman, *Advanced Materials*, **2013**, 25, 3707.

[96] Y. Im, J.Y. Lee, *Chem. Mater.*, **2014**, 26, 1413.

[97] X. Ren, J. Li, R.J. Holmes, P.I. Djurovich, S.R. Forrest, M.E. Thompson, *Chem. Mater.*, **2004**, 16, 4743.

[98] Q. Zhang, J. Li, K. Shizu, S. Huang, S. Hirata, H. Miyazaki, C. Adachi, *JACS*, **2012**, 134, 14706.

[99] Q. Zhang, B. Li, S. Huang, H. Nomura, H. Tanaka, C. Adachi, *Nature Photonics*, **2014**, 8, 326.

[100] J. Kalinowski, V. Fattori, M. Cocchi, J. a G. Williams, *Coordination Chemistry Reviews*, **2011**, 255, 2401.

[101] T. Hofbeck, U. Monkowius, H. Yersin, *JACS*, **2015**, 137, 399.

[102] W.C.H. Choy, W.K. Chan, Y. Yuan, *Advanced Materials*, **2014**, 26, 5368.

[103] H. Yersin, A.F. Rausch, R. Czerwieniec, T. Hofbeck, T. Fischer, *Coordination Chemistry Reviews*, **2011**, 255, 2622.

[104] S.J. Su, E. Gonmori, H. Sasabe, J. Kido, *Advanced Materials*, **2008**, 20, 4189.

[105] N. Chopra, J.S. Swensen, E. Polikarpov, L. Cosimbescu, F. So, A.B. Padmaperuma, *Applied Physics Letters*, **2010**, 97, 3.

[106] S. C. F. Kui, P.K. Chow, G.S.M. Tong, S.L. Lai, G. Cheng, C.C. Kwok, K.H. Low, M.Y. Ko, C.M. Che, *Chemistry - A European Journal*, **2013**, 19, 69.

[107] A.M.G. Helander, Z.B. Wang, J. Qiu, M.T. Greiner, D.P. Puzzo, Z.W. Liu, H. Lu, *Science*, **2011**, 332, 944.

[108] D. Tanaka, H. Sasabe, Y.-J. Li, S.-J. Su, T. Takeda, J. Kido, *Japanese Journal of Applied Physics Letter*, **2007**, 46, L10.

[109] T. Fleetham, Z. Wang, J. Li, *Organic Electronics*, **2012**, 13, 1430.

[110] K. Li, G. Cheng, C. Ma, X. Guan, W.M. Kwok, Y. Chen, W. Lu, C.M. Che, *Chemical Science*, **2013**, 4, 2630.

[111] R.J. Holmes, S.R. Forrest, T. Sajoto, A. Tamayo, P.I. Djurovich, M.E. Thompson, J. Brooks, Y. Tung, D. Andrade, M.S. Weaver, R.C. Kwong, J.J. Brown, *Appl. Phys. Lett*, **2005**, 87, 1.

[112] T. Fleetham, Y. Ji, L. Huang, T.S. Fleetham, J. Li, *Chemical Science*, **2017**, 8, 7983.

[113] L.J. Rothberg, A.J. Lovinger, *journal of materials research*, **1996**, 11, 3174.

[114] X.C. Hang, T. Fleetham, E. Turner, J. Brooks, J. Li, *Angewandte Chemie - International Edition*, **2013**, 52, 6753.

[115] K. Togashi, S. Nomura, N. Yokoyama, T. Yasuda, C. Adachi, *Journal of Materials Chemistry*, **2012**, 22, 20689.

[116] X. Wang, T. Peng, C. Nguyen, Z.H. Lu, N. Wang, W. Wu, Q. Li, S. Wang, *Advanced Functional Materials*, **2017**, 27.

[117] K. Klimes, Z.-Q. Zhu, S. Holloway, J. Li, in *Proceedings of SPIE - The International Society for Optical Engineering*, 2016, 9941.

[118] T.B. Fleetham, L. Huang, K. Klimes, J. Brooks, J. Li, *Chemistry of Materials*, **2016**, 28.

[119] C. Adachi, R.C. Kwong, P. Djurovich, V. Adamovich, M.A. Baldo, M.E. Thompson, S.R. Forrest, *Appl. Phys. Lett*, **2001**, 79, 2082.

[120] R.J. Holmes, S.R. Forrest, Y. Tung, R.C. Kwong, J.J. Brown, S. Garon, M.E. Thompson, *Appl. Phys. Lett*, **2003**, 82, 2422.

[121] L. Cui, J.U. Kim, H. Nomura, H. Nakanotani, C. Adachi, *Angewandte Chemie - International Edition*, **2016**, 55, 6864.

[122] K.S. Yook, J.Y. Lee, *Advanced materials*, **2012**, 24, 3169.

[123] L. Xiao, Z. Chen, B. Qu, J. Luo, S. Kong, Q. Gong, J. Kido, *Advanced Materials*, **2011**, 23, 926.

[124] X. Yang, G. Zhou, W. Wong, *Chem. Soc. Rev.*, **2015**, 44, 8484.

[125] G. Li, K. Klimes, T. Fleetham, Z.-Q. Zhu, J. Li, *Applied Physics Letters*, **2017**, 110.

[126] L. Cui, Y. Deng, D.P. Tsang, Z. Jiang, Q. Zhang, L.-S. Liao, C. Adachi, *Advanced Materials*, **2016**, 28, 7620.

[127] C. Chan, M. Tanaka, H. Nakanotani, C. Adachi, *Nature Communications*, **2018**, 9, 2.

[128] K. Brunner, A. Van Dijken, H. Bo, J.J.A.M. Bastiaansen, N.M.M. Kiggen, B.M.W. Langeveld, *JACS*, **2004**, 126, 6035.

[129] W. Li, J. Qiao, L. Duan, L. Wang, Y. Qiu, *Tetrahedron*, **2007**, 63, 10161.

[130] P. Shih, C. Chiang, A.K. Dixit, C. Chen, M. Yuan, R. Lee, C. Chen, E.W. Diau, C.-F. Shu, *organic letters*, **2006**, 8, 2799.

[131] M. Tsai, T. Ke, H. Lin, C. Wu, S. Chiu, F.-C. Fang, Y.-L. Liao, K.T. Wong, Y.-H. Chen, C.-I. Wu, *ACS Appl. Mater. Interfaces*, **2009**, 1, 567.

[132] T. Tsuboi, S. Liu, M. Wu, C. Chen, *Organic Electronics*, **2009**, 10, 1372.

[133] H. Fukagawa, K. Watanabe, S. Tokito, *Appl. Phys. Lett*, **2008**, 93, 1.

[134] T. Tsuboi, H. Murayama, S. Yeh, M. Wu, C. Chen, *Optical Materials*, **2008**, 31, 366.

[135] D. Tanaka, Y. Agata, T. Takeda, S. Watanabe, J. Kido, *Japanese Journal of Applied Physics*, **2007**, 46, 117.

[136] J. Lee, J. Lee, J.Y. Lee, H. yong Chu, *Synthetic Metals*, **2009**, 159, 1956.

[137] M. Leung, W. Yang, C. Chuang, J. Lee, C. Lin, M. Wei, Y. Liu, *organic letters*, **2012**, 14, 4986.

[138] Y.J. Cho, J. Yeob, *chem. Eur.*, **2011**, 17, 11415.

[139] Z. Jiang, Y. Chen, C. Fan, C. Yang, Q. Wang, Y. Tao, Z. Zhang, J. Qin, D. Ma, *the royal society of chemistry*, **2009**.

[140] H. Chen, Z. Jiang, C. Gao, M. Xu, S.-C. Dong, L.-S. Cui, S.-J. Ji, L.-S. Liao, *chem. Eur.*, **2013**, 19, 11791.

[141] G. Li, Z. Zhu, Q. Chen, J. Li, *Organic Electronics*, **2019**, 69, 135.

[142] C. Lee, J. Lee, K. Kim, J. Kim, *Advanced Functional Materials*, **2018**, 28, 1.

[143] T. Fleetham, J. Ecton, G. Li, J. Li, *Organic Electronics*, **2016**, 37, 141.

[144] B.E.L. Williams, K. Haavisto, J. Li, G.E. Jabbour, *Advanced Materials*, **2007**, 19, 197.

[145] B.X. Yang, Z. Wang, S. Madakuni, J. Li, G.E. Jabbour, **2008**, 2405.

[146] T. Fleetham, L. Huang, J. Li, *Advanced Functional Materials*, **2014**, 24, 6066.

[147] G.E. Norby, C. Park, B.O. Brien, G. Li, L. Huang, J. Li, *Organic Electronics*, **2016**, 37, 163.

[148] J. Song, K. Kim, E. Kim, C. Moon, Y. Kim, J. Kim, S. Yoo, *Nature Communications*, **2018**, 9, 1.

[149] N.K. Patel, S. Cinà, J.H. Burroughes, *IEEE on selectred topics in quantum electronics*, **2002**, 8, 346.

[150] G. Gu, D.Z. Garbuzov, P.E. Burrows, S. Venkatesh, S.R. Forrest, *optics letters*, **1997**, 22, 396.

[151] T. Shiga, H. Fujikawa, Y. Taga, *Journal of Applied Physics*, **2003**, 93, 19.

[152] X. Liu, D. Poitras, Y. Tao, C. Py, *J. Vac. Sci. Technol. A*, **2004**, 22, 764.

[153] C.-L. Lin, H.-W. Lin, C. Wu, *Appl. Phys. Lett.*, **2005**, 87, 1.

[154] S. Moller, S. Forrest, *Journal of Applied Physics*, **2002**, 91.

[155] A. Salehi, Y. Chen, X. Fu, C. Peng, F. So, *ACS Applied Materials & Interfaces*, **2018**, 10, 9595.

[156] M. Wei, *optical express*, **2004**, 12, 5777.

[157] H. Shin, J. Lee, C. Moon, J. Huh, B. Sim, J. Kim, *Advanced Materials*, **2016**, 28, 4920.

[158] soon M. Jeong, F. Araoka, Y. Machida, H. Takezoe, S. Nishimura, G. Suzaki, *Appl. Phys. Lett.*, **2008**, 92, 1.

[159] A. Kohnen, M.C. Gather, N. Riegel, P. Zacharias, K. Meerholz, *Appl. Phys. Lett*, **2007**, 91, 1.

[160] M.J. Jurow, C. Mayr, T.D. Schmidt, T. Lampe, P.I. Djurovich, W. Brutting, M.E. Thompson, *Nat Mater*, **2015**, advance on.

[161] D.H. Kim, K. Inada, L. Zhao, T. Komino, N. Matsumoto, J.C. Ribierre, C. Adachi, *J. Mater. Chem. C*, **2017**, 5, 1216.

[162] W. Lukosz, R.E. Kunz, *J. opt. soc. am*, **1978**, 67, 1607.

[163] K.A. Neyts, *J. opt. soc. am*, **1998**, 15, 962.

[164] J.D. Ecton, *dissertation*, **2014**.

[165] J. Lee, C. Jeong, T. Batagoda, C. Coburn, M.E. Thompson, S.R. Forrest, *Nature Communications*, **2017**, 8, 1.

[166] W. Song, J.Y. Lee, *Advanced Optical Materials*, **2017**, 5.

APPENDIX A
CUSTOM BUILT OLED EQUIPMENT FOR AAML LAB

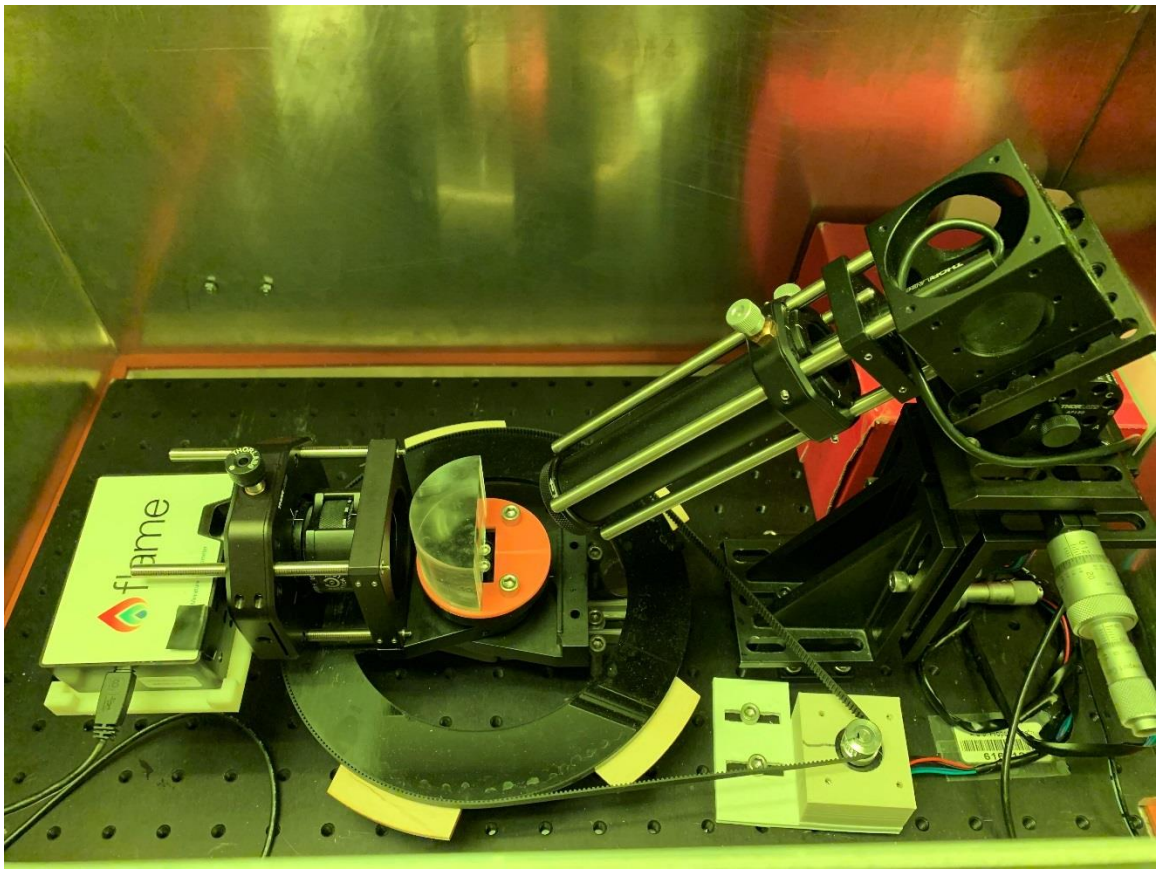

Angular Dependent PL Spectroscopy

This tool was built to measure of the emitting molecules orientation in a thin film. A UV laser excites a thin film on quartz that is index matched to a half cylinder lens. A spectrometer is aligned with the excitation point and the polarized emission from the film is measured as it sweeps from 0-90 degrees. This data is then fit to a library of simulations obtained from optical modeling using Setfos. This enable an estimation of the anisotropic properties of the emissive molecule in a thin film. The tool was designed to be fully automated to allow its class 3b laser to be contained in a light sealed box. This provides both protection for the user and reduced ambient noise.

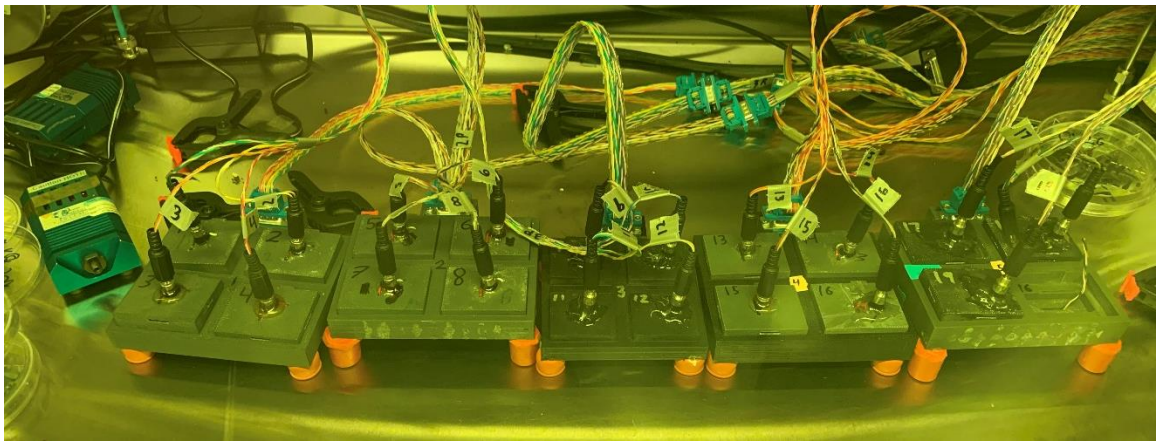

Multi-channel OLED lifetime testing system

To enable a faster research throughput, a low-cost multichannel testing system was developed. This system using a switch matrix and a single high-accuracy ammeter to read the and log the brightness decay of 20 OLEDs simultaneously. This system also has the capacity to be scaled up to 60 channels and beyond with minimal alterations.